Balanced Initialisation Techniques for Coupled Ocean-Atmosphere Models

James G. Jackson

University College London

A thesis submitted for the degree of Doctor of Philosophy

September 5, 2011

I, James George Jackson, confirm that the work presented in this thesis is my own. Where information has been derived from other sources, I confirm that this has been indicated in the thesis.

Abstract

Interactive dynamical ocean and atmosphere models are commonly used for predictions on seasonal timescales, but initialisation of such systems is problematic. In this thesis, idealised coupled models of the El Niño Southern Oscillation phenomenon are used to explore potential new initialisation methods. The basic ENSO model is derived using the two-strip concept for tropical ocean dynamics, together with a simple empirical atmosphere. A hierarchy of models is built, beginning with a basic recharge oscillator type model and culminating in a general n-box model. Each model is treated as a dynamical system. An important step is the 10-box model, in which the seasonal cycle is introduced as an extension of the phase space by two dimensions, which paves the way for more complex and occasionally chaotic behaviour.

For the simplest 2-box model, analytic approximate solutions are described and used to investigate the parameter dependence of regimes of behaviour. Model space is explored statistically and parametric instability is found for the 10-box and upward versions: while it is by no means a perfect simulation of the real world phenomena, some regimes are found which have features similar to those observed.

Initialisation is performed on a system from the n-box model (with $n = 94$), using dimensional reduction via two separate methods: a linear singular value decomposition approach and a nonlinear slow manifold (approximate inertial manifold) type reduction. The influence of the initialisation methods on predictive skill is tested using a perfect model approach. Data from a model integration are treated as observation, which are perturbed randomly on large and small spatial scales, and used as initial states for both reduced and full model forecasts. Integration of the reduced models provides a continuous initialisation process, ensuring orbits remain close to the attractor for the duration of the forecasts. From sets of ensemble forecasts, statistical measures of skill are calculated. Results are found to depend on the dimensionality of the reduced models and the type of initial perturbations used, and model reduction is found to result in a slight improvement in skill from the full model in each case, as well as a significant increase in the maximum timestep.

Contents

List of Figures

Chapter 1

Introduction

1.1 Outline

The sensitive nature of the Earth's climate system acts to shroud the details of its future state in uncertainty. With growing concerns for the stability of the current state comes the need for accurate predictions. Climate predictions can come in many forms, from scales of months to years, or years to decades. The focus here is on the former, seasonal variety of predictions. Unlike decadal prediction, this places a high emphasis on how the current state influences the final state at a time of interest. Sensitivity of the initial state hearkens back to numerical weather prediction, and before discussing climate dynamics it is worth discussing its predecessor in order to clarify the title of this work.

Seasonal climate prediction is analogous to weather prediction, albeit concerning much larger spatial and temporal scales. Like any initial value based predictive system, this requires both a mathematical model and data from the real world. The model can fall under one of two categories; dynamical, whereby a set of equations based on physical laws determines how initial data evolves with time, and statistical models which deal in empirical relations. In the case of weather forecasting, the subject of the model is the Earth's atmosphere, whose dynamics are predicted by solving the nonlinear primitive equations. Initial data

comes from many sources, including weather stations and satellite observations. It is often the case that raw initial data are not suitable for computation, due to measurement errors or the effects of processes which are irrelevant to the forecast upsetting the balance of energy within the system. As the atmosphere is notoriously unstable, these imbalances can cause the forecast to drift away substantially from actual behaviour. In practice, data from the real world is first smoothed out and made compatible with numerical models before being used in a forecast via a process known as initialisation.

The concept of initialisation also originated in numerical weather prediction. Richardson was the first to use numerical approximations of fluid equations for the purposes of predicting pressure changes[1], which ultimately failed due to the rapid growth of initial errors. The first successful attempt was made by Charney, Fjørtoft and von Neumann[2], a one-day forecast using a numerical simulation run on ENIAC, one of the earliest electronic computers. One main difference between this forecast and Richardson's was the implementation of an initialisation scheme whereby small scale, fast oscillations associated with gravity waves were eliminated by time averaging coefficients. However, it was soon discovered that in setting these modes to zero, new problems arose. For example, where there is nonlinearity, new fast modes might be generated even if they are initially zero. From this idea came the introduction of a new scheme discovered independently by Machenhauer and Baer in which the fast modes are not eliminated entirely but held in balance with the other, slower modes of the system[3][4]. This scheme was first implemented by Tribbia to an equatorial atmosphere model[5] and then by Leith to a simulation of the mid latitudes[6]. Leith was then motivated by this nonlinear initialisation technique to introduce the concept of a slow manifold, a geometric interpretation of all the balanced states of the model as a subspace of the full state space onto which initial data is projected. Lorenz was the first to point out a connection between this slow manifold and the concept of an attractor from the field of dynamical systems[7]. The dynamical forecasting of weather and climate is indeed strongly tied to the

theory of dynamical systems, and this study will touch on both of these fields of work.

By this stage new theories on seasonal forecasting, where predictions of temporal and spatial averages could be made on the timescale of months to years, had begun to take form[8]. While day to day weather patterns become unpredictable as the scale of time is extended from days to weeks, the predictability of large scale spatial features returns for longer timescales. Since on these timescales interannual variability begins to play an important role, it was not long before the first models of the El Niño Southern Oscillation (ENSO) were to be developed.

While predecessors of comprehensive El Niño models began with early climate predictions, using Bryan and Manabe's ocean-atmosphere global circulation model (GCM), the first true ENSO simulation was developed by Anderson and McCreary[9]. Although this model was considerably less detailed than the first GCM, there was still a large degree of numerical complexity involved as it included ocean-atmosphere interactions. It was found that a two layer ocean when forced by an idealised atmosphere had oscillatory solutions with a period similar to that of ENSO. Taking another step down in complexity, Vallis developed the simplest of the early ENSO numerical models which was found to have chaotic solutions[10]. The most notable model of this era of deterministic El Niño models was the Cane Zebiak[11], which made the first accurate prediction of an ENSO event[12]. Most work which followed within this era involved stripping down the Cane Zebiak to its most basic form in an effort to understand its underlying mechanisms, such as the Battisti and Hirst delayed oscillator[13] or the Jin recharge oscillator[14], while Tziperman et al looked at the interplay between nonlinear effects and the seasonal cycle which gives rise to aperiodicity[16]. Recently, further progress has been made in the direction of minimalistic low order models, such as the simplest recharge oscillator[23] or the delayed differential model developed by Ghil et al[24]. Although the Cane Zebiak model possessed instabilities which led to some realistic ENSO events, its

deterministic nature failed to recreate realistic timeseries of the equatorial SST (sea surface temperature) anomalies over large times, which are typically far more sporadic. This shortcoming of deterministic models led to the beginning of a new era in ENSO modelling.

Second generation ENSO simulations embraced the effects of randomness, albeit at the expense of nonlinearity. An early linear empirical model from Penland and Sardeshmukh[17] was developed not from fluid equations, but from a collection of observational data and was nudged at every timestep with Gaussian white noise. Physical models soon followed suit with Kleeman and Moore introducing noise into a previously developed coupled linear model[18], and a stochastically forced version of the linearised Cane Zebiak by Thompson and Battisti[19][20].

The beginning of the third generation of ENSO models saw a merge of nonlinear and random effects. This could be seen for example in the statistical Panja Burgers simple model[21], which was a simple nonlinear oscillator (the functional form was guessed) with added white noise, or the Timmerman Jin stochastic version of a nonlinear low order model[22]. One benefit of such an approach is the irregularity of timeseries without the need for complex parameterisations. The Panja Burger model had a predictive skill close to that of modern coupled ocean-atmosphere GCMs, casting some doubt on the requirement for model complexity as far as ENSO forecasting is concerned. There may then be room for improvement as far as the predictive skill of high order models is concerned. One way to improve this is through initialisation. Xue[25] et al found that removal of dominant patterns improved the predictive skill of the Cane Zebiak model, while Chen et al[26] successfully initialised the model by data assimilation means. More complex scenarios have been treated using similar methods such as the initialisation by Ji Leetma[27] and Wang et al[28] of coupled GCMs.

The work described in this thesis is somewhere between the low order and high order approaches, making use of a new ENSO model based on work by

Jin[15] which is an extension of the 2-strip model of the equatorial thermocline with Cane Zebiak[11] sea surface thermodynamics, coupled to a heavily parametrised atmosphere. The seasonal variation of coupling is also taken into account. While noise is not introduced in the form of stochastic forcing, irregularity arises through the interaction of annual and interannual timescales, and the effect of noise on predictive skill is studied in the form of randomly perturbed initial conditions. A strategy is employed whereby a model of intermediate complexity is reduced to a low order one as a means to improve its accuracy in forecasting ENSO.

This chapter is comprised of two distinct parts. The first part establishes a context for the work to follow in this thesis, with a brief discusstion of ENSO history, modelling and theory. The second part introduces basic dynamical systems theory which will be useful in the later chapters. The next chapter derives the model which will be implemented in the initialisation experiments. Chapter three examines the solutions of several variations of the main model. ENSO-like behaviour is found in several locations within the parameter space of this model, which includes phase locking, realistic periods and amplitudes, aperiodic orbits with sensitive initial conditions, and in some cases attractors with sign asymmetry. Chapter four moves away from the subject of models altogether, describing an assortment of initialisation schemes. Predictability of one version of the main model is tested in chapter five and improved using two separate initialisation schemes based on reduction of dimensionality as a means to approximate the model attractors. This includes a linear singular value decomposition and a nonlinear approximate inertial manifold method which has so far not been tested in ENSO modelling.

1.2 El Niño and the Southern Oscillation

Every few years around December, there is a noticeable anomalous warming of the sea surface just off the Peruvian coast. While there is a certain amount

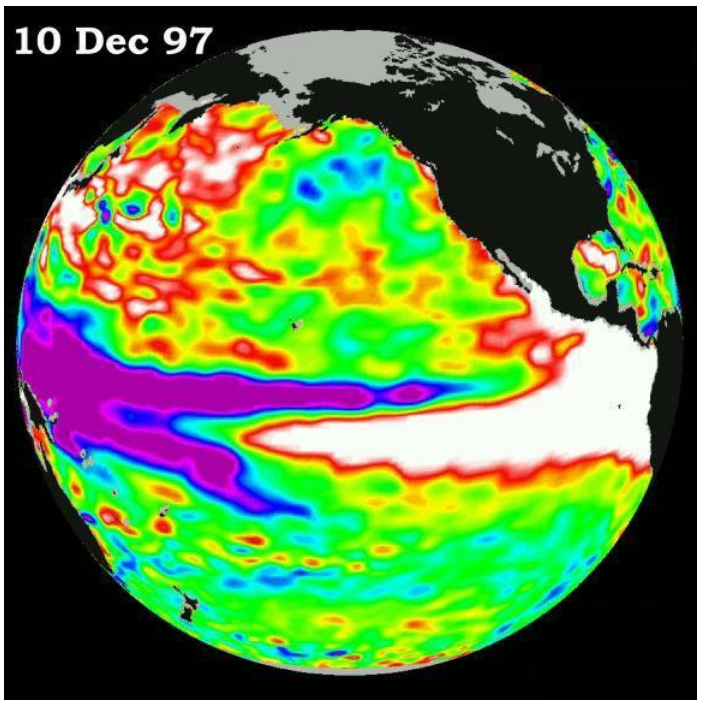

Figure 1.1: Satellite image of equatorial sea surface temperature. Positive anomalies are coloured white, and negative purple. Taken from http://photojournal.jpl.nasa.gov/.

of ambiguity as to how often this warming occurs, records confirm it is on average every four years, although the frequency spectrum is broad[29][30]. The anomaly extends over the eastern equatorial Pacific and has a characteristic spatial structure which can be seen in figure 1.1. Folklore has it that this phenomenon was first discovered by local fishermen who called it El Niño, which is a term in Spanish for the baby Jesus, due to the time of year when it is most intense. It is likely that the negative effect this had on the anchoveta populations sparked such interest from the fishing community. Interest spread beyond this local community in the mid 19th century, since the fluctuating anchoveta population was wiping out sea birds whose guano was an important export for Peru. It was not until the late 20th century that the infamy of the

El Niño reached global proportions, when a large event caused the collapse of the entire Peruvian fishing industry, stimulating worldwide scientific research.

In the early 20th century, on the other side of the Pacific ocean, the British meteorologist Gilbert Walker was Director-General of Observatories in India. Famines caused by the droughts in 1877 and 1899 had generated a great deal of interest in monsoon prediction. After a failure of the monsoon led to another drought in 1918, Walker organised groups of statisticians to examine correlations in weather patterns. They found that positive pressure anomalies on one side of the equatorial Pacific tended to coincide with negative anomalies on the other. The evidence was pointing towards the existence of a global anomalous pressure fluctuation, with an irregular, interannual period which Walker called the Southern Oscillation[31]. It is unlikely, however, that he was aware 1877, 1899 and 1918 were all El Niño years, which is intimately linked with the Southern Oscillation. Research interest soon waned since knowledge of the Southern Oscillation did not appear to be of any use in predicting monsoons, and peer scepticism prevailed.

It was not until 1969 that Bjerknes proposed the El Niño and the Southern Oscillation were both aspects of the same thing: what has now come to be known as the combined acronym ENSO. Normally in the equatorial Pacific, surface atmospheric pressure is low over a warm pool of water to the west, while in the east the ocean is cooler and the atmospheric pressure is higher. This pressure difference gives rise to trade winds blowing westward, a mechanism Bjerknes named the Walker Circulation. The ocean is in constant circulation, with water cooling and sinking at the poles and moving towards the equator where it it warms and rises before heading back toward the poles. During an El Niño event, a positive increment in sea surface temperature in the east Pacific ocean reduces the equatorial atmospheric pressure gradient, weakening easterly winds and allowing warm water to escape the pool in the west Pacific. This change in gradient brings about a drop in the rate of rising cool water, explained with more detail in the next chapter, leading to an increase in sea surface temperature

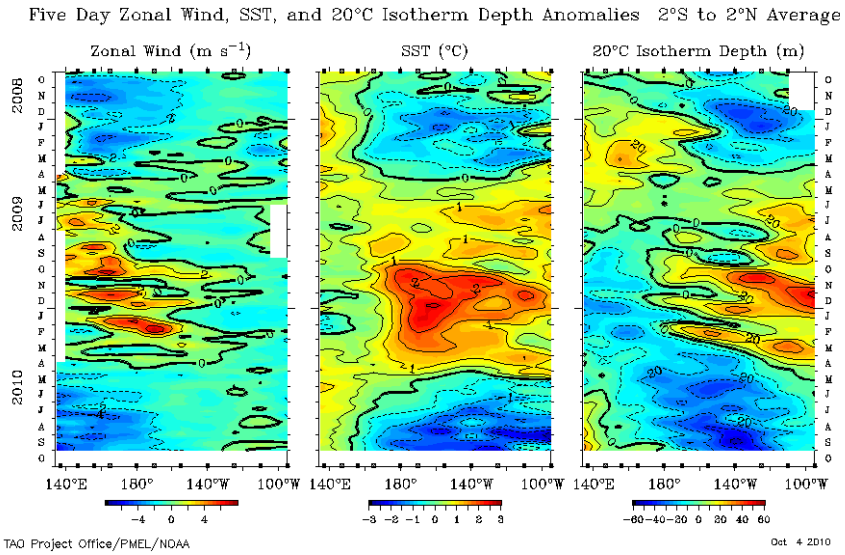

Figure 1.2: Observational data showing the growth and decay of an ENSO event in zonal wind, SST and isotherm depth. Taken from http://www.pmel.noaa.gov/tao/.

and a further reduction of the pressure gradient. An example of a recent event (2009-10) can be seen in the image 1.2: from top to bottom, a deepening of the thermocline accompanies a positive increase in SST in the east. Bursts of zonal winds from the west further deepen the thermocline and warm the sea surface until a large anomaly has spread over the Pacific basin. This process is known as Bjerknes feedback. Anomalous conditions reign for around one year, usually followed by what are known as La Niña conditions. Essentially this is an inverted El Niño, with a cold sea surface temperature in the east and reinforced trade winds. This chain of events reoccurs sporadically; a global climatological phenomenon arising through interactions between the ocean and the atmosphere[32][35].

Temporal aspects of ENSO behaviour can be seen in figure 1.3, which shows a timeseries plot of sea surface temperature for the indices Niño4, in the western tropical pacific, Niño3 to the east and Niño3.4 in between. There are noticeable peaks beginning at 1972-73, a second larger one a decade later at 1982-83 and

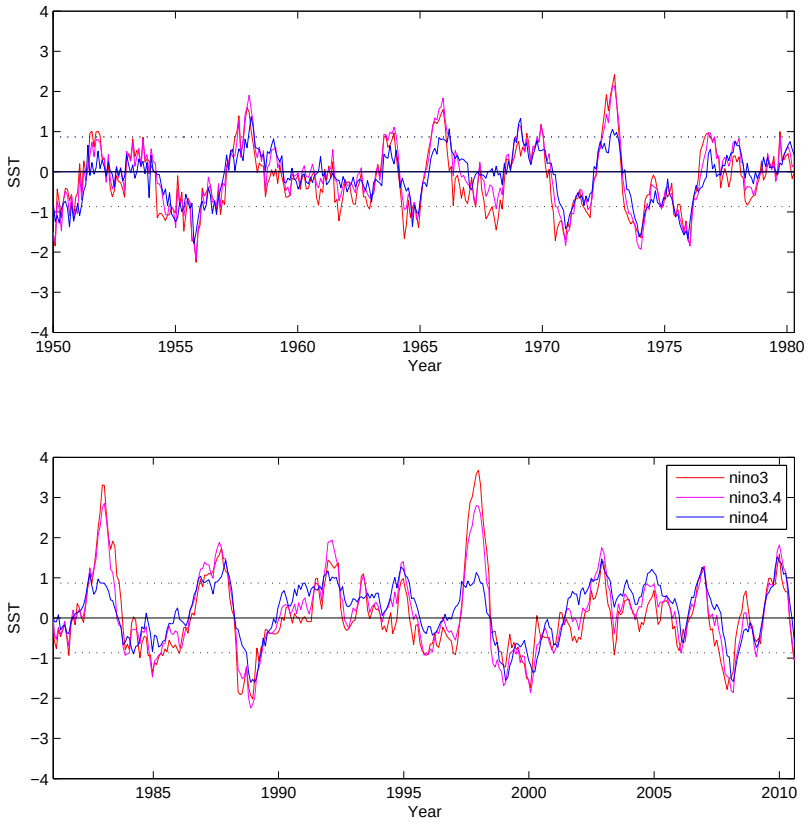

Figure 1.3: Observed equatorial SST since 1950 in the Niño3 (eastern central pacific), Niño3.4 (mid-central pacific) and Niño4 (western central pacific) regions. Taken from http://www.cpc.noaa.gov/data/indices/.

finally the largest peak in 1997-98. Each event had a significant effect on the course of human history, which will now be discussed.

1.3 Brief History of ENSO

In order to justify the efforts made to understand and accurately forecast El Niño, it is worth looking at some case studies where the phenomenon has had serious social and economic impacts. Catastrophes in the past have been connected with El Niño events, with some radical examples being the Irish potato

famine and the sinking of the Titanic[33]. However, these connections are speculative and insufficient evidence exists in meteorological data to prove that ENSO was indeed related to these events. It was not until the latter half of the 20th century that there was enough documentation and scientific records to conclude that the phenomenon was indeed responsible for adverse weather patterns or natural disasters. More detail on the following impacts can be found in Glantz[32].

1.3.1 1972-73 El Niño

This was the most intense event since the 19th century, resulting in a poor monsoon which hindered food production in India. Agriculture was also negatively affected in Russia and China. The consequences were far more drastic for Ethiopia, where there was massive social upheaval after hundreds of thousands starved to death due to famine brought on by drought. It was this event which first attracted the attention of the scientific community, although little is known about it compared with the major El Niño which came a decade later, the most retrospectively analysed event to date.

1.3.2 1982-83 El Niño

At this stage the ENSO mechanism was not wholly understood, and observational data from the ocean was limited. Subsequently this major event, whose onset was unlike that of 1972-73, was not foreseen. Severe droughts were observed in Australia resulting in large scale bush fires, and also in Indonesia, Africa and South America, seriously affecting food production. Floods were also observed in the Americas and Europe inducing landslides and mass evacuation, and the cost to the world ecomony was on the scale of billions of US dollars. The consequences of this event were the impetus for a wave of scientific research, in an effort to find new ways to accurately observe, model and predict the phenomenon.

1.3.3 1997-98 El Niño

The drastic 1997 event resulted in the hottest global temperature since records began, drought and forest fires in Indonesia and major flooding in Ecuador and Peru. Northern China was devastated by flooding when the Yangtze river burst its bank in several places, resulting in the the deaths of at least 3000 people, the evacuation of 15 million and a total cost of nearly 30 billion US dollars. The following 1998-99 La Niña produced more favourable conditions for the formation of Atlantic hurricanes, contributing to the strength of Hurricane Mitch, which resulted in the deaths of over 11,000 in Central America[34].

1.4 ENSO Modelling

The intense El Niño events in the early 70s and 80s were the initial stimulus to develop a theory which could explain the dynamical processes involved. A study of marine and observational satellite data by Rasmusson and Carpenter of six separate ENSO events since 1949 provided a foundation upon which many of the models to follow were based[29].

1.4.1 The Hierarchy of Climate Models

A climate model is a mathematical or computational entity which takes in information about some state of the ocean and atmosphere as input, processes this via some formula, and generates new information describing how this state changes with time as output. It is the tool a climate scientist uses to predict the future environment, and also to help understand the mechanisms causing things to happen. These are typically comprised of differential equations that deal with the rate of change of physical quantities in terms of the quantities themselves. Provided these terms are linear, in that they are not of order quadratic or higher, an analytic solution is almost always possible to obtain. Reality, however, is riddled with nonlinearities which render these equations unsolvable. This is especially true for partial differential equations, involving

quantities which vary in space as well as time. The best way to progress in such a situation is to use numerical methods, although a computer model is unable to deal with smooth functions due to the infinities involved in probing arbitrarily small scales. Governing equations must be approximated in such a way that they can be translated into the language of finite integers for a computer to understand them.

It is at this stage possible to introduce the so-called hierarchy of models. The complexity of a model is typically related to its dimensionality. This is the number n of first order in time differential equations which are the variables required to define the state of the system. Numbers which do not vary in time are known as parameters. There is an upper bound on the value of n due to the technological limitations of computational power, below which is the position of general circulation models (GCMs) to be described shortly. The middle range is inhabited by the intermediate, which would usually focus on a particular climatological phenomenon. At the bottom of the scale are the conceptual, drastically simplified versions of the GCMs or intermediate models. ENSO, being one of the most dominant sources of climate variability, has been modelled on just about every scale which is physically justifiable, but it is the mid range of complexity which has yielded the most insight; the best example of this being the Cane Zebiak model which will be described in more detail later[37][36].

1.4.2 General Circulation Models

The most powerful tools available for climate prediction are the general circulation models, representing a holistic approach to the climate problem. These are numerical codes which calculate physical properties of the ocean and atmosphere over the entire planet for up to centennial timescales. Most of the computation is involved with the time integration of the full primitive equations. The ocean and atmosphere are assumed to be in hydrostatic equilibrium and both are driven by the influx of solar radiation. Indeed every process which

affects the motion such as clouds, geographical features and static sea ice are incorporated. The most well-known limitations to the accuracy of GCMs are the finite resolution of scale, and physical processes such as atmospheric turbulence and sea ice dynamics which are not yet wholly understood.

The first GCM was developed by Manabe[38], which was atmosphere-only, forced by a fixed heat distribution at the surface. Bryan[39] later developed the first ocean model, driven by a prescribed surface wind stress. These basic models were combined to create the first coupled ocean-atmosphere GCM (CGCM)[40] describing a planet with land in the western hemisphere, ocean in the east, and no north or south pole. Bjerknes feedback had remained an untested hypothesis until it was first confirmed using a similar model[41].

Modern GCMs typically require an order of 10^6 or higher numbers to specify the state of the climate at any point in time; for example HadGEM1, a coupled ocean-atmosphere model developed by the UK Met office which also incorporated sea ice. With roughly 200 zonal, 150 meridional and 50 vertical grid points with 4 variables ascribed to each point, over 5 million numbers were required to specify its state[42]. However, this is still not enough to resolve the length-scales responsible for atmospheric turbulence and other physical phenomena. This is done using a parametrisation, an expression that gives an approximate representation to real world processes using bulk formulae of variables.

1.4.3 Seasonal Forecasting Systems

While GCMs are commonly used to predict the long term impacts of climate change, they are also effective at predicting Pacific SST timeseries. Due to the coupled nature of ENSO, an ocean-atmosphere CGCM is the natural choice of predictive system. A forecast typically involves taking a group of states which are initially close to observation and integrating forward in time to provide a group of final states. This allows for the calculation of a time-evolving probability distribution, giving the relative likelihood of the future state occupying particular regions of phase space. Notable systems include those under devel-

opment at the ECMWF and UK Met Office[43][**?**].

As well as using observational data to specify the inital state, new data is assimilated into the model, nudging it towards those regions of state space which are consistent with measurements[45]. Later in the chapter the initialisation of seasonal forecasting systems is discussed again in relation to the slow manifold concept. The science of seasonal prediction relies upon top of the range models at the highest scales of complexity, and is still in its early, experimental stages. To gain a better understanding of ENSO dynamics it is worth looking back to some of the earlier, simpler forecast models beginning with the most well known.

1.4.4 The Cane Zebiak Model

Several attempts were made throughout the 1980s to develop a coupled ENSO model, stemming from an early mathematical effort by McWilliams Gent[32] and culminating in the highly successful Cane Zebiak intermediate model[11], which was the first to successfully predict the 1986 ENSO event [12]. This study simulated a section of the ocean and atmosphere in a rectangular box centered around the equatorial Pacific, 60° latitude wide and 160° longitude in length. Equations of motion for the atmosphere and ocean were linear perturbations about a mean climatological state, which varied seasonally, introducing an intrinsic annual oscillation into the model which ensured events occurred at the same time of year. Only the oceanic components were time integrated, while the atmosphere was assumed to be in equilibrium due to the much faster timescales involved. The ocean was modelled as a fluid of two layers with different densities, a thin layer above another denser layer of effectively infinite depth. The interface between the two layers, known as the thermocline, is an important concept in understanding ENSO physics and plays a leading role in the systems to be introduced later. Surface heat and moisture fluxes drove the atmosphere, and this fed back into the ocean as surface wind stress. As the linear model was unstable for some parameter choices, a nonlinear term was included which conveniently parametrised the effect of changes in thermocline depth on the sea

surface temperature. This curbed the growth of the instability, and turned out to be an accurate representation since the model reproduced a realistic ENSO. Solutions to the Cane Zebiak model using were oscillatory and irregular with a period of 3-4 years.

1.4.5 Conceptual Models

While a holistic approach to modelling yields more accurate results, the data is difficult to interpret with regards to the underlying dynamical processes. It can then be useful and illustrative to approach the ENSO problem from the other end of the complexity scale, and effectively strip away everything except the most dominant contributors to the phenomenon. The most primitive example of an ENSO model would be a simple positive feedback equation

$$\frac{dT}{dt} = \alpha T, \tag{1.1}$$

where α is a positive constant parametrising the Bjerknes feedback mechanism described earlier, and T is the sea surface temperature averaged over the eastern equatorial Pacific. Sources which contribute this value would be for example the reduction of zonal temperature gradient or an increase in anomalous zonal momentum, while an increase in upwelling of cool water from the deep ocean or the dissipation rate of heat into the atmosphere would detract from it. Provided an accurate enough value of α was chosen, this could be used to predict the early growth of an El Niño event on a short enough timescale, given some initial value of T, although this could only be carried out at the start of an event due to the oscillatory nature of the phenomenon.

The late 1980s saw the development of the conceptual ENSO models; beginning with Vallis[10], Anderson McCreary[9], Schopf Suarez[48] and Battisti Hirst[13]. Vallis studied the solutions to a system of 3 ordinary differential equations (ODEs) for zonal velocity and east/west temperature anomalies, finding chaotic solutions. The other two so-called delayed oscillator models were highly

idealised, and each could be summarised with a single delay differential equation (DDE). A DDE is a slightly more exotic variety of differential equation in that it contains a delay term; the rate of change of a variable depends on the value it took some fixed time in the past. The Bjerknes feedback equation can be converted into a DDE by including such a term

$$\frac{dT}{dt} = \alpha T - \beta T(t-\tau), \tag{1.2}$$

where τ is a timescale and β is another positive constant. Physically, the delay term corresponds to an ocean wave created by the atmospheric disturbance at time $t-\tau$ which travels for a time τ, acting to oppose the anomaly at time t. Precisely what these waves are will be explained later in the equatorial wave dynamics section. This linear DDE permits some form of oscillation; one step closer to the reality of ENSO. Unfortunately, this oscillator is unbounded and may become unphysical for large times. A further nonlinear term is required in order to stabilise growth

$$\frac{dT}{dt} = \alpha T - \beta T(t-\tau) - \gamma T^3. \tag{1.3}$$

Nonlinear stratification in the ocean provides the physical basis for inclusion of this third term. Choosing the right values of the parameters $(\alpha, \beta, \gamma, \tau)$ will yield a stable oscillation with typical ENSO period and amplitude.

A new conceptual model, the recharge oscillator, was later developed by Jin[14]. Delay terms were avoided in the recharge oscillator by extending the system to two coupled differential equations, one corresponding to sea surface temperature in the eastern Pacific and the second a measure of warm water volume in the west

$$\frac{dT}{dt} = \alpha T + \kappa h - (h + \gamma T)^3, \tag{1.4}$$

$$\frac{dh}{dt} = -\rho h - \mu T. \tag{1.5}$$

Like the previous model, this too has solutions which are oscillatory and stable. The above equations are an example of an autonomous system, for which there is no time-dependent external forcing. Originally this was derived from a more complex PDE model[15] based on wave modes on the tropical thermocline; a boundary which separates a thin surface layer of hot, turbulent water from the rest of the ocean which is predominantly cold and dense. The variable h is indicative of the depth of the thermocline, averaged over some large region in the western Pacific ocean. A similar model and the behaviour of its solutions will be described in greater depth at the beginning of chapter three.

Realistically, the variation of the influx of solar energy into the climate system throughout the seasons cannot be ignored. This introduces fixed periodicities into a model in the form of time-dependent parameters, and the differential equations which govern such models fall under the category of nonautonomous, given that they are driven by some kind of external motion. Phase locking of ENSO events to the annual cycle, or the persistence of an event to occur at a particular time of year, comes about through periodic forcing of the climate system from the seasonal variation of solar radiation. Tziperman et al showed that inclusion of the seasonal cycle in oscillatory simple models leads to chaotic behaviour[16]. Consideration of weather noise, present in all real world observations of ENSO data, leads naturally to the introduction of stochastic forcing, and another important class of nonautonomous differential equations. The Panja Burgers model consists of a pair of stochastic, nonlinear differential equations with parameters chosen to maximise predictive accuracy, model loosely based on the recharge oscillator idea. As a forecast model, this accuracy compares well with some top of the range models [21]. There is an ongoing debate as to whether ENSO irregularity is a result of deterministic chaos or stochastic randomness, with evidence supporting both arguments [11][20]. Understanding the various mechanisms underlying ENSO behaviour can be achieved through conceptual modelling, and the best way to understand the behaviour of low order models is within the framework of dynamical systems.

1.5 Continuous Time Dynamical Systems

The intention of this section is to act as a brief introduction to dynamical systems theory, as much of the concepts herein shall be used throughout this study. It should be clear at this point that differential equations form the basis of dynamical forecasting. While there is no disputing their usefulness in prediction, a deeper understanding can be gained through a geometric treatment of the system as flows in a vector field. Along with this new perspective comes many useful tools and analytical techniques for the climate scientist, together with a theoretical framework within which all models can be discussed and compared. Many of the basic concepts described here are discussed in more depth in Drazin[49] or Jordan and Smith[50]. The most general definition of a dynamical system is that it consists of a phase space, with every point in this space corresponding to the state of the system at any given time, and an evolution rule which describes how each point in the space evolves with time. For most cases, the phase space is the n dimensional Euclidean space $\mathbb{R}^n$. Each evolution equation contributes another dimension to the phase space of a system. Thus, for the Bjerknes feedback equation $n = 1$, for the recharge oscillator $n = 2$, for a GCM $n \sim 10^6$ and so on.

Consider

$$\frac{d\mathbf{x}}{dt} = \mathbf{f}(\mathbf{x}), \tag{1.6}$$

where $\mathbf{x}(t)$ is a vector, $\mathbf{x}(0) = \mathbf{x}_0$ and f is a continuous vector function. The dynamic quantities are held in $\mathbf{x}$, the evolution law in $\mathbf{f}$, and $\mathbf{x}_0$ is known as the initial condition. If $\mathbf{f}$ is a linear function of $\mathbf{x}$, the equation can be rewritten

$$\frac{d\mathbf{x}}{dt} = A\mathbf{x}, \tag{1.7}$$

where A is a matrix operator whose elements are constant coefficients, acting on $\mathbf{x}$. This can be solved in exactly the same way as (1.1), the only difference

is that A is a matrix and not a scalar,

$$\mathbf{x}(t) = e^{At}\mathbf{x}(0). \tag{1.8}$$

e^{At} is known as an evolution operator. For example in $\mathbb{R}^2$, take the matrix

$$A = \begin{pmatrix} 0 & -1 \\ 1 & 0 \end{pmatrix}. \tag{1.9}$$

The square of this matrix is

$$A^2 = \begin{pmatrix} -1 & 0 \\ 0 & -1 \end{pmatrix} = -I, \tag{1.10}$$

where I is the identity matrix. This would imply

$$A^n = (-I)^{n/2}, \tag{1.11}$$

for even values of integer n and

$$A^n = (-I)^{(n-1)/2}A \tag{1.12}$$

for n odd. Now, since

$$e^x = \sum_{n=0}^{\infty} \frac{x^n}{n!}, \tag{1.13}$$

replacing x with At and using the expressions for A^n yields

$$e^{At} = I(1 - \frac{t^2}{2!} + \frac{t^4}{4!} - \cdots) + A(t - \frac{t^3}{3!} + \frac{t^5}{5!} - \cdots), \tag{1.14}$$

where the series has been separated into odd and even powers. The solution is

$$x(t) = \begin{pmatrix} \cos t & -\sin t \\ \sin t & \cos t \end{pmatrix} x(0). \tag{1.15}$$

Notice that the evolution operator on the right hand side is actually the rotation matrix. All initial points are then rotated, after a time t, by an angle t about the origin. The solutions then are constrained to a circle of radius $|x_0|$ centered at the origin, returning to their original position whenever t takes on integer values of 2π, and all points on the circle are different instances of the same solution. Every point $\mathbf{x}(t)$ is an initial condition itself

$$\mathbf{x}(t+s) = e^{As}\mathbf{x}(t), \tag{1.16}$$

where s is an arbitrary timescale. An orbit is defined as the set of all points $\mathbf{x}$ passes through when it is operated on by e^{At} as $t \to \pm\infty$. It represents the entire past and future of a single state. Since this study is concerning climate forecasting, only times $t > t_0$, the initial time, are important. The above expression leads naturally to the linear condition

$$e^{A(t+s)} = e^{At}e^{As} = e^{As}e^{At}, \tag{1.17}$$

which generalises in the abstract, nonlinear case to

$$S(t+s) = S(t)S(s) = S(s)S(t), \tag{1.18}$$

for solution operator S, due to the fact that there is a unique direction of the flow at every point in the phase space. This is at the heart of dynamical systems as it is the condition for determinism; an orbit starting at the same location always has the same destiny. Once an initial point is chosen, so too is the past and future of that point.

1.5.1 Fixed Points

The fixed points of a dynamical system are those which satisfy

$$\frac{d\mathbf{x}}{dt} = 0. \tag{1.19}$$

If a point in the phase space satisfies this condition, its orbit remains there for all time. It is an example of an invariant subspace, since it is left unchanged when acted on by the evolution operator. While a linear system has one fixed point (or none if the determinant of A is zero), a nonlinear system can have any number. An important property of fixed points is their stability, which determines how a state vector evolves when perturbed from a fixed point. Equation (1.1) possesses what is an example of an unstable fixed point at $x^* = 0$. The slightest increment $\pm\delta x$ will send $x \to \pm\infty$, so the origin is a point which repels all orbits.

If α was negative, the fixed point would be stable, and the origin would attract all orbits. This is the first example of an attractor; an invariant subspace which attracts orbits as time progresses.

For higher dimensional systems, the stability of fixed points can be found via the Jacobian matrix J. This is given by the partial derivatives of the vector function $\mathbf{f}(x)$ evaluated at the fixed point $\mathbf{x}^*$. If $\mathbf{x} = (x_1, x_2, \cdots, x_n)$, and $\mathbf{f}(\mathbf{x}^*) = (f_1, f_2, \cdots, f_n)$, then

$$J(\mathbf{x}^*) = \begin{pmatrix} \frac{\partial f_1}{\partial x_1} & \cdots & \frac{\partial f_1}{\partial x_n} \\ \vdots & \ddots & \vdots \\ \frac{\partial f_n}{\partial x_1} & \cdots & \frac{\partial f_n}{\partial x_n} \end{pmatrix}. \tag{1.20}$$

For a two-dimensional autonomous system it can be shown that the eigenvalues of J satisfy the quadratic equation

$$\lambda^2 - \gamma\lambda + \delta = 0, \tag{1.21}$$

where (γ, δ) are the trace and determinant of J. The solution

$$\lambda = \frac{1}{2}\left(\gamma \pm \sqrt{(\gamma^2 - 4\delta)}\right), \tag{1.22}$$

is real provided $\gamma^2 \geq 4\delta$, and corresponds to a stable solution when $\gamma \leq 0$. Stable solutions can always be converted into their unstable counterpart via

time reversal, where $\lambda \to -\lambda$, leaving the following distinct possible regimes (see figure 1.4 for graphical representations)

- $\delta < 0$: a saddle point, which attracts orbits in one direction and repels in the other, and is hence never stable.
- $\delta \geq 0$, $\gamma^2 \geq 4\delta$: a sink/source which absorbs/repels in all directions and is always stable/unstable
- $\delta \geq 0$, $\gamma^2 < 4\delta$: a stable/unstable spiral similar to above but the trajectories revolve around the attractor. There is therefore some ambiguity surrounding the direction of orbits in the vicinity of the fixed point.
- $\delta \geq 0$, $\gamma = 0$: a centre, being a special case where orbits form a family of ellipses around the fixed point whose axes are determined by the initial conditions and the relative magnitudes of the two purely imaginary eigenvalues.

To each eigenvalue Λ_i of J, there is a corresponding eigenvector v_i, satisfying

$$J\mathbf{v}_i = \Lambda_i \mathbf{v}_i. \tag{1.23}$$

The eigenvectors reveal information about the local geometry of orbits, specifically the direction of orbits in the vicinity of a fixed point. If these vectors are sorted into classes according to the real parts of their eigenvalues, some new varieties of subspaces, the eigenspaces, can be defined

- E^u is the manifold spanned by the eigenvectors with eigenvalues satisfying $\Re(\Lambda_i) > 0$,
- E^s is the manifold spanned by the eigenvectors with eigenvalues satisfying $\Re(\Lambda_i) < 0$,
- E^c is the manifold spanned by the eigenvectors with eigenvalues satisfying $\Re(\Lambda_i) = 0$.

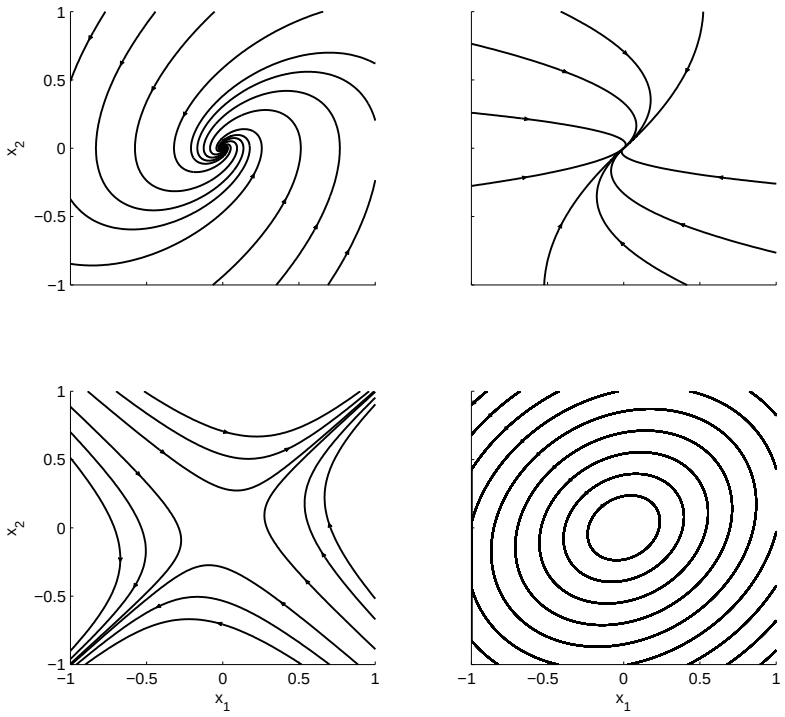

Figure 1.4: Phase space representation of a linear system in two dimensions, depicting a stable spiral (top left), sink (top right), saddle (bottom left) and centre (bottom right).

For linear systems, these subspaces are invariant, and $S(t)\mathbf{x} \in E$ for $\mathbf{x} \in E$. The term manifold is, roughly speaking, a higher (or lower) dimensional generalisation of a surface which looks locally like R^n. For example, one vector defines an infinitely long straight line, two vectors define an infinite plane and so on. Globally for a nonlinear system, a more general definition is required since these subspaces will not be invariant.

- W^u is the set of points satisfying $S(t)\mathbf{x} = \mathbf{x}^*$ as $t \to -\infty$,
- W^s is the set of points satisfying $S(t)\mathbf{x} = \mathbf{x}^*$ as $t \to +\infty$.

Much like the orbits, these usually can only be calculated numerically. While these manifolds will not be used, it is important to introduce global invariant

manifolds at this stage as they form a basis for the analytical approach to initialisation which is discussed further in chapter four.

1.5.2 Limit Cycles

More relevant to ENSO are orbits in phase space which correspond to oscillatory motion, satisfying $\mathbf{x}(t+\tau) = \mathbf{x}(t)$. These have already been touched on in the previous section, with the introduction of centre fixed points, where a closed curve in the phase space defines a periodic orbit. In the macroscopic reality, such idealistic cases are unlikely due to thermodynamical considerations. Real systems typically dissipate energy and tend towards an attractor of some kind, although orbits would be constantly perturbed by noise so never strictly settle on the attractor. Just as there exist stable fixed points and stable surfaces, there can exist stable closed curves, limit cycles, which attract orbits. The main difference between limit cycles and centres is that, while the amplitude of a centre is defined by its initial conditions, the amplitude of a limit cycle is independent of its initial conditions, and depends on the parameters and nonlinearity of the function $\mathbf{f}(\mathbf{x})$. For the right parameter values, it can be shown that the set of equations (1.4), (1.5) possess limit cycles solutions, and with the right period and amplitude could be used to forecast an El Niño event. One analytic example is the set of equations

$$\frac{dx}{dt} = x - y - x(x^2 + y^2) \tag{1.24}$$

$$\frac{dy}{dt} = x + y - y(x^2 + y^2). \tag{1.25}$$

Under a transformation to polar coordinates, this simplifies to

$$\frac{dr}{dt} = r(1 - r^2) \tag{1.26}$$

$$\frac{d\theta}{dt} = 1. \tag{1.27}$$

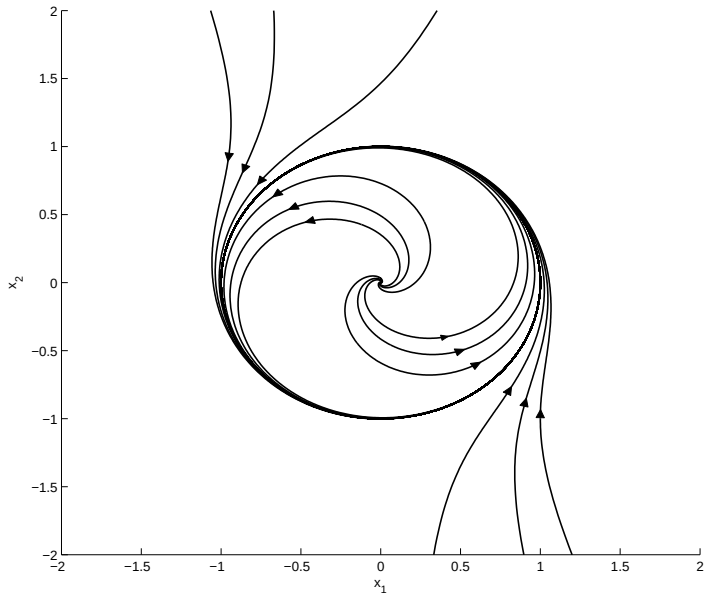

Figure 1.5: Phase space representation of limit cycle described by (1.26), depicting the absorption of several orbits onto the circle of radius $r = 1$.

The set of points at $r = 1$ attract orbits from the entire space, and there is an unstable fixed point at $x = y = 0$. All trajectories revolve around this point at a constant rate, and the attractor is a circle of unit unit radius (see figure 1.5). Like fixed points, limit cycles can be stable or unstable. On a small enough scale in the vicinity of the origin, orbits of a stable (unstable) limit cycle behave as they would around an unstable (stable) fixed point, and on a large enough scale they behave as if the limit cycle was a stable (unstable) fixed point. Unlike fixed points, a limit cycle or a centre cannot exist in a $\mathbb{R}^1$ phase space, since an orbit cannot change direction in a space where the flow is single valued. In other words, the minimum embedding dimension of a limit cycle is 2. The Poincaré-Bendixson theorem states that, in $\mathbb{R}^2$, the only possible bounded solutions tend towards fixed points or limit cycles.

1.5.3 Bifurcations

Two types of attractor have been discussed so far, the fixed point and the limit cycle. Given a dynamical system of the general form (1.6), it is useful to develop an understanding of how the equations describing the time evolution can give rise to different attractors, and how one attractor can change into another. When modelling any physical system, understanding bifurcations is essential because they determine how the topology of orbits can change drastically by varying model parameters even slightly.

Saddle-node Bifurcation

Consider the system in $\mathbb{R}^1$

$$\frac{dx}{dt} = a - x^2, \tag{1.28}$$

where the parameter a is a real number. Fixed points occur at $x = \pm\sqrt{a}$. Linearising about these points for small $\hat{x}$ gives

$$\tfrac{d\hat{x}}{dt} = 2\sqrt{a}\hat{x} \quad \tfrac{d\hat{x}}{dt} = -2\sqrt{a}\hat{x}, \tag{1.29}$$

for $x = \sqrt{a}$ and $x = -\sqrt{a}$ respectively. There is no solution for $a < 0$, and two solutions for $a > 0$, one stable and the other unstable (see figure 1.6). Decreasing a from some positive value brings these solutions closer together, ultimately annihilating each other at $a = 0$.

Transcritical Bifurcation

Now consider

$$\frac{dx}{dt} = ax - x^2. \tag{1.30}$$

Fixed points occur at $x = (0, a)$, and linearising about $x = 0$ and $x = a$ gives

$$\tfrac{d\hat{x}}{dt} = a\hat{x} \quad \tfrac{d\hat{x}}{dt} = -a\hat{x} \tag{1.31}$$

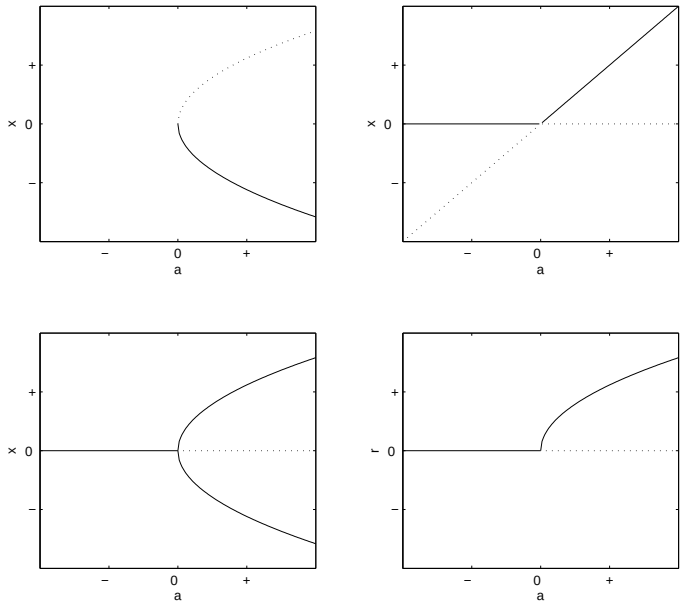

Figure 1.6: Bifurcation diagrams for saddle node (top left), transcritical (top right), pitchfork (bottom left) and Hopf (bottom right).

respectively. For values of $a < 0$, the zero solution is the only stable one, but for a positive, the origin is unstable and the equilibrium is at $x = a$. The exchange of stability which occurs at $a = 0$ gives the bifurcation its name.

Pitchfork Bifurcation

In the case where

$$\frac{dx}{dt} = ax - x^3, \tag{1.32}$$

there are fixed points at $x = (0, \pm\sqrt{a})$. Linearising about $x = 0$ and $x = \pm\sqrt{a}$ gives

$$\frac{d\hat{x}}{dt} = a\hat{x} \quad \frac{d\hat{x}}{dt} = -2a\hat{x} \tag{1.33}$$

Clearly for $a < 0$ there are no solutions other than $x = 0$, which is stable. As a crosses zero, again the origin loses stability and there are stable equilibria at $x = \pm\sqrt{a}$. Geometrically speaking, the point attractor splits into a pair of point

attractors, and the final state of the system depends on the initial value of x. The name comes from the three-pronged shape of the bifurcation diagram.

Hopf Bifurcation

Supposing the previous example is taken into the complex plane, so that

$$\frac{dz}{dt} = \lambda z - |z|^2 z, \tag{1.34}$$

where $z = x + iy$ and $\lambda = a + ib$. When written in polar form $z = re^{i\theta}$, there are two equations. The equation for modulus is identical to that of the pitchfork bifurcation,

$$\frac{dr}{dt} = ar - r^3, \tag{1.35}$$

with $r \geq 0$, while the argument

$$\frac{d\theta}{dt} = b, \tag{1.36}$$

just gives the rate of an orbit about the origin as the imaginary part of the parameter λ. As for the pitchfork bifurcation then, the origin is the attractor for $a < 0$, and for $a > 0$, the circle of modulus $\sqrt{a}$. This kind of bifurcation describes the birth of a limit cycle.

1.5.4 Strange Attractors

The Rössler System

Extending the phase space to $\mathbb{R}^3$ allows for the existence of bounded orbits which are neither closed curves or isolated points. Rather, they form a fractal set whose trajectories are highly sensitive to initial conditions. This sensitivity to initial conditions places a limit on the predictive skill of a dynamical system whilst operating in such a regime. The simplest example is the 3-dimensional

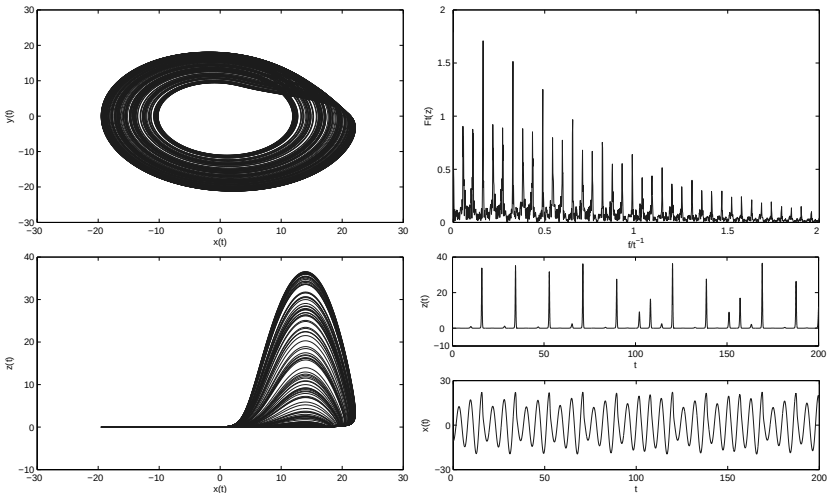

Figure 1.7: Phase plot, frequency spectrum and timeseries of the Rössler attractor with $(a, b, c) = (0.1, 0.1, 14)$.

Rössler system,

$$\begin{aligned}\frac{dx}{dt} &= -y - z \\ \frac{dy}{dt} &= x + ay \\ \frac{dz}{dt} &= b + (x - c)z.\end{aligned}$$

There are two fixed points for this system, the origin $\mathbf{x}^* = 0$ and the point $\mathbf{x}^* = (c - ab, -(c - ab)/a, c - ab/a)$, neither of which are stable. For each fixed point there is a periodic orbit (see figure 1.7), and trajectories jump between these orbits in an apparently sporadic manner.

To understand the process intuitively it is useful to consider the topological properties of this new kind of attractor. First to be noted is that strange attractors have zero volume. Orbits are effectively constrained to thin ribbon-shaped regions of phase space. The Rössler system consists of two conjoined ribbon types; one forming an annulus and the other a mobius band. Orbits move

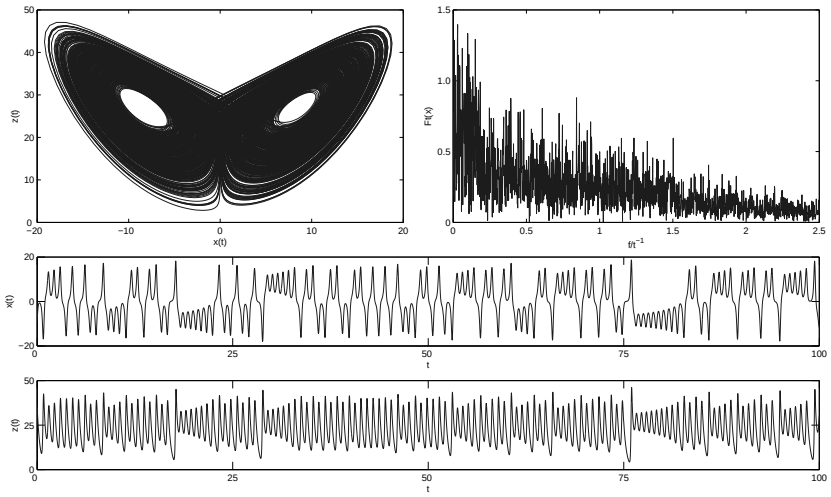

Figure 1.8: Phase plot, spectrum and time series of the Lorenz attractor with $(\sigma, r, b) = (10, 28, 8/3)$.

counter-clockwise along these ribbons. At one point in the circuit a branching occurs, whereby an orbit can choose to either continue along on the annulus or switch to the mobius band. Every choice will depend entirely on the initial conditions, and the introduction of choice brings unpredictability, as two arbitrarily close orbits can choose to follow completely separate paths. Orbits fill the bounded space of these ribbons, jumping from one periodic orbit to another and giving rise to solutions which are oscillatory with an infinite period, never settling down to a repeating pattern.

The Lorenz System

A better known example of chaos was discovered by Lorenz[53], in a simple convection model describing a layer of fluid in two dimensions. The top and bottom surfaces are held at different constant temperatures. After discarding most terms, the result is another aperiodic dynamical system in 3 dimensions,

$$\begin{aligned}\frac{dx}{dt} &= \sigma(y-x)\\ \frac{dy}{dt} &= -y + x(r-z)\\ \frac{dz}{dt} &= -bz + xy.\end{aligned}$$

The fixed points in this case are, along with the origin, the pair $\mathbf{x}^*(\pm\sqrt{(}b(r-1)), \pm\sqrt{(}b(r-1)), r-1)$. When $r > 1$, one eigenvalue of the Jacobian about these points is negative, and the remaining two are complex conjugate pairs. There a critical value of r at $r_c = \sigma(\sigma+b+3)/(\sigma-b-1)$. At subcritical values where $1 < r < r_c$, the real part of the conjugate pairs is negative, and orbits will spiral into these twin fixed point attractors. Beyond r_c, the real part is positive, resulting in a symmetric pair of periodic orbits. Trajectories, as shown in figure 1.8, revolve around a fixed point momentarily before jumping to the other.

This can be thought of geometrically as two annuli, centered at the points $(\pm\sqrt{(}b(r-1)), \pm\sqrt{(}b(r-1)), r-1)$. The orbits move around the left hand annulus clockwise and the right hand counter-clockwise. These annuli are conjoined in the vicinity of the origin, where an orbit can choose to move around the left hand or right hand annulus. As with the Rössler attractor, the minimum embedding dimension of the Lorenz attractor is 3.

1.5.5 Lyapunov Exponents

While an orbit defines the path of a single point through phase space, there is much to be learned from analysing the time evolution of areas, volumes and higher dimensional generalisations of these concepts. Obtained is a spectrum of real numbers, called Lyapunov exponents, which determine the fate of a volume element for large times and the attractor dimension of a system. The number of exponents is equal to the dimensionality of the phase space. Qualitatively

speaking, trajectories which are initially close diverge in a chaotic system, and their separation will grow in time by a factor $e^{\lambda t}$, where λ is the Lyapunov exponent. The idea is to look at the evolution of an infinitesimal n-dimensional sphere as it travels through phase space. Mathematical rigour requires first a definition of the tangent space for the point at the centre of the sphere, since the phase space can only define vectors which have a base at the origin. Lyapunov exponents are calculated by integrating the nonlinear equations to give the time evolution of x, while simultaneously calculating the evolution of a set of basis vectors in the tangent space of x

$$\begin{aligned} \frac{d\mathbf{x}}{dt} &= \mathbf{f}(\mathbf{x}), \\ \frac{d\mathbf{e}_i}{dt} &= J(\mathbf{x})\mathbf{e}_i, \end{aligned}$$

and the result is a set of numbers providing the average growth or decay rates of a volume over the full phase space. The concept of Lyapunov exponents is also important in the classification of attractors. Taking the example of $\mathbb{R}^3$, a fixed point is characterised by three negative exponents $(-,-,-)$. As an orbit approaches a fixed point, the set of basis vectors in the tangent space are all decaying and as a result a volume element shrinks to a point. A limit cycle has two negative and one zero exponent $(-,-,0)$. Two dimensions shrink while the third is unaffected, since two points on the limit cycle will not grow further apart or closer together, resulting in a one dimensional attractor. In other words, the zero corresponds to translation of a volume element. Similarly, two zero Lyapunov exponents $(-,0,0)$ arise where the attractor is in the shape of a torus. The remaining possibility is where there is one positive exponent $(-,0,+)$, whereby the volume element shrinks into a thin ribbon which is then stretched apart. A dynamical system with at least one positive exponent is by definition chaotic.

The concept of Lyapunov exponents leads naturally to that of the predictability of nonlinear systems. Imagine a sphere is allowed to evolve near

an attractor with a $(-, 0, +)$ spectrum. This is similar to an ensemble forecast whereby a group of states (in practice a finite number, but in theory continuously many) close to the initial state $\mathbf{x}_{t_0}$ are evolved to a time $t_0 + t$ and statistical properties of this group are measured rather than the details of individual trajectories. Firstly, the sphere will flatten out into a disk. The circle will continue to translate until it reaches a branching point $\mathbf{x}^*$, where an eigenvalue of the Jacobian $J(\mathbf{x}^*)$ crosses zero and becomes positive, and the disk will be stretched apart. It is at this point that states will begin to diverge, and if ξ_0 is the average distance between two states on this disc, it will evolve as

$$\xi(t) = \xi_0 e^{\lambda t}, \tag{1.37}$$

where λ is the positive Lyapunov exponent. Now, from a forecast point of view if ξ is the distance between an erroneous vector and the true state of a system, even if initially small, it may grow until the error state and true state are unrecognisable. Thus, a cloud of initially close states will spread out into the phase space as a plume. After some fixed forecast time t_f, the width of the plume, which is related to the magnitude of λ and the initial radius of the sphere of states, is a measure of the predictability of a system, and the growth rate of errors. Ultimately, since the attractor is bounded these states must at some point converge. The length of time for which the forecast is reliable and uncorrupted by error then depends on which point on the attractor it is initiated, or where the sphere of states is released and allowed to evolve. This is discussed by Palmer et al[55] in the context of weather and climate prediction.

1.5.6 Branched Manifolds

In the Lorenz and Rössler systems, the trajectories after large times live in a space which is nearly two dimensional, and characterised by the topology of these trajectories. This space is known as a branched manifold, owing to the presence of singularities at the point where orbits diverge which do not

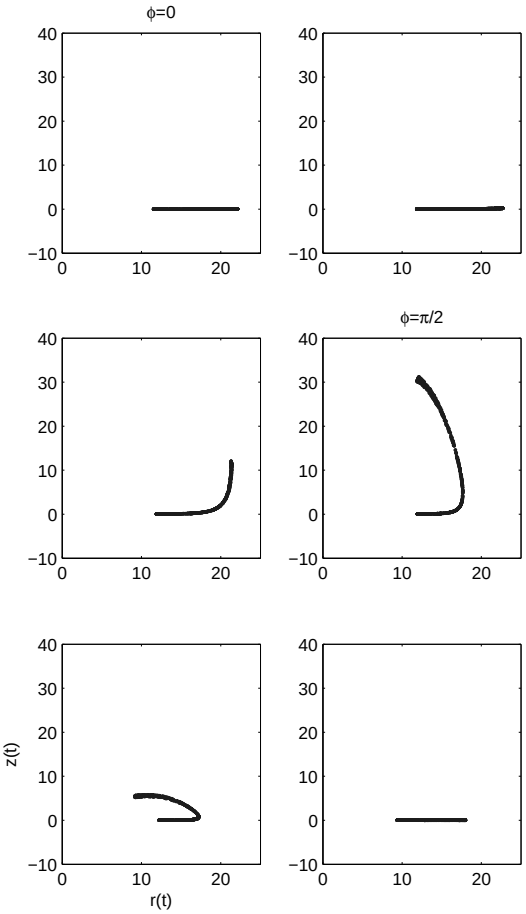

Figure 1.9: Poincaré section of the Rössler attractor in the $(r = \sqrt{x^2 + y^2}, z)$ plane as a function of phase ϕ. Intersections of the orbits with the (r, z) plane at various angles $\phi_i = (i-2)\pi/6$, $i \in [0, 5]$ show clearly the overlapping feature of the attractor as seen in the $(+x, +y)$ quadrant of figure 1.7.

permit the space to be described using the same mathematics as a differentiable manifold. A step above delving into the fractal structure of attractors, this template structure could be the closest guess to the attractor shape for low order systems. There are some potential benefits for the initialisation problem, whose aim is to project onto a set of coordinates which parametrises the attractor using the smallest number of dimensions possible.

With regards to the idea of branched manifolds, there is the Birman-Williams projection coming from the theorem of the same name[56]. This states that two

orbits $x(t)$ and $y(t)$ are equivalent if

$$|x - y| \to 0 \tag{1.38}$$

as $t \to \infty$, or they have the same asymptotic future. This constraint projects orbits onto the manifold which characterises the attractor. A negative Lyapunov implies a volume is exponentially shrinking in a direction perpendicular to the flow, and the limit is the branched manifold. This theorem has not been generalised beyond dimension 3, but the exponentially attracting subspace is a concept similar to the inertial manifold for systems of arbitrary dimension described later.

In a three dimensional chaotic dynamical system, after transient motion has dissipated, an orbit usually moves in a well defined direction along with its neighbours. Consider a surface now through which the orbit is passing, with the normal direction the same as that of the flow of trajectories. Orbits intersecting this flow will usually fill a space which looks like the segment of a curve, since the attractor has zero volume. At some point in the flow there will be a branching point where the curve cannot be parametrised in one dimension, where the space is stretched apart and the curve becomes multi-valued. Using cylindrical coordinates (r, ϕ, z) with $r = \sqrt{x^2 + y^2}$ and looking at the intersection points of the flow with planes at fixed values of ϕ provides a clearer image of the structure of the attractor in figure 1.9. The first plane at ϕ_0 makes an angle $-\pi/3$ to the positive x axis, while subsequent planes are incremented by $\pi/6$, covering most of the activity in the $(+x, +y)$ quadrant visible in 1.7, until the last plane which is parrallel to the positive y direction. The curve containing the orbits elongates and folds in on itself, which is the generating mechanism of chaos in this system.

While this is a useful analogy for describing strange attractors in $\mathbb{R}^3$, the dynamical systems studied in this thesis will typically be of much higher dimension. A reduction to $\mathbb{R}^3$ must then be guaranteed before such a projection can be made, and it is idealistic to presume an analytical form of the branched mani-

fold can be found. The reductions made later in the chapter on initialisation are still of dimension greater than three, so this theory is of little practical use with regards to the primary aims of this work. However, there exist other invariant manifolds inherent within dynamical systems which are directly relevant to the initialisation problem.

1.5.7 Initialisation and the Slow Manifold

The term slow manifold was first coined by Leith in the context of numerical weather prediction[6]. Perturbing the primitive equations which describe the atmosphere generates two kinds of waves, fast gravity waves and the slowly propagating Rossby waves. Nonlinearity causes the waves to interact and force each other, so while gravity waves cannot be neglected entirely a compromise must be found between the modes so that no additional fast waves are generated. This compromise materialises as a dimensionally reduced subspace of the full phase space which captures the asymptotic behaviour of the model. An imbalanced initial condition will dissipate energy in the form of fast waves until it reaches the subspace, so a successful initialisation requires that this region, the slow manifold, be known. Unfortunately, it is not always guaranteed that such a subspace will exist in a model.

From a dynamical systems point of view, the slow manifold is effectively the attractor (in some cases the branched manifold containing the attractor), and initialisation is the art of approximating it. Consider a modified version of (1.26) where the angular coordinate is slowly evolving, then

$$\frac{dx}{dt} = x - \epsilon y - x(x^2 + y^2) \tag{1.39}$$

$$\frac{dy}{dt} = \epsilon x + y - y(x^2 + y^2). \tag{1.40}$$

so

$$\frac{dr}{dt} = r(1 - r^2) \tag{1.41}$$

$$\frac{d\theta}{dt} = \epsilon, \tag{1.42}$$

where $\epsilon \ll 1$. Introducing a slow time $\tau = \epsilon t$, the equations become

$$\epsilon\frac{dr}{d\tau} = r(1 - r^2) \tag{1.43}$$

$$\frac{d\theta}{d\tau} = 1. \tag{1.44}$$

For long times where asymptotic behaviour dominates and $\epsilon \to 0$, the left hand side of the r equation vanishes and all that remains is the circle of unit radius, which is the attractor for this system. Since the value of r is known, the system has been reduced to one dimension and it is only necessary to integrate θ with respect to time.

Suppose now the symmetry of (1.39) is broken by the addition of a vector $\tilde{\mathbf{x}} = (\epsilon x, 0)$ to the right hand side. After conversion to polar coordinate, this leaves

$$\epsilon\frac{dr}{d\tau} = r(1 + \epsilon\cos^2\theta - r^2) \tag{1.45}$$

$$\frac{d\theta}{d\tau} = 1 - 1/2\sin 2\theta, \tag{1.46}$$

one slow and one fast mode. Note that there is an epsilon on both sides of the equation, so some care must be taken in the limiting process. The asymptotic behaviour of r can be found by taking an expansion in terms of small parameter ϵ,

$$r = \sum_{i=0}^{\infty} r_i\epsilon^i. \tag{1.47}$$

Considering only the first two terms of the expansion, zeroth order in ϵ yields

the same equation as (1.43),

$$\epsilon \frac{dr_0}{dt} = r_0(1 - r_0^2) \tag{1.48}$$

with a stable fixed point at $r_0 = 1$. First order gives

$$\epsilon \frac{dr_1}{dt} = r_0 \cos^2 \theta - 3r_0^2 r_1 + r_1, \tag{1.49}$$

and letting $r_0 = 1$,

$$\epsilon \frac{dr_1}{dt} = \cos^2(\theta) - 2r_1. \tag{1.50}$$

Setting $\frac{dr_1}{dt}$ to zero gives a asymptotic solution for r in terms of θ,

$$r(\theta) = 1 + (\epsilon/2) cos^2\theta + \mathcal{O}(\epsilon^2). \tag{1.51}$$

Again, the fast equation need not be integrated as its asymptotic behaviour can now be found in terms of the slowly varying θ, via a slaving function $r(\theta)$. This radius-angle relation allows the dynamical system in R^2 to be parametrised in a periodic interval of R^1. The slaving function concept will be useful later on, and its application to higher dimensional chaotic systems will be described in greater detail in chapter 4, with the introduction of the Baer-Tribbia series and the inertial manifold.

Coupled GCM simulations for seasonal prediction are at the present stage too complex to be treated in the same way, and instead rely on observational data to keep from drifting to the wrong parts of phase space. The process of data assimilation involves regularly projecting model state vectors onto the data manifold, the space of all possible states given some measured variables. An ideal way to initialise such a system would be to project initial states onto the intersection between the data manifold and the slow manifold[57]. However, current predictions do little to separate fast and slow dynamics[58]. The ocean and atmosphere are assimilated separately which can result in the generation of

fast dynamics due initialisation shock.

The methods outlined in this thesis circumvent the problem of initialisation shock by considering the ocean-atmosphere system as a single dynamic entity. Calculating the normal modes of this system allows for a dimensionality reduction whereby only the slower dynamics are integrated. This process results in the generation of families of submodels with varying degrees of slowness which can be integrated with longer timesteps and demonstrate improvements in predictive skill on seasonal timescales. It is found that the lower dimensional parametrisation of the model attractor results in a better forecast, provided the reduced model behaviour remains loyal to that of the full model.

Initialisation aims to create a channel through which information about infinite dimensional real world dynamics can be passed on to the finite dimensional computer model, filtering out all unwanted data. The first logical step then, is to ensure the real world system and the models can be understood within the same framework.

1.5.8 Partial Differential Equations as Dynamical Systems

Predicting climate, like any fluid dynamics problem, ultimately involves solving partial differential equations (PDEs). The problem with posing PDEs such as the diffusion equation

$$\partial_t T(x,t) = \partial_{xx} T, \tag{1.52}$$

subject to some boundary condition, say

$$T(-1,t) = T(1,t) = 0 \tag{1.53}$$

as dynamical systems is that every single point in this region for example $T(-99/100, t)$, $T(1/\sqrt{2}, t)$ et cetera, adds another dimension to the phase space, and there is an uncountable infinity of points within $[-1, 1]$. It is then useful to consider a snapshot of $T(x,t)$ at each point in time and expand the function

into an infinite set of continuous basis functions

$$T(x,t) = \sum_{n=1}^{\infty} c_n(t) sin(\pi n x), \tag{1.54}$$

at least reducing the spatial dimensionality of the dynamical system from an uncountable infinity to a countable one. Taking advantage of the orthogonality of the basis functions leaves an infinite set of time-dependent coefficients which satisfy

$$\frac{dc_n}{dt} = -n^2 c_n. \tag{1.55}$$

Before solving this, it is worth noting the similarities between this equation and (1.6); it describes a dynamical system in an infinite dimensional phase space of a_n coefficients. While it is tempting to call this space $\mathbb{R}^\infty$, there is no guarantee that the Euclidean norm

$$\|\mathbf{c}\| = \sqrt{\sum_{i=1}^{\infty} c_n^2} \tag{1.56}$$

will return any meaningful answer. It is helpful at this point to introduce the concept of a Hilbert space, a generalised Euclidean space which treats functions as infinite dimensional vectors, but with the same geometric notions of lengths and angles. Considering only real functions, the familiar dot product of a vector space

$$\mathbf{f} \cdot \mathbf{g} = \sum_{i=1}^{N} f_i g_i, \tag{1.57}$$

is replaced with

$$\int_\Omega f(x,t) g(x,t) dx, \tag{1.58}$$

over some domain Ω. A time-dependent PDE is effectively a dynamical system whose state is given at each point in time by a point in a Hilbert space. While the phase space of a PDE system is infinite dimensional, it can be shown that the attractors are finite dimensional subsets of the full phase space. Furthermore, if $f(t)$ and $g(t)$ are two solutions of the PDE, there is a property which guarantees that if there is a projection from a Hilbert space to a finite dimensional space

which is determining, that is

$$|P(f(t) - g(t))| \to 0 \text{ as } t \to \infty, \tag{1.59}$$

then in the infinite space

$$|f(t) - g(t)| \to 0 \text{ as } t \to \infty. \tag{1.60}$$

This confirms the attractor of an infinite dimensional dynamical system can be contained within a finite dimensional space. However, yet to be found is some way to map from the infinite to the finite and back again. This is the key to improving predictability of complex models, and the theory of inertial manifolds, which shall be introduced in the initialisation chapter, is one possible route to bridging this gap. Many of these ideas were inspired by Robinson[82], a good introduction to the treatment of PDEs as dynamical systems. There are many well known ways in which the infinite dimension can be approximated by a low order system, typically involving functions with special properties.

1.5.9 Orthogonal Decomposition

To solve any partial differential equation numerically, it is essential to first find a way of translating from the infinite dimensional function space to a vector space of finite, preferably low, dimension with a minimal loss of information. There are several known ways of achieving this.

A vector $\mathbf{x}$ in a Hilbert space can usually be written in the form

$$\mathbf{x} = \sum_n c_n \phi_n, \tag{1.61}$$

where ϕ_n defines a set of vectors or functions which satisfy

$$\phi_n \cdot \phi_m = \delta_{n,m}, \tag{1.62}$$

with $\delta_{n,m}$ the Kronecker delta satisfying

$$\delta_{n,m} = \begin{cases} 1 & \text{if } n = m \\ 0 & \text{otherwise} \end{cases} \tag{1.63}$$

A set of basis functions which can reconstruct any vector in the space as in (1.61) is known as complete. Changing the basis of an equation is a straightforward process, for example substituting (1.61) into the general linear equation (1.7) gives

$$\sum_n \frac{dc_n}{dt}\phi_{\mathbf{n}} = A\sum_n c_n(t)\phi_n, \tag{1.64}$$

and since taking the dot product over another index ϕ_m gives a 1 if $n = m$ or 0 otherwise, the summation disappears leaving

$$\frac{dc_n}{dt} = B\sum_n c_n(t), \tag{1.65}$$

where $B = \phi_{\mathbf{m}} A \phi_{\mathbf{n}}$. For function spaces, these bases ϕ_n are usually the functions $\sin(nx)$, $\cos(nx)$, but could also be other periodic functions or special sets of polynomials. The basis functions used in this research were those of a finite difference type, which will be explained in the next section.

In the example from the end of the previous section, a solution to the temperature equation was expressed in terms of an infinite sum of $\sin(nx)$ basis functions. The coefficients satisfied

$$\frac{da_n}{dt} = -n^2 a_n. \tag{1.66}$$

Now, large values of n correspond to functions which oscillate spatially with a high frequency, and are associated with the smaller length scales. Note also that perturbations of these terms decay very rapidly with time. If the interest is in the large scale, long term behaviour it should be sufficient to compute only a small number of $a_n(t)$, and assume the small scale, rapidly decaying terms are negligible. However, this scheme often fails for nonlinear systems, where high

frequency spatial components are not so easily separated from the low frequency ones, and is the premise for slow manifold techniques discussed later.

Finite Difference Basis

Consider a function $\Theta(x)$ with $x \in [0,1]$. The idea behind finite difference will be to divide this space into N subspaces, with larger N resolving smaller scale with a better approximation to Θ. Throughout this work, the choice of basis functions will be the set

$$f_i = \begin{cases} 1/N & \text{if } (i-1)/N < x < i/N; \\ 0 & \text{otherwise.} \end{cases}, \tag{1.67}$$

where $1 \leq i \leq N$. From a climate modelling perspective, this is analogous to dividing up properties along a one dimensional region, say the depth of the Pacific thermocline along the equator, into N box averaged quantities. It is a trivial exercise to check that these functions satisfy orthonormality, that is

$$\mathbf{f_i} \cdot \mathbf{f_j} = \delta_{i,j}, \tag{1.68}$$

where $\delta_{i,j}$ is the Kronecker delta. Any function $\mathbf{\Theta}$ can be decomposed into coefficients

$$c_i = (\mathbf{f}_i \cdot \mathbf{\Theta}), \tag{1.69}$$

The usual definition of derivative,

$$\frac{df}{dx} = \lim_{\delta \to 0} \frac{f(x+\delta) - f(x)}{\delta}, \tag{1.70}$$

becomes

$$D^+\mathbf{\Theta} = (f_{i+1} - f_i)\mathbf{\Theta}, \tag{1.71}$$

for the forward difference of a point and its nearest right hand neighbour, and

$$D^-\mathbf{\Theta} = (f_i - f_{i-1})\mathbf{\Theta}, \tag{1.72}$$

for the backwards difference with the neighbour on the left hand side. It is important to point out that a basis of N functions generates a derivative set of $N-1$ functions. Every time a spatial derivative is taken, the space corresponding to one basis function is lost from the set, but this information is always regained through the introduction of boundary conditions. The details of these conditions will be covered in the next chapter where the model equations are derived.

Chapter 2

The 2-strip Model

This chapter will derive the governing equations for the ENSO models studied in the next chapter. Beginning with the fluid mechanics of the equatorial waveguide, dispersion relations are derived which lead to a 2-strip system describing thermocline motion in terms of two wave modes (one Kelvin and one Rossby). Next the evolution of the sea surface temperature (SST) anomaly, largely influenced by thermocline motion, is derived from basic temperature advection equations which have been linearised about a climatological mean state. Finally the atmospheric response to an SST anomaly is described, and this generates a wind stress anomaly which drives the thermocline.

2.1 Geophysical Fluids Background

2.1.1 Equatorial Wave Dynamics

Since the ocean is effectively a thin layer on the surface of a rotating sphere, with the average depth of the ocean being only a few kilometres compared to the radius of the earth which is on the scale of thousands of kilometres, horizontal motion dominates on length scales larger than the ocean depth. While the ocean has in reality many layers, a simple stratified ocean has two layers of density ρ_0 (top) and $\rho_0 + \Delta\rho$ (bottom), with the interface between the layers corresponding

to the thermocline. Displacements of the ocean surface in comparison with thermocline depths are negligible, so the former can be thought of as a rigid lid and only variations of the interface are considered. The reader is now referred to the appendix, where this two-layer model of the linear shallow water equations in the equatorial beta plane is derived from the rotating shallow water equations on an equatorial β-plane. Additionally, these same derivations can be found in Gill[60] or Pedlosky[59]. The end result is the set of equations

$$\frac{\partial u}{\partial t} - \beta y v = -g^{'} \frac{\partial h}{\partial x}, \tag{2.1}$$

$$\frac{\partial v}{\partial t} + \beta y u = -g^{'} \frac{\partial h}{\partial y}, \tag{2.2}$$

$$\frac{\partial h}{\partial t} + H \left(\frac{\partial u}{\partial x} + \frac{\partial v}{\partial y} \right) = 0, \tag{2.3}$$

describing the difference in zonal and meridional velocity between the two layers and the deviation h from the average depth H of the density interface. Here, the positive x-direction goes from west to east, and the positive y-direction south to north, with $y = 0$ on the equator. Atmospheric forcing will be ignored for now. Reduced gravity is defined by

$$g^{'} = \frac{\Delta \rho}{\rho_0} g, \tag{2.4}$$

with $\Delta \rho$ the difference in density between the layers, and it is helpful to define a wave speed

$$c = \sqrt{g' H}. \tag{2.5}$$

Now, on the equator the β term vanishes, leaving

$$\frac{\partial u}{\partial t} = -g^{'} \frac{\partial h}{\partial x}, \tag{2.6}$$

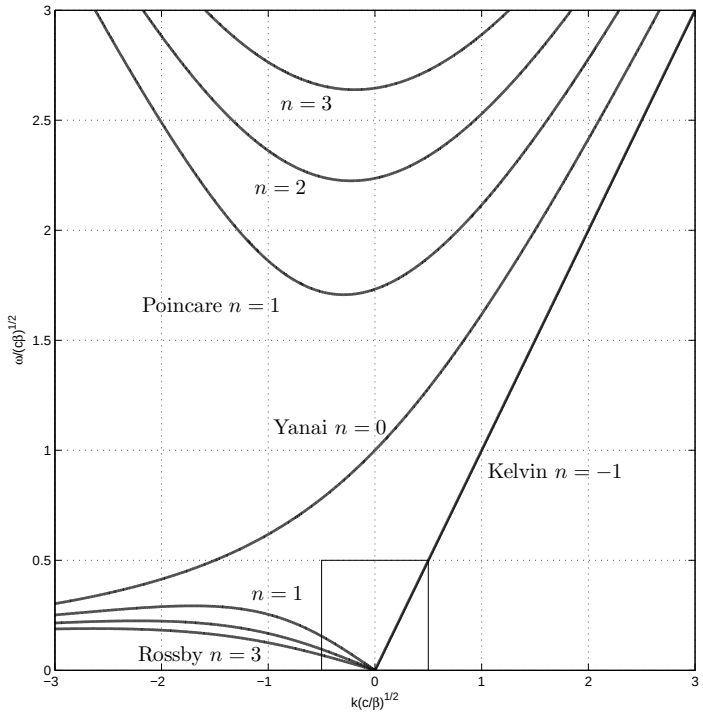

Figure 2.1: Dispersion relation of equatorial waves in the (Ω, K) plane.

The equation for the conservation of potential vorticity

$$\zeta = \frac{\partial v}{\partial x} - \frac{\partial u}{\partial y} \tag{2.7}$$

of this system is

$$\frac{\partial}{\partial t}\left(\zeta - \beta y \frac{h}{H}\right) + \beta v = 0. \tag{2.8}$$

Operating on (2.1) and (2.3) with $-(\beta y/c^2)\partial_t$, (2.2) with ∂_t^2/c^2, (2.8) with $-\partial_x$, and taking the sum yields

$$\frac{\partial}{\partial t}\left[\frac{1}{c^2}\left(\frac{\partial^2 v}{\partial t^2} + \beta^2 y^2\right) - \left(\frac{\partial^2 v}{\partial x^2} + \frac{\partial^2 v}{\partial y^2}\right)\right] - \beta \frac{\partial v}{\partial x} = 0. \tag{2.9}$$

Looking for solutions of the form $v = \hat{v}(y)e^{i(kx-\omega t)}$ gives

$$\frac{d^2v}{dy^2} + \left(\frac{\omega^2}{c^2} - k^2 - \frac{\beta k}{\omega} - \frac{\beta^2 y^2}{c^2}\right) v = 0. \tag{2.10}$$

When subjected to the boundary conditions $v \to 0$ as $y \to \pm\infty$, a solution to the above equation is

$$v = D_n(Y)\cos(kx - \omega t), \tag{2.11}$$

where D_n are parabolic cylinder functions for integer n and

$$Y = \sqrt{2\frac{\beta}{c}}y. \tag{2.12}$$

Now (2.10) can be rearranged and written in the form of an eigenvalue equation

$$\left(2\frac{d^2}{dY^2} - \frac{Y^2}{2}\right) v = Ev, \tag{2.13}$$

where

$$E = \beta c\left(\frac{\omega^2}{(\beta c)^2} - \frac{k^2}{\beta^2} - \frac{k}{\beta\omega}\right). \tag{2.14}$$

At this stage it is useful to define the ladder operators

$$L_\pm = \frac{d}{dY} \mp \frac{Y}{2}, \tag{2.15}$$

which have the properties

$$L_+D_n = -D_{n+1} \quad L_-D_n = nD_{n-1}. \tag{2.16}$$

Since

$$\left(2\frac{d^2}{dY^2} - \frac{Y^2}{2}\right) v = \left(L_+L_- + L_-L_+\right) v, \tag{2.17}$$

using properties of the ladder operators the left hand side reads

$$\frac{1}{2}(L_+L_- + L_-L_+)v = -(2n+1) \tag{2.18}$$

leading to the dispersion relation

$$\frac{\omega^2}{(\beta c)^2} - \frac{k^2}{\beta^2} - \frac{k}{\beta\omega} = (2n+1)\frac{1}{\beta c}. \tag{2.19}$$

Temporarily rescaling coordinates $\Omega = \omega/\sqrt{(c\beta)}$, $K = k\sqrt{c/\beta}$ provides a neater form of the above

$$\Omega^2 - K^2 - \frac{K}{\Omega} = (2n+1) \tag{2.20}$$

for $n = 0, 1, 2\ldots$ etc. If $n = -1$, this equation has a trivial solution

$$\Omega = K, \tag{2.21}$$

or

$$\omega = ck \tag{2.22}$$

which is a special case corresponding to the equatorial Kelvin wave. The case $n = 0$ corresponds to a mixed Rossby-Kelvin wave, or Yanai wave. Every integer $n > 0$ corresponds to both a Rossby and Poincaré mode, as shown in the dispersion relation figure 2.1. Because the relevant physics here is on the large scale and slow timescale, the low frequency, low wavenumber limit is taken as depicted in 2.1 by the region within the box centered around $(\Omega, K) = 0$. By operating on 2.1 with $\frac{\partial}{\partial t}$ leaving

$$\frac{\partial v}{\partial t} = \frac{1}{\beta y}\left(\frac{\partial^2 u}{\partial t^2} + g^{'}\frac{\partial^2 h}{\partial t \partial x}\right), \tag{2.23}$$

and substituting $h = \hat{h}(y)e^{i(kx-\omega t)}$, $u = \hat{u}(y)e^{i(kx-\omega t)}$, the right hand side becomes

$$\frac{1}{\beta y}\left(k\omega g^{'}\hat{h} - \omega^2\hat{u}\right) \to 0, \tag{2.24}$$

tending to zero in the low frequency/wavenumber limit. This way, acceleration in the meridional direction can be neglected and equations (2.1), (2.2) and (2.3)

reduce to

$$\frac{\partial u}{\partial t} - \beta y v = -g^{'} \frac{\partial h}{\partial x}, \tag{2.25}$$

$$\beta y u = -g^{'} \frac{\partial h}{\partial y}, \tag{2.26}$$

$$\frac{\partial h}{\partial t} + H \left(\frac{\partial u}{\partial x} + \frac{\partial v}{\partial y} \right) = 0. \tag{2.27}$$

2.1.2 Kelvin Mode

On the equator, $y = 0$, and (2.25) and (2.27) can be written in terms of h alone in the form of the wave equation in the x direction

$$\left(\frac{\partial^2}{\partial t^2} + c^2 \frac{\partial^2}{\partial x^2} \right) h = 0. \tag{2.28}$$

The above equation can be solved exactly using the D'Alembert solution for h

$$h(t) = h_+(x + ct, y) + h_-(x - ct, y), \tag{2.29}$$

implying from (2.27)

$$Hu(t) = -c \left[h_+(x + ct, y) - h_-(x - ct, y) \right]. \tag{2.30}$$

with h_+ and h_- unknown functions. Substituting in the trial solutions for westward h_+ and eastward h_- propagating waves individually into (2.26) results in the expressions

$$h_+ y = a^2 \tfrac{\partial h_+}{\partial y} \quad h_- y = -a^2 \tfrac{\partial h_-}{\partial y}, \tag{2.31}$$

where $a^2 = \frac{c}{\beta}$. The constant a is known as the equatorial radius of deformation, to be explained shortly. Assuming a separable solution such that

$$h_-(x - ct, y) = Y_-(y) X_-(x - ct) \quad h_+(x + ct, y) = Y_+(y) X_+(x + ct), \tag{2.32}$$

leads to

$$\left(y - a^2 \tfrac{d}{dy}\right) Y_+ = 0 \quad \left(y + a^2 \tfrac{d}{dy}\right) Y_- = 0, \tag{2.33}$$

with solutions

$$Y_\pm = e^{\pm \frac{y^2}{2a^2}}. \tag{2.34}$$

Solutions which decay as $y \to \pm\infty$ are therefore guaranteed by choosing $h_+ = 0$. So the waves are uni-directional and non-dispersive with relation

$$\omega = ck, \tag{2.35}$$

with an amplitude which decays off the equator, and the equatorial Kelvin wave has been rederived along with its meridional structure.

2.1.3 Rossby Mode

In the low frequency, low wavenumber limit nonlinear terms ω^2 and k^2 can be neglected from (2.20), leaving

$$\omega = \frac{-ck}{(2n+1)}, \tag{2.36}$$

corresponding to an infinite family of westward propagating Rossby waves. Now, considering only the first few ($n = 1, 2$ and 3), their parabolic cylinder functions are

$$D_1(Y) = Y e^{-Y^2/4} \tag{2.37}$$

$$D_2(Y) = \left(Y^2 - 1\right) e^{-Y^2/4} \tag{2.38}$$

$$D_3(Y) = \left(Y^3 - 3Y\right) e^{-Y^2/4}. \tag{2.39}$$

Since the atmospheric forcings involved are largely symmetric about the equator, Rossby waves which have contributions to u and h which are symmetric about the equator are the most relevant, the dominant being D_1 with phase speed

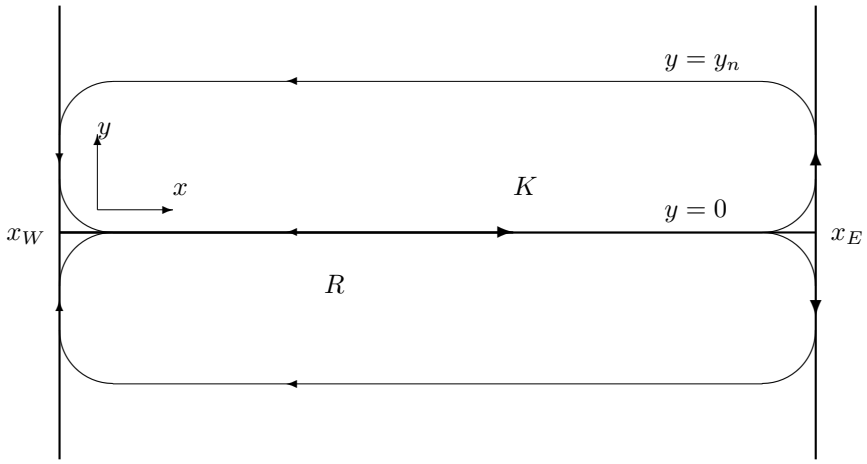

Figure 2.2: Diagram depicting Rossby and Kelvin mode interactions in the equatorial strip, with the Kelvin mode K changing identity into a Rossby R mode at the eastern boundary $x = x_E$, and the Rossby mode becoming a Kelvin mode at the western boundary $x = x_W$.

$-c/3$, the next in line D_3 with phase speed $-c/7$. There are then two distinct classes of wave mode, one Kelvin mode which for which h peaks on the equator and moves east, and a family of Rossby modes which have peaks off the equator and propagates slowly to the west. The distinct structural imprint of Kelvin and Rossby modes on the equatorial thermocline depth make it a convenient quantity to model in this context, as the evolution equations describing its dynamics have a relatively simple form.

2.2 The 2-strip System

2.2.1 Main Equations

Thermocline wave modes play an important role in ENSO dynamics, in both the growth and termination of events. Of major importance are the eastward travelling Kelvin mode, which propagates along the equator, and the westward travelling Rossby modes, which propagate in both the equatorial region and the off-equatorial regions to the north and south. When the Kelvin (Rossby) mode reaches the eastern (western) boundary, it is reflected imperfectly as a Rossby

(Kelvin) wave. Translation of waves induces a motion of the thermocline which changes the sea surface temperature, effectively building or breaking up a temperature anomaly. In the 2-strip system[15], the shape of the thermocline can be expressed entirely in terms of these modes which vary zonally while their meridional structure is fixed in time, with symmetry about the equator. Derivation of the equations is largely the same as the original work by Jin, but a new dimensionless parameter μ is introduced for purposes which will be explained shortly. In the models which are to be derived, an overwhelming proportion of phase space is attributed to the state of the thermocline depth, so their importance cannot be understated. After taking the low frequency/wavenumber limit of equations (2.1), (2.2) and (2.3), a zonal wind stress τ_x is applied over the upper layer and for the sake of stability a weak damping term ϵ is included to give

$$\left(\frac{\partial}{\partial t}+\epsilon\right)u-\beta yv+g^{'}\frac{\partial}{\partial x}h=\frac{\tau_x}{\rho H}, \tag{2.40}$$

$$\beta yu+g^{'}\frac{\partial h}{\partial y}=0, \tag{2.41}$$

$$\left(\frac{\partial}{\partial t}+\epsilon\right)h+H\left(\frac{\partial}{\partial x}u+\frac{\partial}{\partial y}v\right)=0. \tag{2.42}$$

After some algebra, an equation in terms of h alone is

$$\left(\frac{\partial}{\partial t}+\epsilon\right)\left[h-\frac{\partial}{\partial y}\left(\frac{a^4}{y^2}\frac{\partial h}{\partial y}\right)\right]-c\frac{a^2}{y^2}\frac{\partial h}{\partial x}=\frac{\partial}{\partial y}\left(\frac{a^2}{y}\frac{\tau_x}{c\rho}\right), \tag{2.43}$$

where again the equatorial radius of deformation $a=\sqrt{c/\beta}$ and Kelvin wave speed $c=\sqrt{g^{'}H}$. In the equatorial strip, a slightly different form to Jin

$$h(x,y,t)=h_e(x,t)+(1-e^{-\frac{y^2}{2a^2}})\Delta h(x,t) \tag{2.44}$$

is assumed, where $\Delta h=\mu h_n-h_e$. The parameter μ controls the partitioning of the response to wind stress forcing between Kelvin and Rossby waves, but for most cases will be set to unity, making the response the same as Jin. Leaving μ unconstrained leads to a more general, and potentially more realistic system.

Substituting into (2.43), carrying out the derivatives and multiplying through by $(y/a)^2$ leaves

$$\left(\frac{\partial}{\partial t}+\epsilon\right)\left[(y/a)^2(h+2\Delta h)+\Delta h\right]-c\frac{\partial h}{\partial x}=\frac{1}{c\rho}\left(y\frac{\partial}{\partial y}\tau_x-\tau_x\right). \tag{2.45}$$

On the equator, $y=0$, this reduces to

$$-\left(\frac{\partial}{\partial t}+\epsilon\right)\Delta h+c\frac{\partial h_e}{\partial x}=\frac{\tau_x}{c\rho}, \tag{2.46}$$

Zonal velocity at the equator, which shall come in useful later on, is

$$u=-\frac{c}{H}\frac{a^2}{y}\frac{\partial h}{\partial y}, \tag{2.47}$$

becoming

$$u|_{y=0}=-\frac{c}{H}\Delta h \tag{2.48}$$

when evaluated at the equator. Substituting into the expression (2.46) for the wind forced equatorial thermocline yields an evolution equation for u_e,

$$\left(\frac{\partial}{\partial t}+\epsilon\right)u|_{y=0}+\frac{c^2}{H}\frac{\partial h_e}{\partial x}=\frac{\tau_x}{\rho H}. \tag{2.49}$$

As y is increased to a finite value the nature of the equations changes as the equatorial Kelvin mode decays. For some finite value y_n off the equator, thermocline displacement is observed to reach an extremum and

$$h\gg\frac{\partial}{\partial y}\left(\frac{a^4}{y_n^2}\frac{\partial h}{\partial y}\right). \tag{2.50}$$

Equation (2.43) then becomes

$$\left(\frac{\partial}{\partial t}+\epsilon\right)h_n-c\frac{a^2}{y_n^2}\frac{\partial h_n}{\partial x}=\frac{\partial}{\partial y}\left(\frac{a^2}{y_n}\frac{\tau_x}{\mu c\rho}\right), \tag{2.51}$$

describing a single Rossby mode of the equation, which propagates westward. This is representative of the effect a group of Rossby waves has on the off-equatorial strip at $y = y_n$. The governing equations are thus

$$\left(\frac{\partial}{\partial t} + \epsilon\right)(h_e - \mu h_n) + c_K \frac{\partial h_e}{\partial x} = F_e(x,t) \tag{2.52}$$

at the equatorial strip $y = 0$, where $c_K = c$ and $F_e = \tau_x / c\rho$ and

$$\left(\frac{\partial}{\partial t} + \epsilon\right) h_n + c_R \frac{\partial h_n}{\partial x} = F_n(x,t) \tag{2.53}$$

at the northern strip $y = y_n$, with $c_R = -c(a/y_n)^2$ and

$$F_n = \frac{\partial}{\partial y}\left(\frac{a^2}{y}\frac{\tau_x}{\mu c \rho}\right)\Bigg|_{y=y_n}, \tag{2.54}$$

where

$$x \in [-L, L] \quad t \in \mathbb{R}^+. \tag{2.55}$$

Northern strip y_n is located at the extrema of the function which is a combination of the first two modes which are symmetric in u and h, i.e. D_1 and D_3. These modes have wave speeds $-c_K/3$ and $-c_K/7$ respectively, and the value of c_R used is the average of these

$$c_R = -\frac{c_K}{2}\left(\frac{1}{3} + \frac{1}{7}\right) \approx -c_K/4, \tag{2.56}$$

so $y_n = 2a$. Equations (2.52) and (2.54) are subject to the reflective boundary conditions

$$h_n(L,t) = R_E h_e(L,t) \quad h_e(-L,t) = R_W h_n(-L,t) \tag{2.57}$$

at the western ($x_W = -L$) and eastern ($x_E = +L$) boundaries. This is shown graphically in image 2.2. Although the full model will eventually be coupled, with the forcing terms dependent on the thermocline variables, there is still

something to be said about the uncoupled system with idealised forcing. While h_n is affected only by Rossby modes, h_e has contributions from both Kelvin and Rossby modes. It should be possible to write equations (2.52) and (2.54) in terms of Kelvin and Rossby modes alone, or as quantities which move at their respective velocities. If it is assumed that $\epsilon = 0$, the 2-strip equations can be written in matrix-vector form

$$\gamma \partial_t \mathbf{h} + C \partial_x \mathbf{h} = \mathbf{F}, \tag{2.58}$$

with $\mathbf{F} = (F_e, F_n)^T$, $\mathbf{h} = (h_e, h_n)^T$, and γ, C the matrices

$$\gamma = \begin{pmatrix} 1 & -1 \\ 0 & 1 \end{pmatrix}, \quad C = \begin{pmatrix} c_K & 0 \\ 0 & c_R \end{pmatrix}. \tag{2.59}$$

Multiplying through on the left by the inverse of γ, the equation becomes

$$\partial_t \mathbf{h} + \tilde{C} \partial_x \mathbf{h} = \tilde{\mathbf{F}} \tag{2.60}$$

where a tilde implies left multiplication of γ^{-1}. The problem is now to find the left eigenvalues and eigenvectors of the matrix $\tilde{C}$. The eigenvalues are the wave speeds and taking the dot product of the associated eigenvectors with the vectors h and $\tilde{F}$ will return the quantity which moves at that wave speed and the forcing required to excite a pure mode. $\tilde{C}$ has eigenvalues

$$\lambda_1 = c_K, \quad \lambda_2 = c_R \tag{2.61}$$

and normalised eigenvectors

$$\mathbf{v}_1 = \begin{pmatrix} 1 \\ 0 \end{pmatrix}, \quad \mathbf{v}_2 = N \begin{pmatrix} 1 \\ \frac{c_R - c_K}{c_R} \end{pmatrix}, \quad N = \frac{1}{\sqrt{1 + (1 - c_K/c_R)^2}}. \tag{2.62}$$

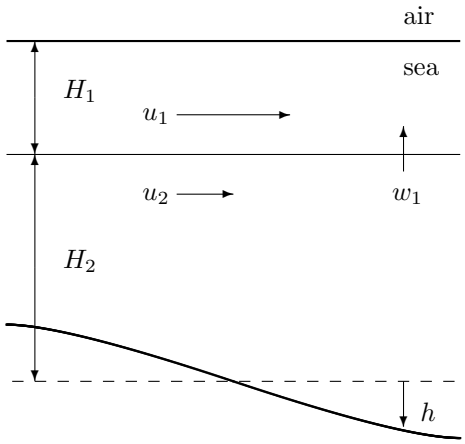

Figure 2.3: Diagram depicting the wind driven surface layer of depth H_1, mean thermocline depth H_1+H_2 and thermocline depth anomaly h, along with surface current u_1 and subsurface current u_2.

The linear combinations and their associated forcings are thus

$$\begin{aligned} h_1 = N(h_e + \tfrac{c_R - c_K}{c_R} h_n) \quad & F_1 = N(F_e - \tfrac{c_R - c_K}{c_R} F_n) \\ h_2 = h_n \quad & F_2 = F_n. \end{aligned} \tag{2.63}$$

This way, any thermocline profile (h_e, h_n) can be decomposed into separate Kelvin and Rossby components. Thus, while a Kelvin mode is contributes only to h_e, a Rossby mode influences both h_e and h_n.

2.2.2 Wind Forcing

Atmospheric motion affects the thermocline by raising or lowering the sea surface over large scales, inducing a pressure difference which draws the interface closer or pushes it further away from the surface. The shear layer can be regarded as a turbulent surface layer of constant depth, which induces upwelling or downwelling currents within the mixed layer. Dissipation of energy of the system is strongly affected by the inclusion of this layer, making the terms which

follow a necessary component of the coupled model. Similar derivations can be found in Jin and Neelin[62] or Zebiak and Cane[11]. First, the upper ocean layer is partitioned into a surface layer of constant depth H_1 and subsurface layer of constant depth H_2, such that the entire upper layer depth is

$$H = H_1 + H_2. \tag{2.64}$$

If the upper layer velocities (u, v) derived earlier are taken to represent the depth average of the surface and subsurface layers, the average velocity of the surface layer is

$$u_1 = u + u_s, \quad v_1 = v + v_s, \tag{2.65}$$

while the average of the whole upper layer is

$$(u, v) = \frac{H_1(u_1, v_1) + H_2(u_2, v_2)}{H} \tag{2.66}$$

making the shear current

$$(u_s, v_s) = [(u_1, v_1) - (u_2, v_2)]\,(H_2/H). \tag{2.67}$$

Starting with the zonal momentum equations in the surface and subsurface layers,

$$\left(\frac{\partial}{\partial t} + \epsilon\right) u_1 - \beta y v_1 + \epsilon_s u_s = \frac{\tau_x}{\rho H_1} \tag{2.68}$$

and

$$\left(\frac{\partial}{\partial t} + \epsilon\right) u_2 - \beta y v_2 - \frac{H_1}{H_2}\epsilon_s u_s = -g^{'}\frac{\partial h}{\partial x}, \tag{2.69}$$

where ϵ_s is a damping coefficient of around $1/2$ days^{-1}. With this information, momentum difference

$$(u_1, v_1) - (u_2, v_2) = \frac{\tau_x}{\rho H_1}\frac{(\epsilon_s, \beta y)}{\epsilon_s^2 + (\beta y)^2} \tag{2.70}$$

can be calculated[62][11], where ϵ_s is a strong surface damping rate. Contributions to SST typically come from upwelling, which at the base of the surface layer is

$$w_1 = H_1 \left(\frac{\partial}{\partial x} u_1 + \frac{\partial}{\partial y} v_1 \right), \tag{2.71}$$

and evaluated at the equator this amounts to

$$w_s = H_2 \frac{(\epsilon_s \partial_x \tau_x - \beta \tau_x)}{\epsilon_s^2 \rho H}. \tag{2.72}$$

Typically the β term dominates, leaving at H_1

$$w_s \simeq -H_2 \frac{\beta \tau_x}{\epsilon_s^2 \rho H}. \tag{2.73}$$

On the equator, the currents are then

$$u_1|_{y=0} = \frac{c_K}{H}(h_e - \mu h_n) + \frac{H_2}{\epsilon_s H_1} \frac{\tau_x}{\rho H}, \tag{2.74}$$

$$w_1|_{y=0} = -\frac{H_1}{H} \left(\frac{\partial}{\partial t} + \epsilon \right) h_e - \frac{\beta H_2}{\epsilon_s^2} \frac{\tau_x}{\rho H}. \tag{2.75}$$

Figure 2.3 depicts a zonal cross section of the equatorial Pacific basin identifying the different layers.

2.2.3 SST Dynamics

An equation parametrising the time evolution of SST anomalies is now derived. This information is essential for determining wind stress anomalies, as the atmosphere itself is driven largely by the thermal energy which it draws from the ocean. Thermodynamical considerations also introduce the first nonlinearities which curb the instability of Bjerknes feedback, the process by which changes in the SST induce a pressure difference which affects the strength of atmospheric forcing, leading to further changes in SST. The main region where the SST influences wind motions which drive the thermocline is the eastern half of the Pacific basin at the equator. Here the time evolution of the equatorial SST is

given by a modified scalar advection equation,

$$\partial_t T + (\mathbf{u} \cdot \nabla)T = -\epsilon_T (T - \overline{T}), \tag{2.76}$$

where $\mathbf{u} = (u, v, R(w))$. The sea surface tends to equilibrium temperature $\overline{T}$ over a timescale $1/\epsilon_T$, parametrising various surface physics effects, while being subjected to variability through the interior flows of the ocean. Vertical velocity is here the argument of the ramp function,

$$R(x) = \begin{cases} x & x < 0; \\ 0 & x \geq 0. \end{cases}, \tag{2.77}$$

since the SST is unaffected by downwelling. If $T = T_e + T_C$ and $\mathbf{u} = \mathbf{u_e} + \mathbf{u_C}$, where terms with subscript e are small perturbations from a climatological mean state with subscript C. this can be linearised to

$$\frac{\partial}{\partial t} T_e + \mathbf{u}_e \cdot \nabla T_C + \mathbf{u}_C \cdot \nabla T_e = \epsilon_T T_e. \tag{2.78}$$

It is assumed (see Battisti and Hirst[13]) that the term $v_C \frac{\partial}{\partial y} T_e$ is small enough to be neglected. Climatological ocean currents tend to have a positive feedback effect on the temperature, so

$$\left(u_C \frac{\partial}{\partial x} + v_C \frac{\partial}{\partial y} \right) T_e = -K T_e, \tag{2.79}$$

for constant K. The surface velocities, including currents induced by wind shear, are

$$u_e = \frac{H_2}{\epsilon_s H_1} \frac{\tau_x}{\rho H} + \frac{c_K}{H} (h_e - \mu h_n), \tag{2.80}$$

$$w_e = -\frac{\beta H_2}{\epsilon_s^2} \frac{\tau_x}{\rho H} - \frac{H_1}{H} \left(\frac{\partial}{\partial t} h_e + \epsilon h_e \right). \tag{2.81}$$

Arguably the most important term in the temperature equation is $\frac{\partial}{\partial z} T_e$, as it contains a nonlinearity which comes from the stratification of the ocean. Taking

one point at the surface, where the temperature is just T_e, and a reference point in the subsurface layer $z = -H_B$,

$$\frac{\partial}{\partial z} T_e = \frac{T_e - T_B}{H_B}. \tag{2.82}$$

The temperature anomaly at the base of the layer T_B depends on the depth of the thermocline layer h_e, and a mathematically convenient approximation (based on observational data[13]) is

$$T_B = T_0 \tanh(h_e / H^*), \tag{2.83}$$

where T_0 and H_B are coefficients representative of the temperature difference above and below the layer, and the lengthscale over which this temperature difference occurs. This way, extreme thermocline anomalies at the equator do not result in rapid changes in SST due to the small range of the function T_B, which acts to limit the thermal response to h_e. Overall, the evolution is

$$\frac{\partial T_e}{\partial t} = \alpha T_e - u_e \frac{\partial T_C}{\partial x} - w_e \frac{\partial T_C}{\partial z} + \frac{w_c}{H_B} T_0 \tanh\left(\frac{h_e}{H^*}\right) \tag{2.84}$$

where $\alpha = K + \epsilon_T - w_C / H_B$. Similar derivations can be found in Cane Zebiak[11] or Battisti Hirst [4], and the physical constants used for this model are listed at the end of the chapter.

2.2.4 Atmospheric Coupling

In the coupled 2-strip model, temperature anomalies arising through thermocline motion drive an atmospheric response which feeds back into the model as wind stress, based on a Gill atmosphere[61]. For this study, the atmosphere is parametrised by nonlocal cause and effect, whereby a zonal wind stress anomaly is linearly coupled to an SST anomaly a fixed distance x_c to the east. The merid-

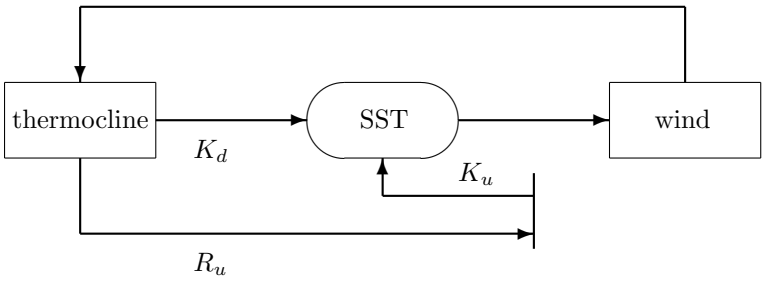

Figure 2.4: Schematic of interactions in the tropical pacific. A positive SST anomaly induces an atmospheric wind stress anomaly triggering a downwelling Kelvin wave K_d, and upwelling Rossby R_u mode. The upwelling Rossby mode is reflected in the western boundary into an upwelling Kelvin mode K_u, which ultimately ends the El Niño event and starts a La Niña.

ional profile of this wind stress anomaly is roughly Gaussian, so the form

$$\tau_x(x,y,t) = \kappa(t)T_e(x+x_c)f(x)e^{-\frac{1}{2}(\frac{y}{b})^2} \tag{2.85}$$

is used, where κ is a coupling strength and b is a lengthscale related to the atmospheric Rossby radius of deformation[62]. The meridional structure of the atmospheric response is equivalent to that of the ocean, with one Kelvin and one Rossby mode, but the radius of deformation b is larger due to the faster wave speeds. Now, the oceanic Kelvin wave is forced directly by wind stress, so

$$F_e(x,t) = \kappa T_e(x+x_c,t), \tag{2.86}$$

while the equatorial Rossby is forced by the curl of the wind stress $\frac{\partial}{\partial y}(\tau_x/y)|_{y=y_n}$, then

$$F_n(x,t) = r_f F_e(x,t) \tag{2.87}$$

where

$$r_f = -\left(\frac{2y_n^2+b^2}{\mu y_n^2 b^2}\right). \tag{2.88}$$

Sign is important here as when a positive SST anomaly T_e generates a downwelling wave in h_e, it generates an upwelling wave in h_n at the same time which,

after a delay due to wave propagation time, will reflect into h_e as an upwelling Kelvin wave and oppose the anomaly. This is shown in the schematic diagram 2.4 which summarises the various feedbacks involved in the growth and decay of an ENSO event. Zonal structure of the wind stress anomaly is given by the function $f(x)$ which for all purposes here is represented by a central block,

$$f(x) = \begin{cases} 1 & \text{if } |x| < L/3; \\ 0 & \text{otherwise.} \end{cases} \tag{2.89}$$

Throughout the modelling process there will be several further parametrisations of atmospheric motion, mostly exploring different SST box averages. It is important to note the time dependence of the coupling coefficient $\kappa(t)$. While this number ideally varies both stochastically and periodically due to the effects of turbulence and the annual cycle respectively, this study will focus on the latter such that

$$\kappa(t + \tau_a) = \kappa(t), \tag{2.90}$$

where τ_a is a timescale of one year. Ignoring random variations in coupling and considering only mean values allows for a complete description of the model within the theory of autonomous dynamical systems, and the shape of the attractor is fixed in time. Had stochastic effects been included, nonautonomous systems of the form

$$\frac{d\mathbf{x}}{dt} = \mathbf{f}(\mathbf{x}, t), \tag{2.91}$$

would constantly be nudged around and so could never settle down onto an attractor in the traditional sense, and the concept of a pullback attractor is required. The pullback attractor at time t is given by a probability distribution function built from orbits which flow onto it from a point s in the past, and ideally taking the limit $s \to \infty$[63]. Now, to avoid couplings of the form (2.90) resulting in a system of the form (2.91), some trickery is required. An increase

in phase space by dimension 2 allows for the subsystem

$$x_1 = -\omega_a x_2 \quad x_2 = \omega_a x_1, \tag{2.92}$$

where the value of ω_a is chosen such that a point in the (x_1, x_2) plane takes one year to return to its initial position, that is $\omega_a = 2\pi/\tau_a$. The simple harmonic motion of this subsystem models the sinusoidal oscillations of the annual cycle without introducing time-varying coefficients. Initial values are chosen such that

$$x_1(t_0)^2 + x_2(t_0)^2 = 1, \tag{2.93}$$

so orbits in this plane are constrained to a circle of unit radius for all time. Seasonal variability of the atmosphere is relevant in the study of ENSO since phase locking to the annual cycle is a key property of any simulation of the phenomenon. Coupling parameter κ takes the form

$$\kappa(t) = \kappa_0 + \kappa_a x_1 \tag{2.94}$$

where κ_0, κ_a are positive constants. Through an increase of dimensionality, a coupled ocean-atmosphere model forced by the seasonal cycle is described by an autonomous dynamical system, with an additional quadratic nonlinear term. Coupling amplitude is controlled by κ_a and a larger amplitude is likely to result in stronger nonlinearity. At this stage there are no further mechanisms to consider or derivations to be made, so the process of truncating and parametrising the system equations will begin in the next chapter.

2.2.5 Physical Constants

Symbol = Value (Units)	Meaning
$\rho = 1000\,\mathrm{kg/m^3}$	density of water
$\Delta\rho = 0.003\,\mathrm{kg/m^3}$	density difference between mixed layer and deep ocean
$g = 9.8\,\mathrm{m/s^2}$	acceleration due to gravity
$g^{'} = g\frac{\Delta\rho}{\rho}$	reduced acceleration due to gravity
$\frac{\partial}{\partial z}T_C = 0.04\,\mathrm{m^{\circ}Cm^{-}1}$	mean vertical temperature gradient
$\frac{\partial}{\partial x}T_C = -10^{-6}\,\mathrm{m^{\circ}Cm^{-}1}$	mean horizontal temperature gradient
$T_0 = 5\,^{\circ}\mathrm{C}$	maximum temperature of upwelled water
$H_1 = 50\,\mathrm{m}$	shear layer depth
$H_2 = 100\,\mathrm{m}$	shear to thermocline depth
$H = 150\,\mathrm{m}$	mean upper layer depth
$H^* = 40\,\mathrm{m}$	thermocline variability scale
$H_B = 75\,\mathrm{m}$	upwelling depth scale
$c_K = \sqrt{gH} = 2.1\,\mathrm{ms^{-1}}$	Kelvin wave speed
$a = 2 \times 10^5\,\mathrm{m}$	equatorial Rossby radius
$2L = 1.5 \times 10^7\,\mathrm{m}$	width of Pacific basin
$\epsilon = 5 \times 10^{-9}\,\mathrm{s^{-1}}$	ocean adjustment damping
$\epsilon_s = 5.8 \times 10^{-6}\,\mathrm{s^{-1}}$	Upper layer timescale
$\beta = 2.3 \times 10^{-11}\,\mathrm{s^{-1}m^{-}1}$	Beta parameter

Chapter 3

Box Models

This chapter will cover all of the models covered in this thesis, derived as discretisations of the 2-strip system. Beginning with the 2-box, a recharge oscillator type model with limit cycle solutions, the focus later shifts to more complex models with chaotic solutions and larger phase spaces, such as the 10-box, culimating in the n-box and n^*-box PDE models (using coarse and fine atmospheric parameterisations respectively), with the ability to resolve the spatial structure of thermocline anomalies with arbitrary precision.

3.1 The 2-box model

The 2-strip equations are first reduced to a system of ordinary differential equations through a primitive discretisation process. A similar approach to the discretisation of the 2-strip model has been carried out already by Jin for the well-known recharge oscillator model[14]. The equatorial and northern strips (marked with subscripts e and n respectively) are each divided into western and eastern halves (subscripts W and E, see figure 3.1), and the thermocline depth in each quadrant is represented by a single coordinate. The upstream Euler method defines the difference across each strip. This way, in the equatorial

Figure 3.1: East/west box average discretisation of the 2-strip model with the northern strip on top and equatorial strip on the bottom.

strip the zonal gradient term becomes

$$\frac{\partial}{\partial x} h_e = \frac{h_{eE} - h_{eW}}{L}, \tag{3.1}$$

while in the northern strip

$$\frac{\partial}{\partial x} h_n = \frac{h_{nE} - h_{nW}}{L}, \tag{3.2}$$

Implementing the boundary conditions

$$h_{eW} = R_W h_{nW} \quad h_{nE} = R_E h_{eE}, \tag{3.3}$$

reduces the model to three coordinates; the two thermocline depths h_{eE} and h_{nW}, and the average eastern equatorial SST anomaly T_{eE} from which the forcing terms are determined. Primitive atmospheric parametrisation is used whereby the wind stress is proportional to the box averaged eastern equatorial SST

$$\tau_x = \kappa T_{eE}, \tag{3.4}$$

for some constant (annual averaged) value κ. This linear relationship is approximately true for monthly mean values, as seen in GCMs and observation[67].

A further reduction is made by assuming the equatorial strip is in Sverdrup balance, that is the zonal momentum has reached a steady state determined by the temperature gradient, and (2.49) becomes

$$(c_K^2/H)\frac{h_{eE} - h_{eW}}{L} = \frac{\kappa T_{eE}}{\rho H}, \tag{3.5}$$

that is

$$h_{eE} = R_W h_{nW} + (LH/c_K^2)\frac{\kappa T_{eE}}{\rho H}. \tag{3.6}$$

Again this is only true for long timescales, as Sverdrup balance is reached over several months. Now there are only two free variables, east equatorial SST T_{eE} and west thermocline depth of the northern strip h_{nW}. Time evolution of h_{nW} is

$$\frac{dh_{nW}}{dt} = -\epsilon h_{nW} - (R_E h_{eE} - h_{nW})\frac{c_R}{L} + r_f \frac{\kappa T_{eE}}{\rho H}, \tag{3.7}$$

while that of T_{eE}, as derived from (2.84) is

$$\frac{dT_{eE}}{dt} = \alpha T_{eE} - u_{eE}\frac{\partial}{\partial x}T_C - w_{eE}\frac{\partial T_C}{\partial z} + \frac{w_c}{H_B}T_0 \tanh(\frac{h_{eE}}{H^*}), \tag{3.8}$$

where

$$u_{eE} = (H_2/\epsilon_s H_1)\frac{\kappa T_{eE}}{\rho H} + \frac{c_K}{H}(1 - \mu R_E)h_{eE}, \tag{3.9}$$

$$w_{eE} = -(\beta H_2/\epsilon_s^2)\frac{\kappa T_{eE}}{\rho H} - (H_1/H)\left(\frac{d}{dt} + \epsilon\right)h_{eE}, \tag{3.10}$$

and the expression for h_{eE} in terms of h_{nW} and T_{eE} is given above. The full system can then be written in the form

$$\frac{dh}{dt} = -a_1 h - a_2 T, \tag{3.11}$$

for the northwest thermocline depth anomaly and

$$\frac{dT}{dt} = b_1 T + b_2 h + b_3 \tanh[b_4 h + b_5 T] \tag{3.12}$$

for the east equatorial temperature anomaly, where $h = h_{nW}$ and $T = T_{eE}$. Locator subscripts have been dropped for the duration of the discussion of the 2-box model. Coefficients for the thermocline depth evolution equation are

$$a_1 = (R_E R_W - 1)\frac{c_R}{L} + \epsilon, \tag{3.13}$$

$$a_2 = c_R(R_E - 1)(H/c_K^2)\frac{\kappa}{\rho H}. \tag{3.14}$$

Calculation of thermodynamic evolution coefficients is somewhat more demanding, with

$$b_0 = 1 - \frac{\partial T_C}{\partial z}\frac{\kappa}{\rho H}(LH_1/c_K^2), \tag{3.15}$$

$$b_1 = \frac{\alpha + b_{1b} + b_{1c}}{b_0}; \tag{3.16}$$

$$b_{1b} = \frac{\partial T_C}{\partial x}\frac{\kappa}{\rho H}\left[(\mu R_E - 1)(L/c_K) - (H_2/\epsilon_s H_1)\right], \tag{3.17}$$

$$b_{1c} = \frac{\partial T_C}{\partial z}\frac{\kappa}{\rho H}\left[(\beta H_2/\epsilon_s^2) + \epsilon(LH/c_K^2) + c_R R_W(1 - R_E)(H_1/c_K^2)\right], \tag{3.18}$$

$$b_2 = \frac{\partial T_C}{\partial x}(c_K/H)R_W(\mu R_E - 1) + \frac{\partial T_C}{\partial z}(c_R H_1/LH)(1 - R_E R_W), \tag{3.19}$$

$$b_3 = (w_C/b_0 H_B)T_0, \tag{3.20}$$

$$b_4 = R_W/H^*, \tag{3.21}$$

and

$$b_5 = (LH/H^* c_K^2)\frac{\kappa}{\rho H}. \tag{3.22}$$

Some typical values when $R_E = 0.5$ and $R_W = 0.75$ are $a_1 = 0.004$ days^{-1},

$b_4 = 0.02$ metres^{-1}.

3.1.1 Nondimensionalisation

At this stage the parameter space of the model is 7 dimensional, with two contributions from the h equation and five from the T equation. It is useful to reduce this parameter space by rescaling h,T and t appropriately. One way to do this is to write

$$\hat{h} = b_4 h, \tag{3.23}$$

$$\hat{t} = a_1 t, \tag{3.24}$$

$$\hat{T} = (a_2 b_4 / a_1) T. \tag{3.25}$$

This transforms (3.11) and (3.1) into

$$\frac{d\hat{h}}{d\hat{t}} = -\hat{h} - \hat{T} \tag{3.26}$$

and

$$\frac{d\hat{T}}{d\hat{t}} = (b_1/a_1)\hat{T} + (b_2 a_2/a_1^2)\hat{h} + (b_3 b_4 a_2/a_1^2)\tanh[\hat{h} + (b_5 a_1/b_4 a_2)\hat{T}]. \tag{3.27}$$

For convenience, let

$$\eta = (b_4 a_2/b_5 a_1), \tag{3.28}$$

$$\nu = (b_3 b_5/a_1), \tag{3.29}$$

$$P = (b_1 + b_3 b_5)/a_1 - 1 \tag{3.30}$$

and

$$Q = (b_2 + b_3 b_4)a_2/a_1^2 - (b_1 + b_3 b_5)/a_1. \tag{3.31}$$

Then, removing the hats from the rescaled variables and writing (3.11) and (3.1) in the new nondimensional form,

$$\frac{dh}{dt} = -h - T, \tag{3.32}$$

$$\frac{dT}{dt} = (P+1)T + (P+Q+1)h + \eta\nu[\tanh(h + T/\eta) - (h + T/\eta)], \tag{3.33}$$

a planar four parameter system. Note that the expression in square brackets above is fully nonlinear, with a Taylor expansion around $(h, t) = 0$ starting with cubic terms. The system can then be written in one line

$$\frac{d\mathbf{\Theta}}{dt} = M\mathbf{\Theta} + \eta\nu[\tanh N\Theta - N\Theta], \tag{3.34}$$

where $\Theta_1 = h$, $\Theta_2 = T$,

$$M = \begin{pmatrix} -1 & -1 \\ P+Q+1 & P+1 \end{pmatrix} \tag{3.35}$$

and

$$N = \begin{pmatrix} 0 & 0 \\ 1 & 1/\eta \end{pmatrix}. \tag{3.36}$$

This system is then completely described by the state vector $\mathbf{\Theta} = (h, T)^T$; a notation which shall be used throughout this study.

3.1.2 Regime Behaviour

Consider the points in the (h, T) phase space ($\mathbb{R}^2$) satisfying $d\mathbf{\Theta}/dt = 0$, that is

$$0 = -h - T, \tag{3.37}$$

$$0 = (P+1)T + (P+Q+1)h + \eta\nu[\tanh(h + T/\eta) - (h + T/\eta)], \tag{3.38}$$

so $h = -T$ and thus

$$[Q + \nu(1-\eta)]T = \eta\nu \tanh[T(1-\eta)/\eta]. \tag{3.39}$$

The right hand side of this expression looks like $\nu(1-\eta)T$ in the vicinity of $T = 0$, flattening out to $\pm\eta\nu$ as $T \to \pm\infty$. The left hand side is a straight line which intersects the right hand in one place (the origin) if $Q > 0$, and three places if $Q \leq 0$: the origin and the two nontrivial solutions of (3.39). Positive Q values then correspond to a single equilibrium, while negative or zero Q values to a multiple equilibria regime.

Stability of fixed point at (h, T)=0

Examined first is the case where $Q > 0$. Linearising (3.34) about $T = 0$ gives

$$\frac{d\boldsymbol{\Theta}}{dt} = M\boldsymbol{\Theta}, \tag{3.40}$$

and eliminating h from the equations leads to a single ODE in T

$$\frac{d^2T}{dt^2} - P\frac{dT}{dt} + QT = 0. \tag{3.41}$$

Substituting $T = e^{\sigma t}$ leads to the relation

$$\sigma^2 - P\sigma + Q = 0, \tag{3.42}$$

which is satisfied when

$$2\sigma = P \pm \sqrt{P^2 - 4Q}. \tag{3.43}$$

In regimes where $P < 0$, solutions decay away and the point $T = 0$ is a stable equilibrium. Conversely, $P > 0$ corresponds to an unstable fixed point at $T = 0$, and if $P^2 < 4Q$ these solutions are oscillatory, unstable spirals as depicted in chapter 1.

Multiple equilibria

As Q is taken from a positive value to a negative one across zero, the system undergoes a bifurcation. At $Q = 0$, this bifurcation is either a pitchfork or a Hopf bifurcation, whereby the origin becomes unstable and the solution heads to a different equilibrium point or a stable limit cycle. As for the nonzero equilibria, there are two solutions at $T = (T^+, T^-)$. These can be calculated by solving

$$QT^{\pm} = \nu\eta(\tanh[(1-\eta)T^{\pm}/\eta] - [(1-\eta)T^{\pm}/\eta]). \tag{3.44}$$

When $|T^{\pm}|$ the above equation is approximated by a Taylor series about zero, the solutions are given by $T = 0$ and

$$T^{\pm} \approx \pm\sqrt{\frac{3Q\eta^2}{\nu(\eta-1)^3}}. \tag{3.45}$$

It is worth noting that $T^{\pm}$ is independent of P. There are some parts of parameter space where $T^{\pm}$ are stable, and can be especially sensitive to initial conditions. Figure 3.2 shows an example of this, where three initially close orbits have three distinct asymptotic solutions. There are two basins of attraction surrounding T^+ and T^-. Initial states inside these basins will tend towards the corresponding fixed point, while those outside will end up on the limit cycle. Stability of $T^{\pm}$ can be found by replacing P with $P^{'}$ where $P' = P + P_0$ with

$$P_0 = \nu \tanh^2\left[\frac{T^{\pm}(1-\eta)}{\eta}\right] \tag{3.46}$$

and $Q^{'} = Q - Q_0$ with

$$Q_0 = (1-\eta)\nu \tanh^2\left[\frac{T^{\pm}(1-\eta)}{\eta}\right], \tag{3.47}$$

so if $0 < P < P_0$ these points will attract local trajectories.

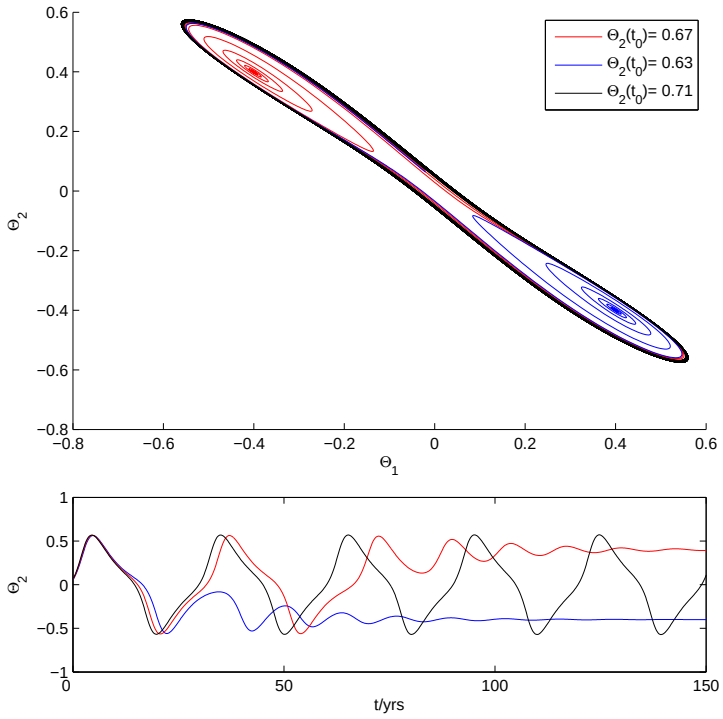

Figure 3.2: 2-box model operating in a low frequency regime $(P, Q, \eta, \nu) = (0.225, -0.05, 1/2, 2)$ with nearby initial Θ_2 coordinates and $\Theta_1 = -0.02$ demonstrating sensitivity to initial conditions.

3.1.3 Approximation of limit cycle

Growing oscillatory solutions are curbed by the tanh nonlinearity, and tend toward an attracting closed curve or limit cycle. It is possible to make an approximation for small Q, just after the bifurcation point, of the limit cycle solution in the (h, T) plane. Similar work on the approximation of recharge oscillator type limit cycles has been done by Wu, using a homotopy analysis method for strong nonlinearity [64]. This method is valid for the weakly nonlinear limit for which oscillatory behaviour is nearly sinusoidal, and the tanh term is expanded via Taylor series and approximated as

$$\tanh[h + T/\eta] \approx (h + T/\eta) - (h + T/\eta)^3/3. \tag{3.48}$$

The truncated nonlinear system is

$$\frac{dh}{dt} = -h - T, \tag{3.49}$$

$$\frac{dT}{dt} = (P+1)T + (P+Q+1)h - (\nu/3\eta^2)(\eta h + T)^3. \tag{3.50}$$

Using a guessed solution

$$T = A\cos(\sigma t), \tag{3.51}$$

$$h = B\cos(\sigma[t-\delta]). \tag{3.52}$$

Substitution then reveals

$$\sigma = \tan(\sigma\delta) \tag{3.53}$$

and

$$B = -A\cos(\sigma\delta). \tag{3.54}$$

Expanding out the nonlinear term and matching the harmonic terms gives

$$\cos^2(\sigma\delta) = \frac{1}{P(1-\eta)Q+1}, \tag{3.55}$$

and the existence of solutions of the assumed form requires that

$$P(1-\eta) + Q > 0. \tag{3.56}$$

Frequency of oscillation can be shown to be

$$\sigma = \sqrt{P(1-\eta)+Q}, \tag{3.57}$$

and similarly the amplitude

$$A^2 = \frac{4P\nu\eta^2}{\cos^2(\sigma\delta)[(1+\eta)^2-1]+1}. \tag{3.58}$$

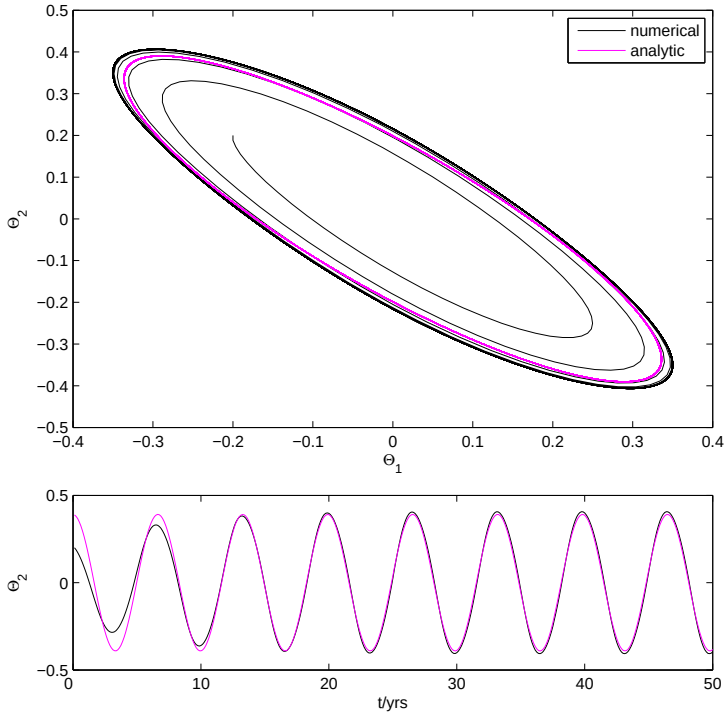

Figure 3.3: ENSO-like 2-box model $(P, Q, \eta, \nu) = (0.14, 0.28, 1/2, 2)$ with sinusoidal limit cycle (black curve), compared with linear approximation (magenta curve).

3.1.4 Geometric Interpretation

The approximation of solutions as given above is realised geometrically as an ellipse embedded in the (h, T) space, centered around zero. Due to the delay term $\cos(\sigma[t-\delta])$, the two axes of this ellipse will not be parallel to the h and T axes, but will be rotated around by some unknown angle. The purpose of this section is to determine specific geometric properties of this rotated ellipse. Parametric equations for an ellipse are

$$\begin{aligned} x &= a\cos\theta, \\ y &= b\sin\theta, \end{aligned}$$

where taking $\theta \in [0, 2\pi]$ defines a closed curve. x and y then satisfy

$$(x/a)^2 + (y/b)^2 = 1, \tag{3.59}$$

or

$$\mathbf{x}^T\mathbf{x} = 1 \tag{3.60}$$

where $\mathbf{x} = (x/a, y/b)$. Constants a and b define the axes of the ellipse. Equation (3.51) is of the form

$$\begin{aligned} x &= a\cos\theta \\ y &= b(\cos\theta\cos\phi + \sin\theta\sin\phi), \end{aligned}$$

or

$$\begin{aligned} (x/a) &= \cos\theta \\ (y/b) &= (x/a)\cos\phi + \sin\theta\sin\phi, \end{aligned}$$

and the aim is to express the equations above in the same form as (3.60). Beginning with taking the square of both sides of the expression for (y/b), and making use of the relation $\sin^2\theta = 1 - (x/a)^2$ gives

$$(x/a)^2 + (y/b)^2 - 2(x/a)(y/b)\cos\phi = \sin^2\phi. \tag{3.61}$$

Dividing through by $\sin^2\phi$ and defining

$$(X, Y) = \frac{(x/a, y/b)}{\sin\phi} \tag{3.62}$$

gives

$$X^2 + Y^2 - 2\gamma XY = 1, \tag{3.63}$$

where $\gamma = \cos\phi$. Finally, defining a new basis (p,q) such that

$$X = \frac{p+q}{\sqrt{2(1-\gamma)}} \quad Y = \frac{p-q}{\sqrt{2(1-\gamma)}} \ , \tag{3.64}$$

the resulting equation is of the form

$$\mathbf{p}^T\mathbf{p} = 1. \tag{3.65}$$

with $\phi = (p, q)$. Thus, (3.51) corresponds to a scaled ellipse rotated by an angle $\pi/4$ about the origin. This is useful to know for instance if it was necessary to initialise the 2-box model. An initial state vector may be projected near the attractor using the ellipse approximation. If the transient, dissipative motion is normal to the limit cycle while long term behaviour is tangent, any initial vector can be projected onto the attractor using the matrix

$$\Pi = R^{-1}S(\theta)R, \tag{3.66}$$

where R is the rotation matrix

$$R = \frac{1}{\sqrt{2}}\begin{pmatrix} 1 & 1 \\ -1 & 1 \end{pmatrix}, \tag{3.67}$$

and the operator $S(r, \theta)$ acts on the new set of polar coordinates in the rotated frame, scaling a vector of length r by a factor $f(\theta)/r$ where $f(\theta)$ is the equation for an ellipse. The basis is then rotated back to its original position. Through this process, any initial condition is radially projected onto the ellipse and information corresponding to fast, transient motion is destroyed, assuming the ellipse is a perfect approximation of the actual limit cycle. A comparison of an approximate solution with a limit cycle in the phase plane can be seen in figure 3.3. Once the numerical solution has dissipated onto the cycle, the period and amplitude are in agreement with the sinusoidal approximation.

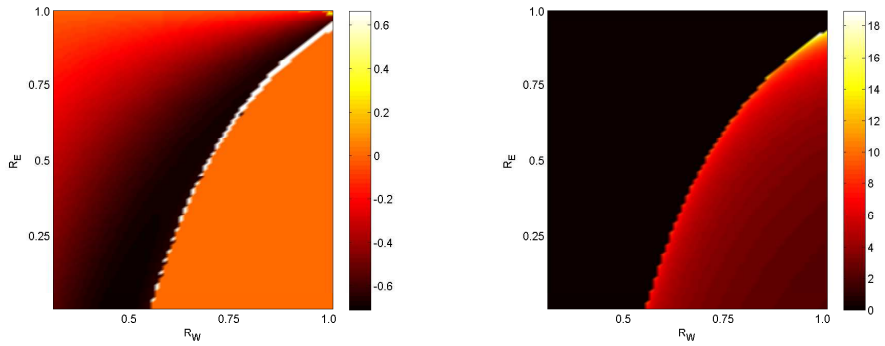

Figure 3.4: Mean of fine scale SST coordinate Θ_2 (left) and period (right, in years, as calculated from winding number) for the 2-box as a function of reflection coefficients R_E and R_W.

3.1.5 2-box Analytical Summary

To summarise the regime behaviour of the 2-box model, for values of $Q > 0$,

- If $P < 0$, the origin is a point attractor.
- If $P = 0$, orbits form a family of ellipses centered at the origin.
- If $P > 0$, the origin repels all orbits.
- In any case when $P^2 < 4Q$ the solutions are oscillatory, and the amplitude of oscillation tends towards zero as $P \to 0$ from above.

Similarly, when $Q < 0$,

- If $0 < P < -Q/(\eta - 1)$, the origin repels orbits, and there are two point attractors outside the origin. Orbits will go to one or the other depending on initial conditions.
- If $Q/(\eta - 1) < P < P_0$ there exist both stable limit cycles centered on the origin and point attractors further from the origin.
- If $Q/(\eta - 1) < P_0 < P$ there are limit cycles centered on the origin.

In other words, there is a bifurcation point at $Q = 0$ which is either a pitchfork ($P < Q/(\eta - 1)$) or Hopf ($P \geq Q/(\eta - 1)$). This will be confirmed numerically

later, but first there will be some discussion of the methods used to integrate the 2-box, as well as the more complex models that follow it.

3.1.6 Numerical Integration

The numerical solution to (3.34) is found by integrating over discrete time intervals with an Adams-Bashforth multistep method. This approximates the time derivative in (1.6) at step i by a linear combination of vectors at steps $i - s$ to $i - 1$, where s is the order. The first order is just the Euler method

$$\mathbf{x}_i = \mathbf{x}_{i-1} + \Delta t \mathbf{f}(\mathbf{x}_{i-1}), \tag{3.68}$$

while the 2^{nd} order is given by

$$\mathbf{x}_i = \mathbf{x}_{i-1} + \Delta t \left[\frac{3}{2}\mathbf{f}(\mathbf{x}_{i-1}) - \frac{1}{2}\mathbf{f}(\mathbf{x}_{i-2}) \right], \tag{3.69}$$

the second order being the maximum used throughout this study. Thus, beginning timestep uses the Euler method while all those which follow store the right hand side from the previous two timesteps in a $(2 \times n)$ array, where n is the number of boxes or length of $\mathbf{x}_i$, and calculate the state at time $i\Delta t$ using the above formula. Before integrating directly, it should be checked whether the model satisfies the criteria which ensure basic numerical stability.

The Courant Friedrichs Lewy Condition

As for any model which involves the propagation of information across a spatial domain, it is essential to introduce the condition which places some constraints on the size of timestep Δt. A balance must be maintained between the spatial and temporal resolution of a model, in that

$$v \frac{\Delta t}{\Delta x} \leq 1, \tag{3.70}$$

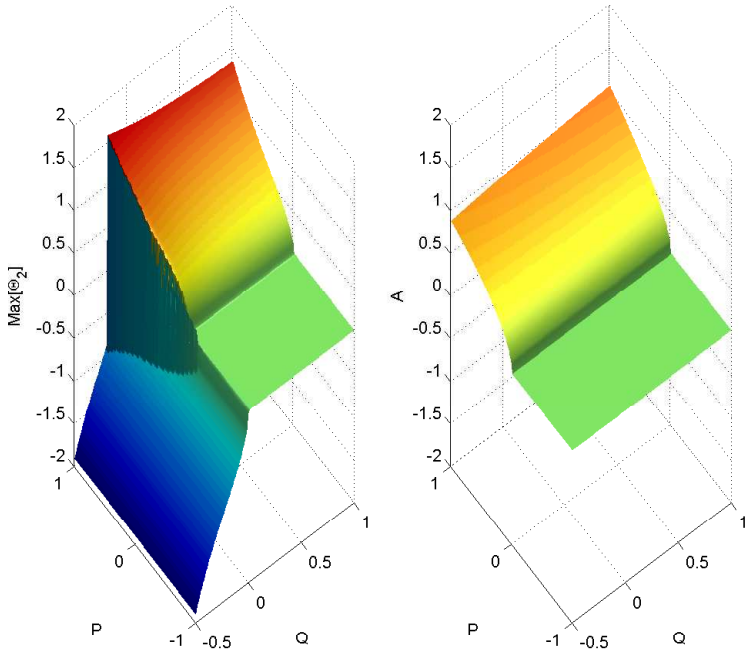

Figure 3.5: Map of maximum value of Θ_2 (on the right hand side) compared with amplitude of linear approximation of 2-box for varying (P, Q) values (on the left hand side). The range of parameters is truncated due to globally unstable solutions where nonlinearity dominates.

were Δt is the timestep, Δx is the grid spacing and v is the maximum velocity of propagation. This places an upper bound on the maximum possible timestep which cannot be crossed, and this threshold decreases with the number of boxes. However, in some cases the condition can be bypassed, permitting longer minimum timesteps at no cost to the resolution. More detail will be provided in the initialisation section.

3.1.7 Time Series Statistics

To gain an overview on how orbits behave throughout different regions of the parameter space, a brief summary of some statistical tools which will be used to analyse timeseries elements $\Theta_i(j\Delta t)$ where i indicates phase space coordinate

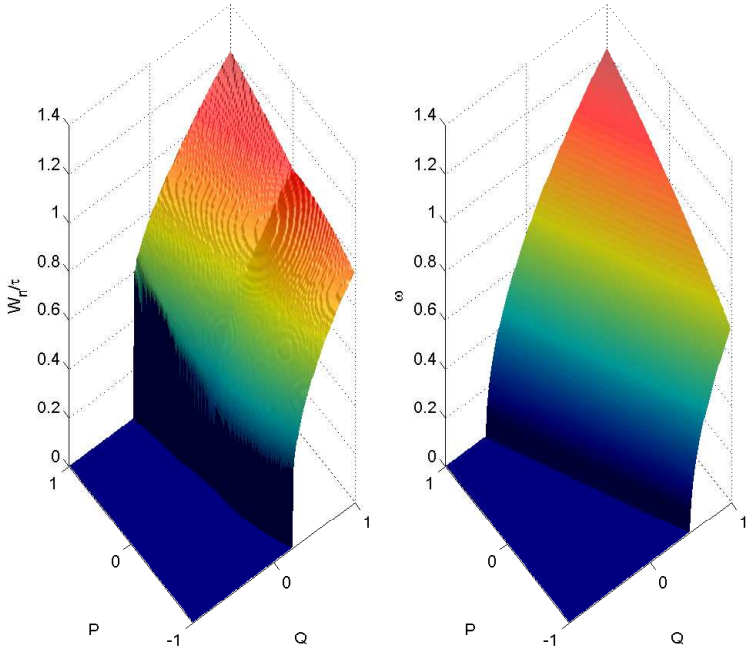

Figure 3.6: Map of scaled winding number of Θ_2 (on the right hand side) compared with frequency of linear approximation of 2-box for varying (P, Q) values (on the left hand side).

and j the timestep. These include mean

$$\text{Mean}[\Theta_i] = \frac{1}{N}\sum_{j=1}^{N}\Theta_i(j\Delta t), \tag{3.71}$$

range

$$\text{Range}[\Theta_i] = \max[\Theta_i(j\Delta t)] - \min[\Theta_i(j\Delta t)], \tag{3.72}$$

winding number,

$$W_n[\Theta_i] = \sum_{j=1}^{N-1} H\left(\text{sign}[\Theta_i((j+1)\Delta t)] - \text{sign}[\Theta_i(j\Delta t)]\right), \tag{3.73}$$

used for the calculating the period of the 2-box model, where $H(\cdot)$ is the Heaviside step function which is 1 if the sign of $\Theta_i(j\Delta t) < 0$, $\Theta_i((j+1)\Delta t) > 0$ and 0

otherwise. Another timescale approximation, the near-period, is calculated the same way as Ghil et al[24]

$$P_n[\Theta_i] = n_p \delta t, \tag{3.74}$$

where n_p is the integer which minimises

$$t_n = \frac{\sum_{n_p+1}^{N} \left[\Theta(n\Delta t) - \Theta((n-n_p)\Delta t)\right]^2}{N - n_p}, \tag{3.75}$$

for the values $n \in [1, N]$. The numerator will locate the first element when a pattern repeats itself, and the denominator ensures the first is chosen rather than a later period. This is more suited than the winding number for calculating the period of the 10-box model described later. The reason period is calculated for the 2-box in a different way than the 10-box is because the former has a continuous range of periodicities, while the latter has a discrete range due to phase locking. Mean value and period of Θ_2 were calculated as reflection coefficients R_E and R_W are varied, and figure 3.4 shows a clear divide between oscillatory and nonoscillatory behaviour for high R_W/low R_E and low R_W/high R_E respectively. While there is no evidence of parametric instability at this stage, later models which are discretisations of the same original PDE system do show signs of this. Maximum value and winding number of the 2-box for varying P and Q values are shown in figures 3.5 and 3.6, along with the limit cycle approximation of amplitude and frequency. These compare well throughout much of the parameter space, particularly in the $(+P, +Q)$ quadrant.

Table 3.1: 2-box Parameters

Parameter	Value
P	$[-1, 1]$
Q	$[-1, 1]$
μ	2
η	0.5

3.2 2-strip Revisited

In the lead up to the n-box model, a separate nondimensionalisation is required for the PDEs prior to discretisation. This must be more general than the previous treatment and be prepared for cases where there is no Sverdrup balance. To make the three equations dimensionless, each variable v is written in the form

$$v = v^* \hat{v} \tag{3.76}$$

where $\hat{v}$ is a number and v^* is the characteristic unit of a variable. Beginning with the 2-strip equations, the zonal coordinate x is scaled with the half basin width L, and t with the time taken for a Kelvin signal to cross this width

$$x^* = L \tag{3.77}$$

$$t^* = \frac{x^*}{c_K}. \tag{3.78}$$

Moving onto the temperature equation, the most obvious choice for scaling h_e is H^*, and

$$T^* = \frac{L w_C T_0}{c_K H_B} \tag{3.79}$$

as this tidies up the tanh term significantly. The magnitude of atmospheric forcing, represented by a central block on the equator, becomes

$$\hat{F}(t) = \kappa(\hat{t}) \int_0^1 \hat{T}_e(\hat{x}, \hat{t}) d\hat{x} \tag{3.80}$$

where

$$\kappa_0 = \frac{t^* T^*}{H^* \rho c_K} \mu_c. \tag{3.81}$$

As was mentioned in the previous chapter,

$$\kappa(t) = \kappa_0 + \kappa_a x_1(t). \tag{3.82}$$

Removing hats, the equations for evolution of thermocline anomalies are

$$\left(\frac{\partial}{\partial t}+\varepsilon\right)(h_e-h_n)+\frac{\partial h_e}{\partial x}=\kappa(t)F_e, \tag{3.83}$$

$$\left(\frac{\partial}{\partial t}+\varepsilon\right)h_n+r_s\frac{\partial h_n}{\partial x}=r_f\kappa(t)F_e, \tag{3.84}$$

and temperature anomalies

$$\partial_t\left(T_e+\gamma h_e\right)=\alpha T_e+\sigma F_e+\tanh(h_e), \tag{3.85}$$

where

$$F_e(x,t)=\kappa(t)\Pi(2x/3)\int_0^1 T_e(x,t)dx \tag{3.86}$$

for a uniform wind stress model, where

$$\varepsilon=t^*\epsilon, \tag{3.87}$$

$$r_s=\frac{c_R}{c_K}, \tag{3.88}$$

$$\alpha=t^*\alpha_T, \tag{3.89}$$

$$\gamma=-\frac{\partial T_C}{\partial z}(H^*H_1/T^*H), \tag{3.90}$$

$$\sigma=\frac{\partial T_C}{\partial z}(H^*H_2/T^*H)\frac{\beta c_K}{\epsilon_s^2}. \tag{3.91}$$

Over the model hierarchy development, three separate atmospheric parametrisations are used. Starting with the simplest, integrating (3.85) over the range $[0,1]$ eliminates the x dependence of T_e, leaving

$$\frac{d\bar{T}_{eE}}{dt}=\left[\alpha+\frac{1}{3}\sigma\kappa(t)\right]\bar{T}_{eE}+\int_0^1\left[\tanh(h_e)-\gamma\frac{\partial h_e}{\partial t}\right]dx, \tag{3.92}$$

where

$$\bar{T}_{eE}=\int_0^1 T_e dx. \tag{3.93}$$

The second begins with dividing the interval $[0,1]$ into three, and the atmosphere is coupled to the SST over the first two regions $\bar{T}_{e1}(x,t), x \in [1/3, 2/3]$ and $\bar{T}_{e2}(x,t), x \in [0,1/3]$. This reverse numbering is due to the numbering of discretised coordinates, which will be discussed later with regard to the n-box model. There are then two dynamic temperature equations

$$\frac{d\bar{T}_{e1}}{dt} = [\alpha + \sigma\kappa(t)]\,\bar{T}_{e1} + \int_{1/3}^{2/3} \left[\tanh(h_e) - \gamma\tfrac{\partial h_e}{\partial t}\right] dx, \tag{3.94}$$

$$\frac{d\bar{T}_{e2}}{dt} = \alpha\bar{T}_{e2} + \int_{0}^{1/3} \left[\tanh(h_e) - \gamma\tfrac{\partial h_e}{\partial t}\right] dx, \tag{3.95}$$

where the main difference between the two equations is that $\bar{T}_{e2}$ is in a wind forced region while $\bar{T}_{e1}$ is not. From this stage on (3.94) will be referred to as coarse (atmospheric) parametrisation. The third and most complex parametrisation is pointwise and does not involve spatial averaging

$$\partial_t \left(T_e(x,t) + \gamma h_e(x,t)\right) = \alpha T_e + \sigma F_e + \tanh(h_e), \tag{3.96}$$

where

$$F_e(x,t) = \kappa(t) T_e(x + x_c, t). \tag{3.97}$$

Here $x_c = \frac{1}{3}$ quantifies the nonlocality of the atmospheric response to an SST anomaly. This will be referred to as fine (atmospheric) parametrisation and will be implemented at the top of the model hierarchy. There are some steps before this stage, and the next model above the 2-box in the complexity scale is the 10-box model, which is the first to incorporate the annual cycle.

3.3 The 10-box model

The next stage of advancement before discussing the general PDE system can be seen as a stepping point in between a conceptual and intermediate complexity model. While still a relatively simple model, the 10-box has a much larger phase space and therefore more degrees of freedom, allowing for more complex

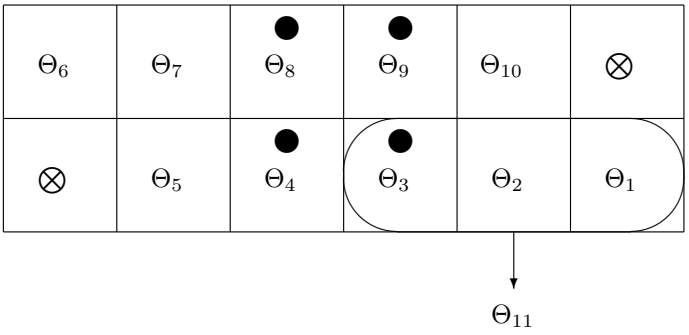

Figure 3.7: 10-box diagram, where boxes marked with a filled circle are wind forced and thermocline anomalies are averaged over the area within the loop. Boxes marked with $\otimes$ are not integrated, and correspond to $\Theta_5^{\leftarrow}$ in the equatorial and $\Theta_1^{\uparrow}$ in the northern strip.

behaviour and a better spatial resolution of thermocline structure than the 2-box. A convenient discretisation of the thermocline depth which resolves both the central forced patch (one third of the unit interval) and the eastern interaction zone affecting the forcing (one half of the unit interval) is six boxes in each strip. This, together with the SST and seasonal cycle coordinates amount to a thirteen dimensional phase space. Reflective boundary conditions reduce the space to eleven dimensions, of which ten are box variables, one an average SST coordinate and two are seasonal cycle simple harmonic motion resulting in a simple model which behaves in a similar way to the continuous case. Contributions to the phase space then come from the thermocline anomaly $\Theta_1 \to \Theta_{10}$ (describing h_e and h_n), east equatorial SST Θ_{11} (or T_{eE}), and the simple harmonic motion of the annual cycle comes from Θ_{12} and Θ_{13}. The configuration of box variables is demonstrated in 3.7, where coordinates with indices $1 \leq i \leq 5$ correspond to the equatorial strip and $6 \leq i \leq 10$ the northern strip boxes. The governing nondimensionalised equations for the equatorial strip are found using an upstream difference appropriate for the Kelvin wave propagation (without

Sverdrup balance),

$$\frac{d}{dt}(\Theta_i - \Theta_i^{\uparrow}) = \epsilon(\Theta_i^{\leftarrow} - \Theta_i) + \frac{1}{\Delta}(\Theta_i^{\leftarrow} - \Theta_i) + F_i, \tag{3.98}$$

$$F_i = \begin{cases} (\kappa_0 + \kappa_a \Theta_{12})\Theta_{11} & \text{if } 3 \leq i \leq 4; \\ 0 & \text{otherwise.} \end{cases} \tag{3.99}$$

Here ϵ is a damping term, Δ is the box spacing, and Θ_{12} is oscillating with unit amplitude and period one year. The $\leftarrow$ and $\uparrow$ tags of Θ_i refer to the boxes to the left and above of Θ_i respectively, where $\Theta_1^{\uparrow} = R_E\Theta_1$ and $\Theta_5^{\leftarrow} = R_W\Theta_6$ due to the boundary conditions. The northern strip equations implement an upstream difference for the Rossby wave

$$\frac{d}{dt}\Theta_i = -\epsilon\Theta_i + \frac{r_s}{\Delta}(\Theta_i - \Theta_i^{\rightarrow}) + G_i, \tag{3.100}$$

$$G_i = \begin{cases} r_f(\kappa_0 + \kappa_a \Theta_{12})\Theta_{11} & \text{if } 8 \leq i \leq 9; \\ 0 & \text{otherwise.} \end{cases} \tag{3.101}$$

The factor r_f relates a forcing of a Kelvin wave in the equatorial strip to that of a Rossby wave in the northern strip, while r_f is the ratio of Rossby and Kelvin wave speeds, the $\rightarrow$ tag of Θ_i refers to boxes to the right of Θ_i, and the boundary conditions impose $\Theta_{10}^{\rightarrow} = R_E\Theta_1$.

The 10-box model implements a very primitive atmospheric parametrisation (3.92) whereby the SST coordinate T_{eE}, with index $i = 11$, is the temperature integrated over the eastern half of the equatorial strip

$$\Theta_{11} = \Delta \sum_{i=1}^{3} T_i, \tag{3.102}$$

whose evolution is given by

$$\frac{d}{dt}\left(\Theta_{11} - \gamma\Delta \sum_{k=1}^{3} \Theta_k\right) = \left[\alpha + \frac{\sigma}{3}(\kappa_0 + \kappa_a\Theta_{12})\right]\Theta_{11} + \Delta \sum_{k=1}^{3} \tanh(\Theta_k), \tag{3.103}$$

where α and γ are constants relating to feedback and upwelling respectively, while σ quantifies the degree to which wind stress affects SST dynamics. Finally, this model includes two annual cycle coordinates which are in perpetual simple harmonic motion

$$\Theta_{12} = -\omega\Theta_{13}, \tag{3.104}$$

and

$$\Theta_{13} = \omega\Theta_{12}. \tag{3.105}$$

Subscript a has been dropped here as from this point onwards ω will represent the timescale of the annual cycle.

3.3.1 Regime Behaviour

Table 3.2: 10-box Parameters

Parameter	Physical Interpretation	Value
ϵ	Weak ocean adjustment damping	0.03
α_0	SST damping rate	0.43
γ	Thermocline motion SST factor	0.19
κ_0	Ocean/Atmosphere Coupling strength	[4/3,8/3]
R_E	Eastern boundary reflection coefficient	[0,1]
R_W	Western boundary reflection coefficient	[0,1]
r_s	Ratio of Rossby/Kelvin wave speeds	-0.25
r_f	Ration of atmospheric forcing of Rossby/Kelvin waves	-0.25
σ	Shear influence on SST	0.15

As in Jin[15], the parameter space is mapped out to find the regions of different orbit behaviour. The ranges of (R_E, R_W) are $([1/4, 1], [0, 3/4])$ while $\kappa_0 \in [2/3, 3/2]$ and $\kappa_a = \kappa_0$. Realistic values of R_E and R_W are around 0.5 and 0.75 respectively, while κ_0 is closer to 2 with κ_a comparatively small. Distinct regimes are found by analysing the the statistical properties of timeseries as parameters are varied. These properties include near-period in figure 3.8, range in 3.9 and mean in 3.10. The differences between parameter maps of the 2-box model in (P, Q) space and the 10-box in (κ_0, R_E, R_W) space are immediately apparent in the period map 3.8, which displays a landscape with a discrete spectrum of timescales, compared with the continuous map in figure 3.6. This is due

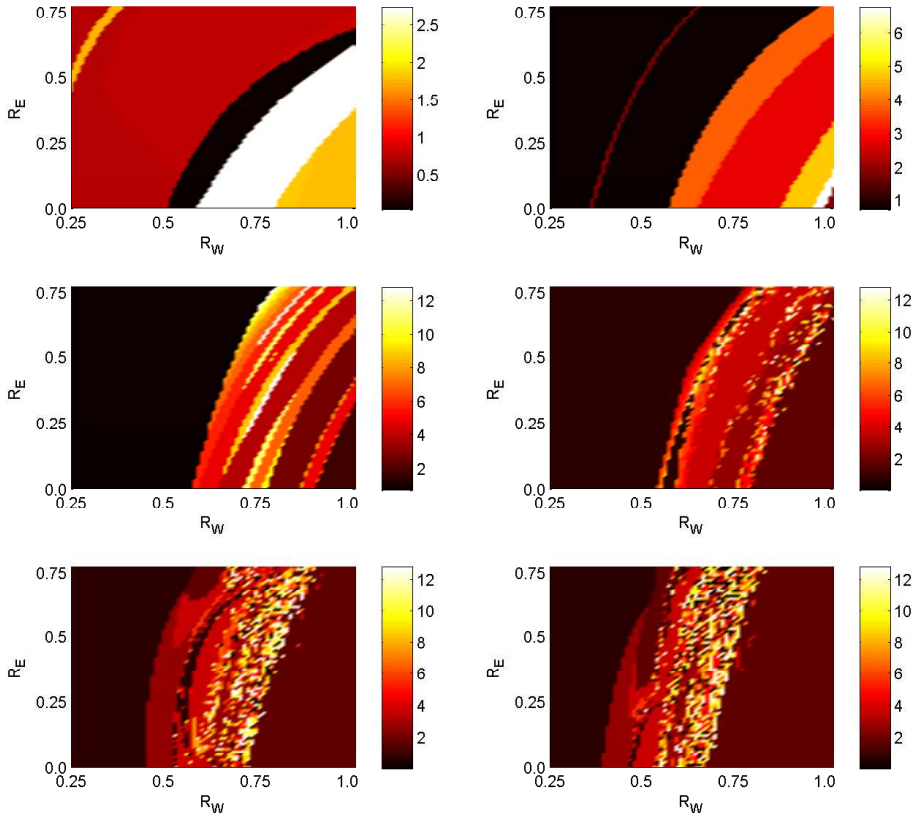

Figure 3.8: Near-Period of 10-box (in years) $T_{eE} = \Theta_{n+1}$ for $R_E \in (0, 0.75)$ and $R_W \in (0.25, 1.0)$ for the values $\kappa_0 = (4/6, 5/6)$ top (left,right), $\kappa_0 = (1, 7/6)$ centre (left,right), $\kappa_0 = (8/6, 9/6)$ bottom (left,right).

to the quantisation of periods coming about through the locking of the ENSO phase to the annual cycle. Phase locking is first visible as discontinuous bands of constant period at low coupling, evolving into low frequency ridges which then fragment and begin to spread over the parameter space. The final stage is a thin band where frequency of oscillation is somewhat arbitrarily based on parameter choices (possibly due to structural instability), surrounded by uniform regions of small period. For low R_W values on the left hand side, trajectories oscillate with a one year period with nonzero mean (see figure 3.10), while for high R_W to the right they are period doubled, and oscillate about a mean $\mathbf{\Theta} = 0$. The

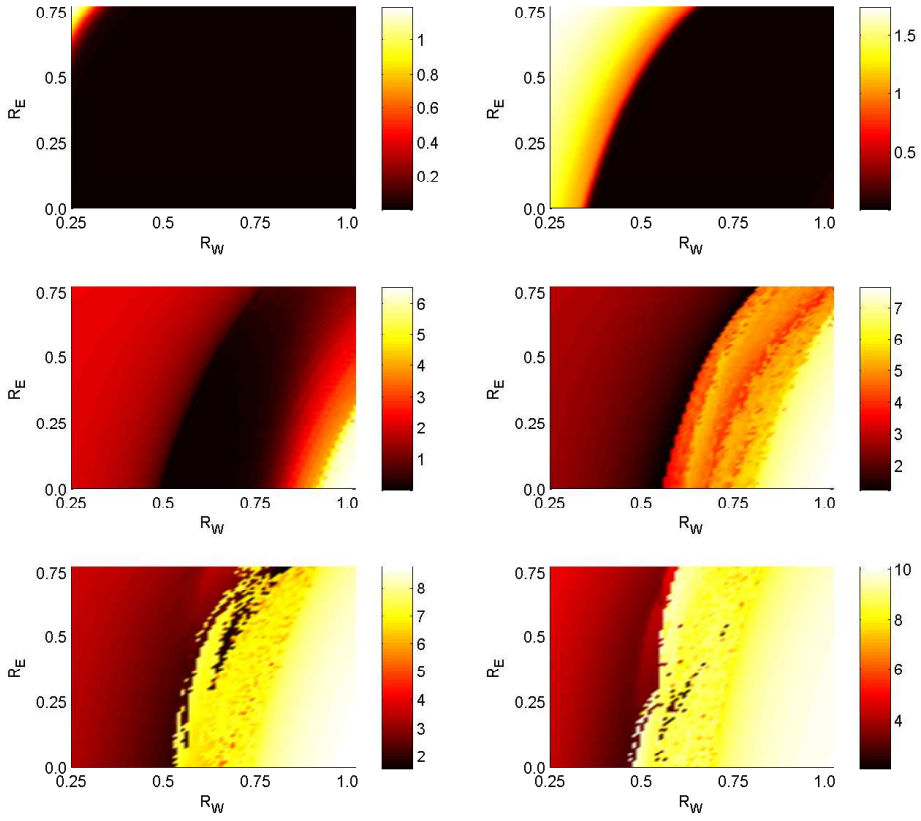

Figure 3.9: Range of 10-box $T_{eE} = \Theta_{n+1}$ for $R_E \in (0, 0.75)$ and $R_W \in (0.25, 1.0)$ for the values $\kappa_0 = (2/6, 5/6)$ top (left,right), $\kappa_0 = (1, 7/6)$ centre (left,right), $\kappa_0 = (8/6, 9/6)$ bottom (left,right).

average and range parameter maps (figures 3.10 and 3.9 respectively) look similar to the (P, Q) parameter maps 3.6 and 3.5 for weak coupling, with pitchfork type behaviour in one region (low R_W) and Hopf type in another (high R_W), separated by a stable belt. As coupling strengthens, eventually the pitchfork and Hopf regions collide, but there is no clear distinction between them. Instead they are separated by a rough, fractal boundary where there is no clear dominant behaviour. The irregular models similar to the observed ENSO exist in this liminal space between the two extremes. A more detailed analysis can be made by looking at phase portraits, Poincaré sections and spectra for these

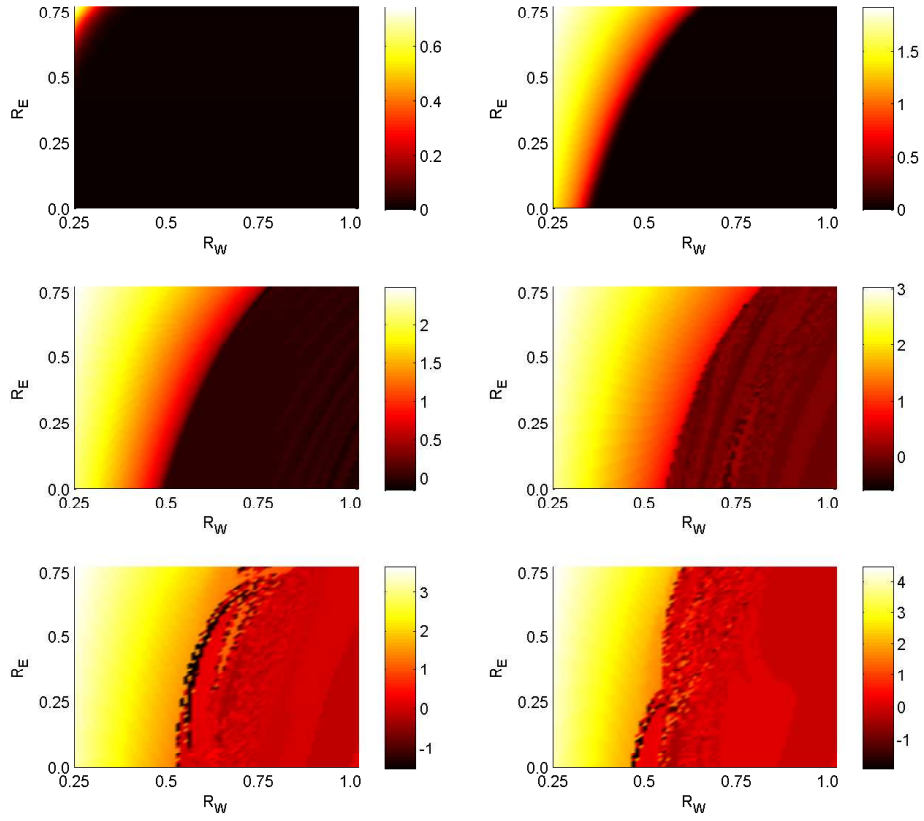

Figure 3.10: Mean of 10-box $T_{eE} = \Theta_{n+1}$ for $R_E \in (0, 0.75)$ and $R_W \in (0.25, 1.0)$ for the values $\kappa_0 = (2/6, 5/6)$ top (left,right), $\kappa_0 = (1, 7/6)$ centre (left,right), $\kappa_0 = (8/6, 9/6)$ bottom (left,right).

models, to be discussed now.

3.3.2 Analysis of Timeseries

Beginning with simplest behaviour, regions of strong coupling and reflection in the western boundary are dominated by period doubled annual orbits such as that shown in figures 3.11 and 3.12. This is confirmed by Poincaré section, where there are two separate intersection points at a fixed phase of the annual cycle, and spectrum, with a peak at two years. SST amplitudes are slightly larger than seen in nature, which is common for large κ_0, as can be seen in figure

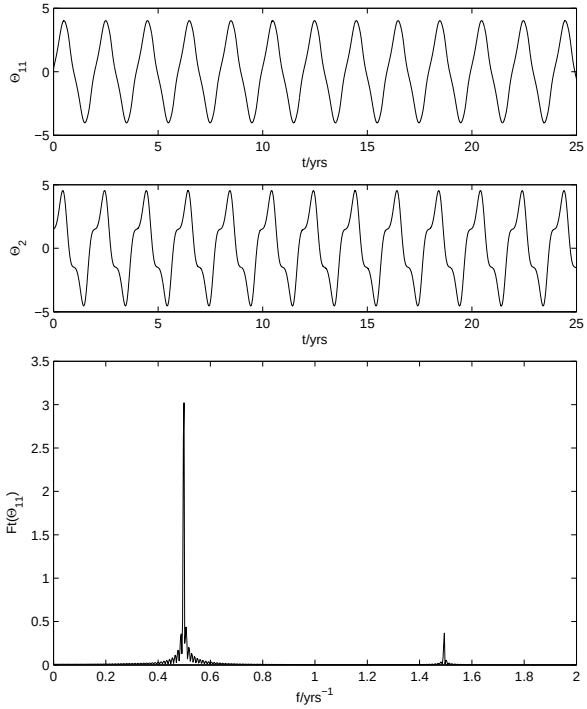

Figure 3.11: 10-box thermocline and SST timeseries with frequency spectrum (Fourier transform) for $(\kappa_0, R_E, R_W) = (4/6, 0.10, 0.95)$ and $\kappa_a = \kappa_0$.

3.9. For similar coupling strength values, and weak west boundary reflection, orbits oscillate around a nonzero equilibrium with a period of one year, similar to figures 3.3.2 and 3.14, where there is no La Niña. Here parameters have been chosen where trajectories oscillate irregularly around the warm phase, although for low R_W a regular periodic cycle is more common, as can be seen in figure 3.8. This can be explained physically as a permanent warm phase with seasonal fluctuations, where there is no low frequency oscillation as the upwelling Rossby wave is reflected as an upwelling Kelvin wave whose magnitude is insufficient to disturb the eastern SST anomaly.

An example which is close to real world ENSO is shown in figures 3.3.2 and 3.16. The orbits appear to be aperiodic with a frequency peak between three and four years. Evidence that the attractor is strange appears due to the irregular pattern formed at intersection points. The shape of the attractor could imply

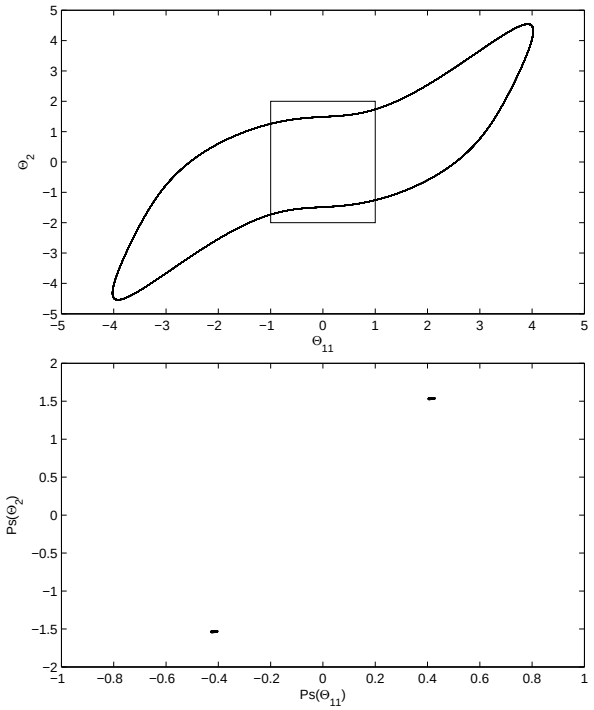

Figure 3.12: 10-box phase plot (top) and Poincaré section (bottom) for $(\kappa_0, R_E, R_W) = (4/6, 0.10, 0.95)$. Box in phase plot represents region section was sampled from.

that chaos arises through the breakup of a homoclinic orbit, whereby trajectories jump between two periodic orbits, one representing a warm and the other a cold phase. While it has been speculated that some of the 10-box models may be oscillating chaotically, there is as yet no quantitative proof that this is the case. The next section will show explicitly that these models have positive Lyapunov exponents, confirming that they demonstrate chaotic behaviour.

3.3.3 Lyapunov Spectra

Lyapunov exponents of the 10-box model are calculated for a variety of different parameters. The method[65][66] used here, based on the code provided by Wolf[54], takes an n-dimensional model and integrates it forward in time. Meanwhile, a set of n linear equations are time integrated which track the evo-

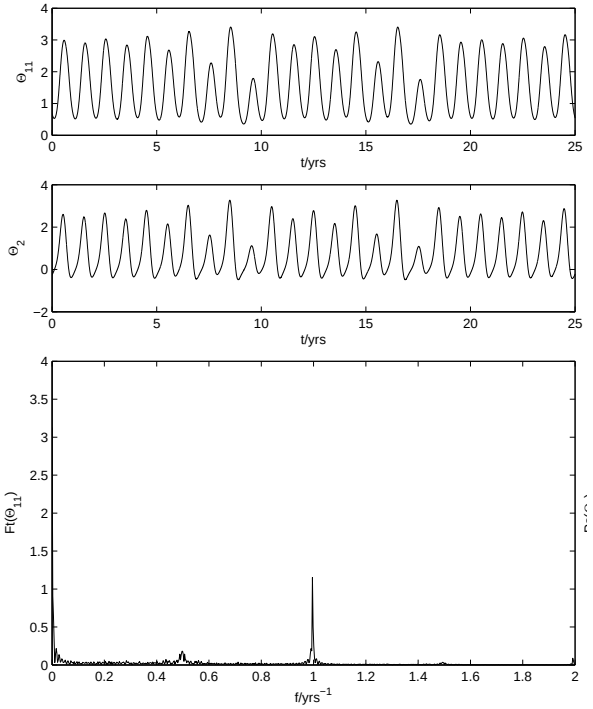

Figure 3.13: 10-box thermocline and SST timeseries with frequency spectrum (found by Fourier transforming timeseries) for $(\kappa_0, R_E, R_W) = (3/2, 0.43, 0.60)$ and $\kappa_a = \kappa_0$.

lution of a set of n basis vectors in the tangent space. There is a technical problem in that basis vectors have a tendency to line up in the same direction and diverge, but this can be overcome by performing periodic Gram-Schmidt reorthonormalisation on the set of basis vectors, that is defining a new basis

$$\begin{aligned}
\mathbf{e}_1^{'} &= \frac{\mathbf{e}_1}{\|\mathbf{e}_1\|} \\
\mathbf{e}_2^{'} &= \frac{\mathbf{e}_2 - \langle \mathbf{e}_2, \mathbf{e}_1^{'} \rangle \mathbf{e}_1^{'}}{\|\mathbf{e}_2 - \langle \mathbf{e}_2, \mathbf{e}_1^{'} \rangle \mathbf{e}_1^{'}\|} \\
&\vdots \\
\mathbf{e}_n^{'} &= \frac{\mathbf{e}_n - \langle \mathbf{e}_{n-1}, \mathbf{e}_{n-1}^{'} \rangle \mathbf{e}_1^{'} - \ldots - \langle \mathbf{e}_n, \mathbf{e}_1^{'} \rangle \mathbf{e}_1^{'}}{\|\mathbf{e}_n - \langle \mathbf{e}_{n-1}, \mathbf{e}_{n-1}^{'} \rangle \mathbf{e}_1^{'} - \ldots - \langle \mathbf{e}_n, \mathbf{e}_1^{'} \rangle \mathbf{e}_1^{'}\|}.
\end{aligned}$$

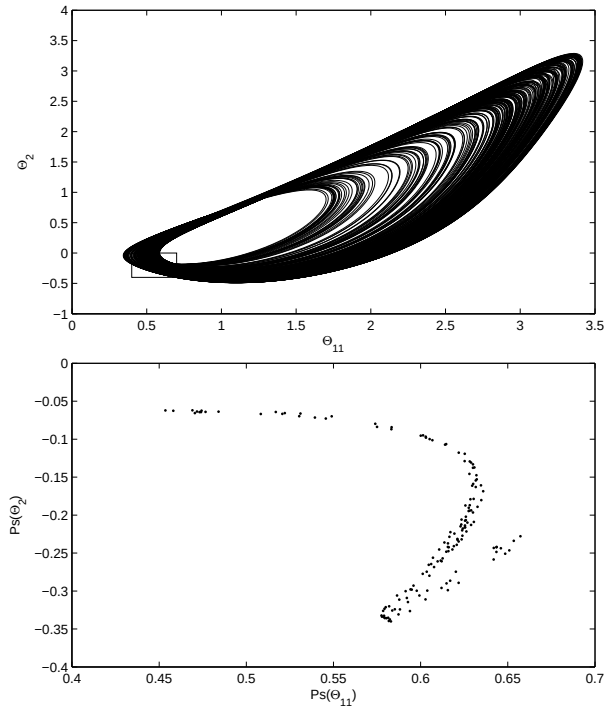

Figure 3.14: 10-box phase plot (top) and Poincaré section (bottom) for $(\kappa_0, R_E, R_W) = (3/2, 0.43, 0.60)$.

The code integrates $n(n+1)$ ordinary differential equations, renorthonormalising every k timesteps. Each time Gram-Schmidt is performed, the lengths of the basis vectors are measured. Taking the sum of these lengths gives a set of n numbers which is an approximation of the Lyapunov spectra. Before calculating the spectra of the 10-box system, the exponents of the Lorenz model are calculated first to test the method, and are found to agree with the published values. Positive exponents are found for certain parameter choices of the 10-box model (see table 3.3). For the 10-box model, the annual cycle variables Θ_{12} and Θ_{13} each contribute a Lyapunov exponent which is exactly zero. Since only Θ_{12} affects influences the other coordinates while Θ_{13} is only present to ensure oscillation, the latter coordinate is not taken into account when calculating the Lyapunov dimension. The pair can be thought of as a single complex number with a fixed absolute value and time-varying argument (indeed for the n-box

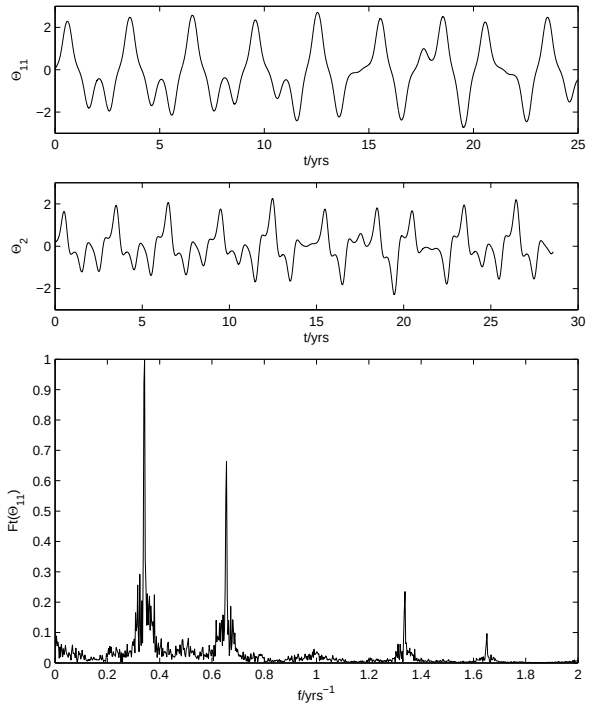

Figure 3.15: 10-box thermocline and SST timeseries with frequency spectrum (Fourier transform) for $(\kappa_0, R_E, R_W) = (7/6, 0.41, 0.88)$ and $\kappa_a = \kappa_0$.

model only the argument is integrated, explained later), thus only contributing one degree of freedom to the system. There are several paired exponents for both 10-box models, and these arise due to the presence of complex modes within the system, and these are found explicitly in chapter five. Exponents were calculated for more than one set of parameters for this system to check that both limit cycle (10-box 1) and chaotic solutions (10-box 2) resulted in Lyapunov spectra consistent with timeseries data. Since there are at this stage over a hundred ODEs being solved at once with reorthonormalisation in a ten dimensional space, it would not be computationally practical to calculate the spectra of systems with arbitrarily large phase spaces such as those which will be introduced over the next sections.

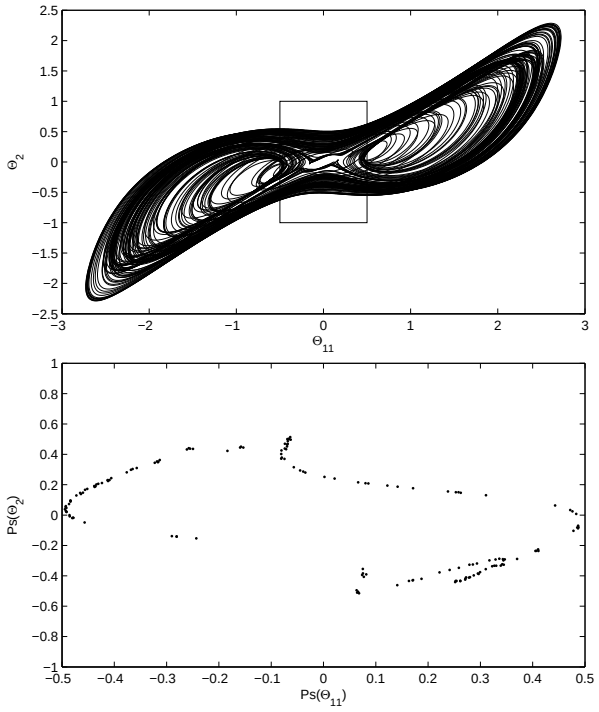

Figure 3.16: 10-box phase plot (top) and Poincaré section (bottom) for $(\kappa_0, R_E, R_W) = (7/6, 0.41, 0.88)$.

3.4 The n-box model

The configuration of the 10-box model is the foundation of the generalised n-box model, which has an arbitrarily fine ocean forced by a coarse atmosphere. Driven by two temperature coordinates, the n-box model is the first to introduce spatially varying SST, leading to a more complex atmospheric parametrisation. Six boxes in each strip (the same boxes from the 10-box system) are each discretised further into B boxes so that the total number of boxes is $12B - 2$, where the subtraction of two comes from the reflective boundary conditions. This allows for the resolution of any scale with no further alterations to the equations, provided the number of boxes is valid (i.e. $(n + 2)$ is a multiple of 12) and the Courant Friedrichs Lewy condition is satisfied. A visual representation of this model can be seen in 3.17, where the top row corresponds to the northern strip

Table 3.3: Lyapunov Spectra for Lorenz and 10-box systems, where $\times$ 2 indicates an identical pair of exponents.

Model	Parameters	Exponents	Dimension
Lorenz	$(\sigma, r, b) = (16, 45.92, 4)$	2.18	2.07
		0.02	
		-32.4	
10-box 1	$(\kappa_0, R_E, R_W) = (7/6, 0.41, 0.88)$	0.094	2.43
		-0.22	
		-0.58	
		-0.96	
		-1.66 $\times$ 2	
		-3.63 $\times$ 2	
		-5.10 $\times$ 2	
		-8.50	
10-box 2	$(\kappa_0, R_E, R_W) = (4/6, 0.10, 0.95)$	-0.17 $\times$ 2	1.0
		-0.80	
		-1.17	
		-1.58 $\times$ 2	
		-1.66 $\times$ 2	
		-3.66 $\times$ 2	
		-4.92 $\times$ 2	
		-5.88	

thermocline and the bottom row the equatorial strip, quantities within loops affect SST coordinates and their coupling to an atmospheric forcing is denoted by an arrow, and the forced regions are marked with a dot. In the equatorial strip, the thermocline h_e is contained within Θ_i coordinates with $1 < i < n/2$, and they evolve according to

$$\frac{d}{dt}(\Theta_i - \Theta_i^{\uparrow}) = \epsilon(\Theta_i^{\leftarrow} - \Theta_i) + \frac{1}{\Delta}(\Theta_i^{\leftarrow} - \Theta_i) + F_i, \tag{3.106}$$

with

$$F_i = \begin{cases} (\kappa_0 + \kappa_a \Theta_{n+3})\Theta_{n+1} & \text{if } 2B+1 \le i \le 3B; \\ (\kappa_0 + \kappa_a \Theta_{n+3})\Theta_{n+2} & \text{if } 3B+1 \le i \le 4B; \\ 0 & \text{otherwise.} \end{cases} \tag{3.107}$$

For the northern strip h_n, contained within coordinates Θ_i, $n/2 + 1 < i < n$,

$$\frac{d\Theta_i}{dt} = \epsilon\Theta_i + \frac{r_s}{\Delta}(\Theta_i - \Theta_i^{\rightarrow}) + G_i, \tag{3.108}$$

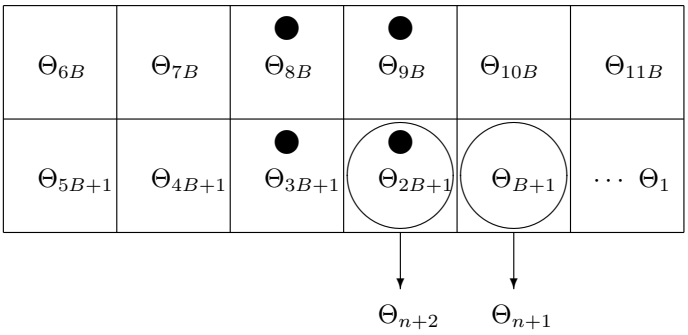

Figure 3.17: n-box diagram, as with the 10-box but with the first of B coordinates shown in each box. SST is averaged over two boxes of the coarse grid and each forces a group of B thermocline coordinates in the central Pacific.

and

$$G_i = \begin{cases} r_f(\kappa_0 + \kappa_a \Theta_{n+3})\Theta_{n+1} & \text{if } 9B \le i \le 10B - 1; \\ r_f(\kappa_0 + \kappa_a \Theta_{n+3})\Theta_{n+2} & \text{if } 8B \le i \le 9B - 1; \\ 0 & \text{otherwise.} \end{cases} \tag{3.109}$$

where $\Theta_{n+1} = T_{e1}$, $\Theta_{n+2} = T_{e1}$. The last two coordinates, like the 10-box model, evolve according to

$$\frac{d\Theta_{n+3}}{dt} = -\omega\Theta_{n+4} \tag{3.110}$$

$$\frac{d\Theta_{n+4}}{dt} = \omega\Theta_{n+3}. \tag{3.111}$$

During integration for this model, a different notation is used for convenience, and Θ_{n+3} is written $\cos(\phi)$ where ϕ is periodic in $[0, 2\pi]$. The equation

$$\frac{d\phi}{dt} = \omega \tag{3.112}$$

is integrated with instead of the mathematically equivalent $(\Theta_{n+3}, \Theta_{n+4})$ subsystem described previously. Defining annual phase as ϕ will also be used later

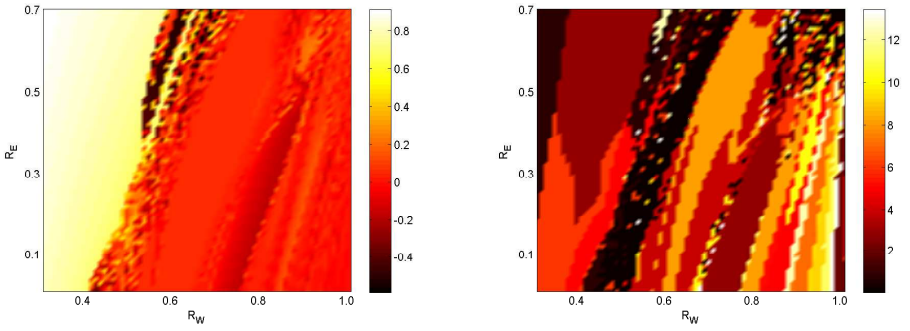

Figure 3.18: Mean of Θ_{100} (left) and period (right, in years) for the n^*-box with $\kappa_0 = \kappa_a = 7/5$.

when looking at Poincaré sections. Boundary conditions are

$$\Theta_1^{\uparrow} = R_E \Theta_1 \quad \Theta_{6B}^{\leftarrow} = R_W \Theta_{6B-1}, \tag{3.113}$$

where Θ_{6B-1} is the last thermocline coordinate in the equatorial strip.

Two eastern equatorial SST boxes feed back into the system as T_{e1} (in this case Θ_{95})

$$\frac{d}{dt}\Theta_{n+1} = \alpha\Theta_{n+1} + \frac{1}{B}\sum_{k=1}^{B}\tanh(\Theta_{k+B}), \tag{3.114}$$

and T_{e2} (or Θ_{96})

$$\frac{d}{dt}\Theta_{n+2} = [\alpha + \sigma(\kappa_0 + \kappa_a\Theta_{n+3})]\Theta_{n+2} + \frac{1}{B}\sum_{k=1}^{B}\tanh(\Theta_{k+2B}). \tag{3.115}$$

feed back into the system as blocks of forcing, B subgrid points wide. The number of boxes required for an accurate resolution of spatial thermocline features should be $\simeq 100$, making the mapping of three dimensional parameter space an expensive numerical task. For this reason the n-box (all examples show the case $n = 94$ and $B = 8$) and the n^*-box, discussed shortly, are mapped out for a fixed coupling strength. Like the 10-box, the n-box exhibits parametric instability for strong ocean-atmosphere coupling and this can be seen in figure 3.18. While the n-box model is not as complete as the next and final covered

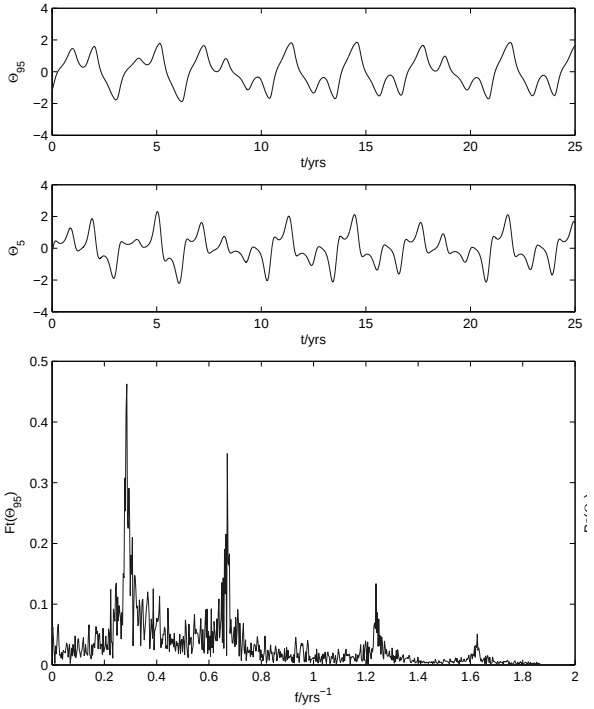

Figure 3.19: n-box (n=94) thermocline and SST timeseries and spectrum (Fourier transform) for $(\kappa_0, R_E, R_W) = (3/2, 0.26, 0.39)$, $\kappa_a = \kappa_0$.

in the thesis, due to its coarse atmospheric parametrisation, it will be the main subject of the initialisation experiments in later chapters.

3.4.1 Analysis of Timeseries

As the models become more complex, the exploration of parameter space will focus on locating ENSO-like regimes in the hope of finding a model suitable for testing initialisation schemes in chapter five. Only chaotic solutions to the n-box equations are considered, which fall under two categories depending on the nature of the parameters: those which are strongly (for example figures 3.19 and 3.20) and weakly (figure 3.4.1 and 3.22) phase locked to the seasonal cycle. Ideally, the test model would lie somewhere between these two cases. Strongly phase locked ($\kappa_a = \kappa_0$) models have roughly the same amplitude and period as ENSO, but the spectral peaks are thin and oscillations too regular. Weakly

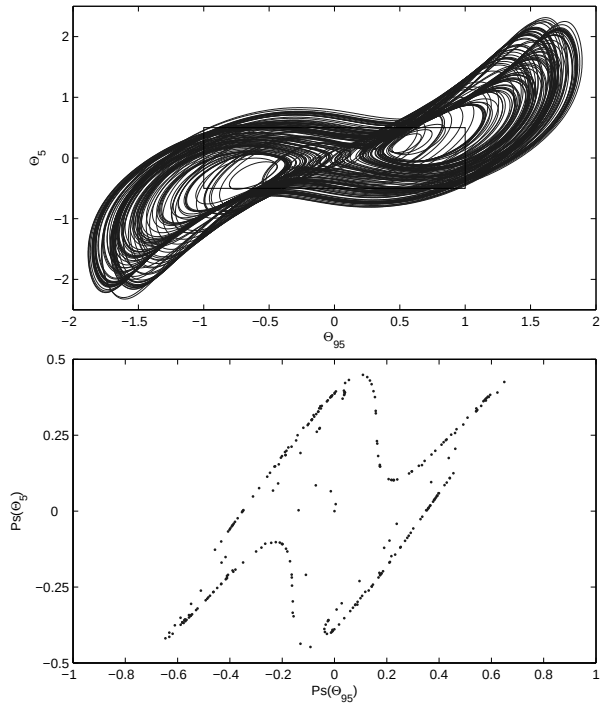

Figure 3.20: n-box (n=94) phase plot (top) and Poincaré section (bottom) for $(\kappa_0, R_E, R_W) = (3/2, 0.26, 0.39)$.

phase locked ($\kappa_a = \kappa_0/4$) models are more sporadic with broad spectral peaks, but the amplitudes are slightly higher than observed in reality and the periods are longer (3.4.1 shows a spectral peak indicating a period of approximately 5 years). For the weakly phase locked model, Poincaré sections were taken at a phase resolution of $\pi/6$ giving some insight into the chaos generating mechanism of this model. If the direction of increasing ϕ is tangent to the flow (contributing a zero Lyapunov exponent), it is useful to think of the Poincaré section in the $(\Theta_5, \Theta_{95}) = (h_e(4/5, t), T_{e1})$ plane as a cross section of a three dimensional object in $(\Theta_5, \Theta_{95}, \phi)$ space. For the phases $\phi \in [0, \pi]$ orbits are constrained to a strip (see figure 3.23), implying volume elements are flattening in the same manner as in the Lorenz or Rössler systems, so there is at least one negative Lyapunov exponent. In the complimentary phases $\phi \in [\pi, 2\pi]$ the strip stretches out and folds in on itself (see figure 3.24, particularly the last two sections

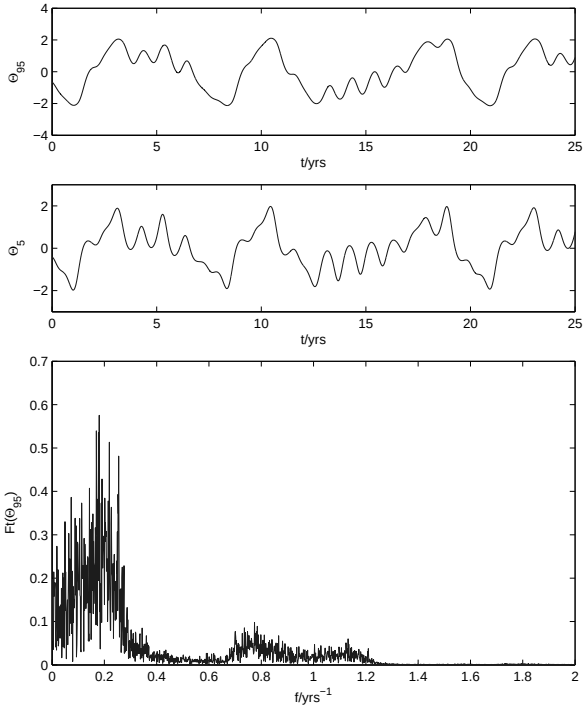

Figure 3.21: n-box (n=94) thermocline and SST timeseries and spectrum (Fourier transform) for $(\kappa_0, R_E, R_W) = (13/8, 0.47, 0.65)$, and $\kappa_a = \kappa_0/4$.

$\phi = [10\pi/6, 11\pi/6]$). An extension of the strip to nearly twice its length could be an indication of a positive Lyapunov exponent. Through this mechanism, if a segment of the curve (the intersection of a plane of constant ϕ with the attractor in the $(\Theta_5, \Theta_{95}, \phi)$ space) corresponds to an initial error, this will be stretched out over time until it covers the entire attractor, and at this stage predictability is lost. While there is no qualitative proof, some evidence presented here would imply that, for some parameter choices, the 94-box model loses predictability in the same way as low order chaotic systems.

3.5 The n^*-box model

At the top of the hierarchy of ENSO models covered by this thesis is the n^*-box model, with a fine ocean as well as a fine atmospheric parametrisation.

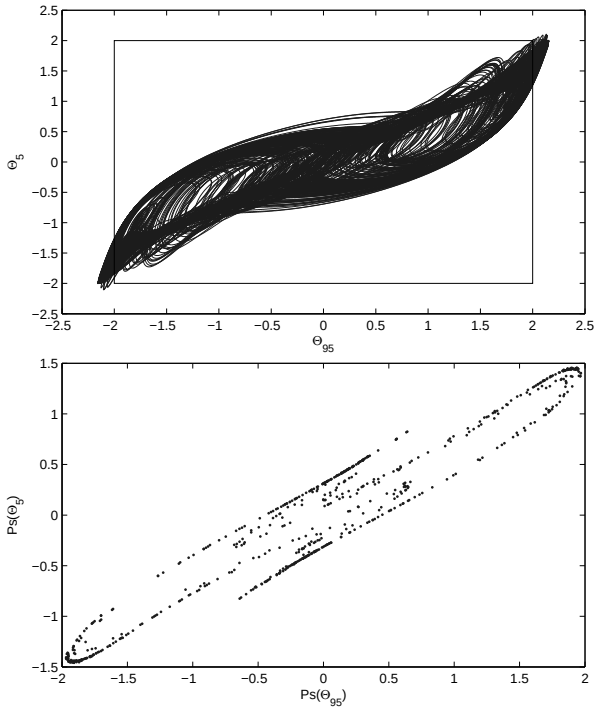

Figure 3.22: n-box (n=94) phase plot (top) and Poincaré section (bottom) for $(\kappa_0, R_E, R_W) = (13/8, 0.47, 0.65)$, and $\kappa_a = \kappa_0/4$.

This is a variation of the n-box model, implementing the spatially varying wind stress which requires an extension of $2B = (n+2)/6$ (i.e. $n^* = n + 2B$,) beyond the thermocline and annual phase space to incorporate extra fine-scale SST coordinates. These coordinates interact with the atmosphere and force the ocean, as shown in 3.25 with the same diagrammatic notation as the n-box, evolving as

$$\frac{d}{dt}\left(\Theta_{n+i} - \gamma\Theta_{B+i}\right) = \alpha\Theta_{n+i} + \sigma F_{B+i} + \tanh(\Theta_{B+i}), \tag{3.116}$$

for $1 \leq i \leq 2B$. For $n = 94$ (i.e. $B = 8$), $n^* = 110$ and there are 16 fine-scale SST coordinates. Thermocline evolution equations are the same as the n-box,

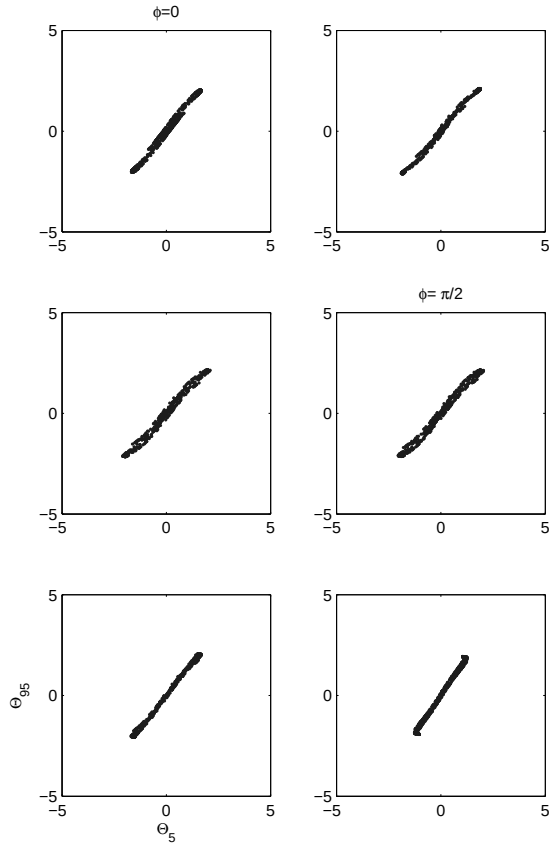

Figure 3.23: Poincaré section of the n-box model (n=94, $(\kappa_0, R_E, R_W) = (13/8, 0.47, 0.65)$) in the (Θ_5, Θ_{95}) plane as a function of phase ϕ taking the values $\in [0, \pi]$ at regular intervals of $\pi/6$.

although with a slight alteration to the forcing terms

$$F_i = \begin{cases} (\kappa_0 + \kappa_a \Theta_{n+2B+1})\Theta_{n+i} & \text{if } 2B+1 \leq i \leq 4B; \\ 0 & \text{otherwise.} \end{cases} , \tag{3.117}$$

and in the northern strip, this runs backwards due to the differencing scheme used

$$G_i = \begin{cases} (\kappa_0 + \kappa_a \Theta_{n+2B+1})\Theta_{n+2B-i} & \text{if } 8B \leq i \leq 10B-1; \\ 0 & \text{otherwise.} \end{cases} \tag{3.118}$$

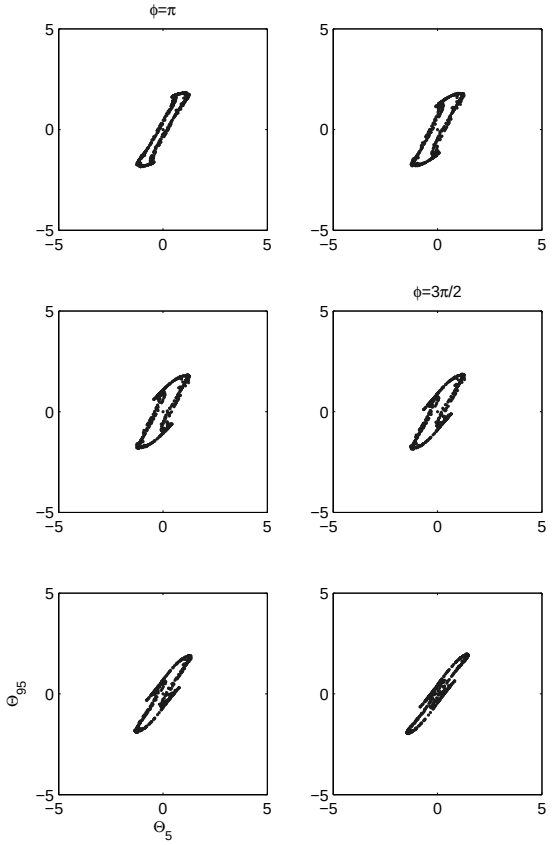

Figure 3.24: Poincaré section of the n-box model (n=94, $(\kappa_0, R_E, R_W) = (13/8, 0.47, 0.65)$) in the (Θ_5, Θ_{95}) plane as a function of phase ϕ taking the values$\in [\pi, 2\pi]$ at regular intervals of $\pi/6$.

and finally the annual cycle is contained within the subsystem

$$\frac{d\Theta_{n^*+1}}{dt} = -\omega\Theta_{n^*+2}, \tag{3.119}$$

$$\frac{d\Theta_{n^*+2}}{dt} = \omega\Theta_{n^*+1}, \tag{3.120}$$

Timeseries statistics were gathered for varying (R_E, R_W) and fixed κ_0, and the detailed structures seen in figure 3.26 would suggest that this model has the most sensitive parameter dependence of all the hierarchy. Figure 3.27 shows

Table 3.4: n-box Parameters

Parameter	Physical Interpretation	Value (M_1/M_2)
ϵ	Weak ocean adjustment damping	0.03
α	SST damping rate	-0.43
γ	Thermocline motion SST factor	0.19/0
κ_0	Ocean/Atmosphere Coupling mean strength	13/3/9/3
κ_a	Ocean/Atmosphere Coupling amplitude	$k_0/4/k_0$
R_E	Eastern boundary reflection coefficient	[0,1]
R_W	Western boundary reflection coefficient	[0,1]
r_s	Ratio of Rossby/Kelvin wave speeds	-0.25
r_f	Ration of atmospheric forcing of Rossby/Kelvin waves	-0.25
σ	Shear influence on SST	0.25

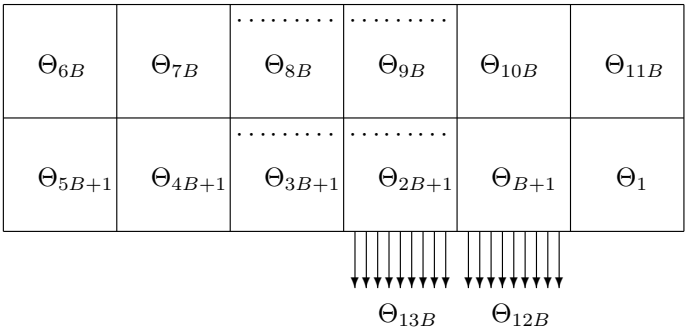

Figure 3.25: n^*-box diagram, where the $2B$ arrows represent SST coordinates forcing $2B$ thermocline coordinates in the equatorial and northern strips at a distance $x_c = B\Delta$ to the left.

an ENSO-like solution of the n^*-box, which is highly irregular and apparently asymmetric. Due to the symmetry of the equations, this is most likely due to the presence of a separatrix in the phase space, and this way different initial conditions would result in the mirror image of the attractor depicted in 3.28 over the page. While the amplitude and frequency of occurrence do not reflect observation, there are sporadic extreme events similar to those seen in for example figure 1.3 in the first chapter. From the Poincaré section it is difficult to determine whether the chaos generating mechanism is similar to that of the n-box, as cross sections in the $(\Theta_5, \Theta_{95}, \phi)$ space for fixed values of ϕ do appear to be constrained to a one dimensional region, but spread across the (Θ_5, Θ_{95}) plane, occasionally clustering (see figure 3.28).

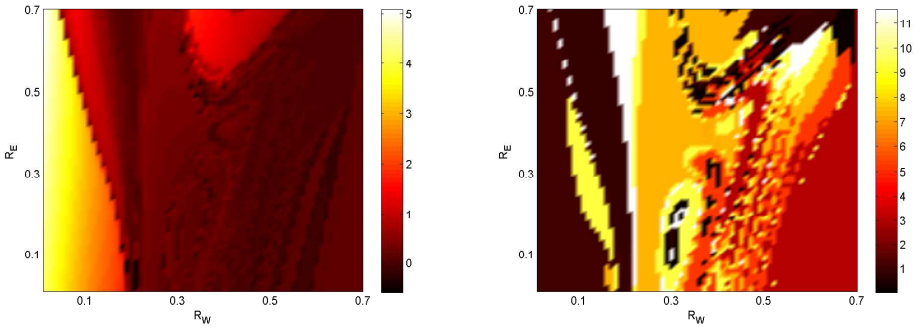

Figure 3.26: Mean of fine scale SST coordinate Θ_{100} (left) and period (right, in years) for the n^*-box with $\kappa_0 = \kappa_a = 7/5$.

3.6 Summary

A hierarchy of models has been developed from the 2-strip system of wave modes on the equatorial thermocline and a nonlinear sea surface temperature parametrisation. Beginning with a basic east/west finite difference truncation of the model equations, a conceptual model in R^2 was found to possess limit cycle solutions with a similar period and amplitude to the observed ENSO. A linear analytical approximation was made to the model equations which compared well to the nonlinear numerical solutions. Resolution of the finite difference truncation was increased, resulting in a 10-box model which also incorporated the annual cycle. This system was proven to have chaotic solutions by tracing the evolution of a set of basis vectors in the tangent space, finding positive Lyapunov exponents. A statistical map of the model space showed that it is parametrically unstable and was used to find ENSO-like solutions. The 10-box was used as a foundation to develop two general models which could resolve arbitrarily small scales, the n-box with a coarse atmospheric parametrisation similar to that of the 10-box, and the n^*-box with a fine parametrisation taking more advantage of the extra degrees of freedom released with the small scales. The chaos-generating mechanism which brought unpredictability to the n-box was described briefly and a map of the parameter space was made for fixed coupling values of both the n-box and n^*-box. ENSO-like regimes were found

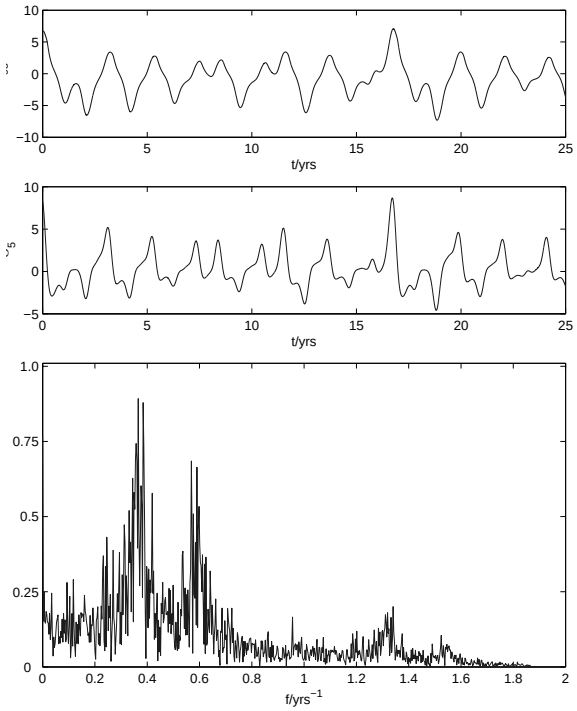

Figure 3.27: n^*-box (n^*=110) thermocline and SST timeseries, $(\kappa_0, R_E, R_W) = (11/5, 0.24, 0.73)$, and $\kappa_a = \kappa_0$.

in both models, and while it is most likely that the n^*-box is less predictable and more sensitive to initial conditions, the initialisation schemes discussed in the next chapter will be performed on the n-box model due to technical problems which will be made clear in chapter five.

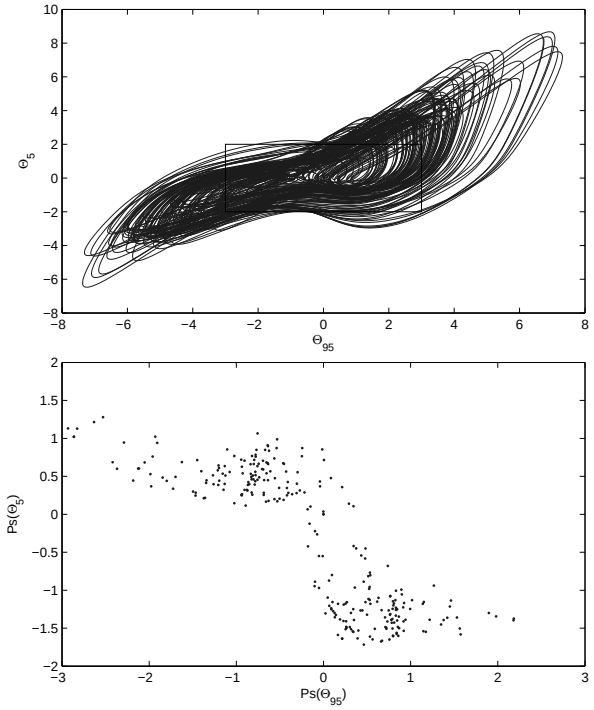

Figure 3.28: n^*-box (n^*=110) phase plot (top), Poincaré section (bottom) for $(\kappa_0, R_E, R_W) = (11/5, 0.24, 0.73)$, and $\kappa_a = \kappa_0$.

Chapter 4

Initialisation I: Methods

Positive Lyapunov exponents leading to the divergence of initially close orbits severely hinder forecasting predictability, since the slightest error in the measurement of an initial state can grow in time, sending even a perfect simulator of reality off into the wrong region of phase space. These divergences are often a result of erroneous observational data or effects due to subgrid scale turbulence causing the model to deviate from observation. In fact, data from the real world is typically riddled with noise from the sporadic nature of weather systems, making initialisation an essential bridge from stochastic physical reality to the deterministic model environment. The following chapter will be dedicated to describing several techniques, although not all of them will be implemented. These techniques fall under one of two classes; those linear schemes which seek to filter out fast processes entirely, or nonlinear schemes which include fast processes as functions of the slow ones.

This study will adopt two different approaches from the brief compendium of schemes. The first method is empirical and linear, and the model equations are restricted to a manifold of maximum variance; a linear subspace of the full model where trajectories have visited based on a large enough dataset. It is effectively an n-dimensional generalisation of the least squares fit algorithm. The second method is a truncation of the model equations such that there is a

small number of slow modes with the dominant behaviour, and the remaining fast modes are functions of these dominant modes. The dominant slow modes are hypothesised to live in a nonlinear finite dimensional subspace of the full infinite dimension phase space known as the inertial manifold, and this study employs a non-rigorous scheme to approximate the manifold in the finite, albeit large, dimensional case. Before discussing projection onto these manifolds, it is worth mentioning some ways in which error is simulated in order to test model predictability.

4.1 Perturbation

One way to determine the predictability of an n dimensional dynamical system is to probe the local space around an initial state on the attractor, so the interest is not the entire phase space but the tangent space of this state as time progresses. A set of randomly perturbed, and therefore imbalanced initial states is then represented by a set of vectors in this tangent space. In practice, randomly choosing these vectors from a potentially vast tangent space is typically not the most effective way to measure the robustness of a model. In meteorology for example, an SST perturbation which fluctuates wildly on small scales but averages out to zero on large scales may be less likely to induce a large scale atmospheric response than an extended spatial feature. It is important to seek out the directions in this tangent space which have long term consequences for the orbits which have been perturbed in this way. There exist several methods to determine these directions, or modes, which will be discussed but not implemented in this model; specific perturbations used for this model will be described in the final chapter.

4.1.1 Lyapunov Vectors

Lyapunov vectors spring naturally from the Osedelec multiplicative ergodic theorem[68], which allowed for accurate computations of Lyapunov exponents

for the first time. Ergodic theories typically involve measuring statistical properties of dynamical systems, and this one concerns the time averaged behaviour showing that a Lyapunov spectrum can be found which is irrespective of starting position on the phase space. The theorem states that, except in some rare cases, given a dynamical system (1.6) in $\mathbb{R}^n$, for every vector $\mathbf{x}$ there is a local decomposition of the phase space into a direct sum (i.e. a sum of basis vectors in the tangent space of $\mathbf{x}$) of $k \leq n$ subspaces

$$\mathbb{R}^n = \bigoplus_{i=1}^{k} H_i(\mathbf{x}),$$

corresponding to a set of n Lyapunov exponents

$$\lambda_i(\mathbf{x}) < \cdots < \lambda_k(\mathbf{x}) \tag{4.1}$$

determined by

$$\pm\lambda_i = \lim_{t\to\pm\infty} \frac{1}{|t-t_0|} \log\left(\frac{|S(t-t_0)\mathbf{e}|}{|\mathbf{e}|}\right), \tag{4.2}$$

where

$$\mathbf{e} \in H_i(\mathbf{x}). \tag{4.3}$$

The solution operator $S(t-t_0)$ is the cocycle, or product of Jacobians of $\mathbf{f}(\mathbf{x}(t))$ over the range $[t_0, t]$.

$$S(t-t_0) = J[\mathbf{f}(\mathbf{x}(t))] \cdots J[\mathbf{f}(\mathbf{x}(t_0))], \tag{4.4}$$

and the exponents are invariant under the action of these operators. By identifying subspaces corresponding to positive values of λ_i, the source of error growth can be allocated in a model. Similarly, negative λ_i correspond to directions of growth while the direction of flow is the H_i where $\lambda_i = 0$. to decay and zero to the direction of flow. Also, there exists a limit operator

$$L = \lim_{t\to\infty} \left(S^T(t-t_0)S(t-t_0)\right)^{\frac{1}{2t}}, \tag{4.5}$$

where superscript T denotes transpose. The eigenvalues of L are the squares of the exponentials of the Lyapunov exponents, while the eigenvectors are known as Lyapunov vectors.

4.1.2 Bred Vectors

Leading on directly from Lyapunov vectors are their computationally practical counterparts, finite time Lyapunov vectors or bred vectors[70]. These are calculated by randomly perturbing some initial state $\mathbf{x}_0$ by an amount $\delta\mathbf{x}_0$. Integrating forward the perturbed and unperturbed states gives

$$S(t)(\mathbf{x}_0 + \delta\mathbf{x}_0) = \mathbf{x}(t) + \delta\mathbf{x}(t). \tag{4.6}$$

The new perturbation $\delta\mathbf{x}(t)$ is rescaled by a factor ρ so that

$$\rho|\delta\mathbf{x}(t)| = |\delta\mathbf{x}_0|. \tag{4.7}$$

The rescaled grown perturbation $\rho\delta x(t)$ is then added to the unperturbed run $x(t)$ and again integrated

$$S(t)(\mathbf{x}(t) + \rho\delta x(t)) = \mathbf{x}(2t) + \rho\delta\mathbf{x}(2t), \tag{4.8}$$

and so on, and the perturbation $\delta\mathbf{x}(t)$ will then tend toward the direction of the fastest growing perturbation as $t \to \infty$. Bred vectors are useful in probing the sensitivities of a model, and empirically finding the unstable directions in a particular vicinity of its phase space.

4.1.3 Singular Vectors

Another useful product of the Osedelec theorem is the singular vector, a linear tangent model approach to growing vectors [69]. Consider the general evolution equation

$$\frac{d\mathbf{x}}{dt} = \mathbf{f}(\mathbf{x}), \tag{4.9}$$

or

$$\mathbf{x}(t) = S(t)\mathbf{x}(0). \tag{4.10}$$

Bridging the gap between the former expression and the latter involves the calculation of the Jacobian J of $\mathbf{f}$ at the point $\mathbf{x}$, since in the vicinity of $\mathbf{x}$

$$\frac{d\mathbf{x}}{dt} = J(x)\mathbf{x}. \tag{4.11}$$

The instantaneous solution operator, or propagator, is then

$$S_L(t) = e^{Jt}. \tag{4.12}$$

This defines a linear tangent model which is valid while the trajectories are close to $\mathbf{x}$. An initial perturbation $\delta\mathbf{x}_0$ will grow as

$$\delta\mathbf{x}(t) = S_L(t)\delta\mathbf{x}_0, \tag{4.13}$$

and the relative size is then

$$\frac{|\delta\mathbf{x}(t)|}{|\delta\mathbf{x}_0|} = \frac{\sqrt{(\delta\mathbf{x}_0 e^{J^*t}, e^{Jt}\delta\mathbf{x}_0)}}{|\delta\mathbf{x}_0|}. \tag{4.14}$$

Unlike the example given in the introduction, there is rarely a neat way of expressing $S(t)$ analytically. If the sphere of states around the point $\mathbf{x}$ is transformed into an ellipse by the action of S, its axes will expand or contract with the flow. Of interest is the direction of most rapid expansion, which is the eigenvector corresponding to the largest eigenvalue of $S^T S$. This method is closely related to the singular value decomposition described later.

4.2 Linear Methods

4.2.1 Exponential Time Differencing

While this scheme is not reductive, in that it does not involve integrating quantities which have been projected onto a lower dimensional subspace of the full state space, it does introduce some concepts which will be intuitively useful later on such as the distinction between fast and slow modes. Consider a system

$$\frac{d\hat{\mathbf{x}}}{dt} = \mathbf{f}(\mathbf{x}), \tag{4.15}$$

which satisfies $\mathbf{f}(\mathbf{x}^*) = 0$ for a point or set of fixed points $\mathbf{x}^*$. Linear dynamics governed by

$$\frac{d\hat{\mathbf{x}}}{dt} = \Lambda\hat{\mathbf{x}}, \tag{4.16}$$

with solution

$$\hat{\mathbf{x}}(t) = e^{\Lambda t}\hat{x}_0, \tag{4.17}$$

correspond to fast oscillations which are enveloped by slow, nonlinear behaviour $\mathbf{N}(\mathbf{x})$. A convenient change of basis involves scaling by an integrating factor

$$\chi = e^{-\Lambda t}\mathbf{x}, \tag{4.18}$$

so that

$$\frac{d\chi}{dt} = e^{-\Lambda t}\left(\frac{d\mathbf{x}}{dt} - \Lambda\mathbf{x}\right). \tag{4.19}$$

Now, notice that rearranging and multiplying through (4.26) with $e^{-\Lambda t}$ gives

$$e^{-\Lambda t}\left(\frac{d\mathbf{x}}{dt} - \Lambda\mathbf{x}\right) = e^{-\Lambda t}\mathbf{N}(\mathbf{x}), \tag{4.20}$$

which is in fact another way of writing

$$\frac{d\chi}{dt} = e^{-\Lambda t}\mathbf{N}(e^{\Lambda t}\chi). \tag{4.21}$$

Only the nonlinear part is integrated and the linear oscillations are contained within it, allowing for the Courant Friedrichs Lewy condition to be bypassed, provided $\mathbf{N}(\mathbf{x}(\mathbf{t}))$ is indeed slowly varying. This idea is analogous to the concept of a wave envelope, with fast waves moving at phase speed while the amplitude modulated signal moves at a slow group velocity. Originally this scheme was proposed as a means to minimise error growth in the ENSO box models considered in this thesis, but it was found that in some cases nonlinearity was large and thus fast and slow motion could not be separated simply in terms of linear and nonlinear modes, so instead the focus moved to model reduction methods for the initialisation experiments.

4.2.2 Galerkin Truncation

Any process involving the reduction of PDEs to a finite set of ODEs involves a truncation of some type of normal mode, as a computer is incapable of dealing with the infinities involved in a continuum. A PDE is first decomposed into orthogonal basis functions, typically with the low (high) order modes resolving large (small) scale structures. The time evolution of the state vector $\mathbf{x}$ whose elements are basis functions can be written

$$\frac{d\mathbf{x}}{dt} = L\mathbf{x} + \mathbf{N}(\mathbf{x}), \tag{4.22}$$

where the linear part $L = J(\mathbf{x}^*)$ is the Jacobian of $\mathbf{x}^*$, and $\mathbf{N}$ is a vector function of the state vector; the nonlinear part. Typically $\mathbf{x}^*$ is a fixed point of the system, and a good choice of fixed point is one which best represents some kind of mean state, or has a particular symmetry. In most cases L will be similar to a matrix which has nonzero entries in the diagonal elements only, so there exists a matrix V such that

$$L = V\Lambda V^{-1}. \tag{4.23}$$

The n nonzero elements of Λ are its eigenvalues of L and the n columns of V are its eigenvectors. If

$$\mathbf{x} = V\chi, \tag{4.24}$$

multiplying through (4.22) by V^{-1} yields

$$\frac{d\chi}{dt} = \Lambda\chi + \eta(\chi), \tag{4.25}$$

where $\eta = V^{-1}\mathbf{N}(V\chi)$ which is the PDE rewritten in terms of its normal modes. One way to think of the normal mode of a nonlinear system is a way of defining some kind of collective motion, representing the dynamics of a structure rather than an individual quantity. The concept of a Galerkin truncation is fairly simple: a projection operator $P_m : H \to \mathbb{R}^m$ such that m is minimised but at the same time best represents the full dynamics in H. Dimensions of χ which are outside the range of P_m correspond to those eigenvalues of L which are large and negative, which rapidly dissipate and do not affect the dynamics on long timescales. Operating on (4.26) with P_m gives

$$\frac{d\mathbf{p}}{dt} = \Lambda\mathbf{p} + P_m\eta(\mathbf{p}), \tag{4.26}$$

where $\mathbf{p} = P_m\chi$ and η is a function of reduced state vector $\mathbf{p}$. In cases of the n-box model for large enough n it is assumed that the model in $\mathbb{R}^n$ is a perfect representation of the mode in the full Hilbert space H. While being essential for the numerical modelling of any PDE, this scheme can also be seen as a filtering of high frequency modes via a projection from the full model in $\mathbb{R}^n$ onto a slow subspace $m < n$. However, there is a limit to how far this analogy can be taken when nonlinear terms come into play, and this shall be discussed in the later parts of this chapter.

4.2.3 Proper Orthogonal Decomposition

Expanding the set of initialisation tools beyond the model equations, and including the data generated by these equations allows for a powerful statistical technique for the approximation of attractors and reduction of models. Originally this came from a theory of Loeve concerning the decomposition of random functions into sums of orthogonal functions with random coefficients[71]. The first applications of this theory to the field of fluid mechanics were made by Lumley[72], as a means to extract features from turbulent flows. An overview of the subject can be found in Berkooz, Holmes and Lumley[73], while an introduction to the subject can be found in Chaterjee[74]. Consider a function h over the domain $x \in \Omega$. Now, the inner product of two functions h and g

$$(h, g) = \int_{\Omega} h(x)g(x)dx, \tag{4.27}$$

and the norm is

$$|h| = \sqrt{(h, h)}. \tag{4.28}$$

Say that h is allowed to vary indefinitely with time, then the average

$$\langle h \rangle = \lim_{t\to\infty} \frac{1}{t} \int_0^t h(x, t)dt. \tag{4.29}$$

Extraction of features from the function space involves finding a function ϕ such that the variance in the direction ϕ,

$$V = \frac{\left\langle |(h, \phi)|^2 \right\rangle}{(\phi, \phi)}, \tag{4.30}$$

is maximised. It is known that the function ϕ is in fact an eigenfunction of the average two point covariance tensor,

$$R(x, x^{'}) = \lim_{t\to\infty} \frac{1}{t} \int_0^t h(x, t)h(x^{'}, t)dt. \tag{4.31}$$

There is an infinite set of these functions, call them ϕ_k and they satisfy the orthonormality condition

$$(\phi_j, \phi_{j'}) = \delta_{kk'}, \tag{4.32}$$

each corresponding to an eigenvalue λ_k. Since $R(x, x^{'})$ is a symmetric tensor, the eigenvalues are all positive real numbers. The tensor can then be diagonalised into

$$R(x, x^{'}) = \sum \lambda_j \phi_j(x) \phi_j^*(x^{'}). \tag{4.33}$$

Eigenvalues are typically ordered in descending order, that is $\lambda_j > \lambda_{j+1}$, starting at a finite value but tailing off to zero as index j increases. The basis functions corresponding to the zero eigenvalues are largely irrelevant and do not affect the outcome of time integration if removed, so completeness of the basis allows the following decomposition

$$h(x) = \sum_{j}^{m} c_j \phi_j(x), \tag{4.34}$$

where m is the value of j for which $\lambda_{j+1} = 0$.

4.2.4 Singular Value Decomposition

Proper orthogonal decomposition (POD) leads naturally to the discussion of the singular value decomposition (SVD) of a matrix. This is an extremely useful method which involves expressing a matrix A in the form

$$A = U \Sigma V^T, \tag{4.35}$$

where the matrix Σ is a diagonal matrix whose entries are positive real numbers called the singular values of A. U and V are matrices satisfying $V^T V = 1$ and $UU^T = 1$, where the normal transpose is used as the assumption is made that they are not complex. These are not necessarily the same size, meaning Σ and indeed A need not be square in order for the SVD to be calculated. The columns of U form the eigenvectors of $A^T A$, and columns of V the eigenvectors of AA^T,

known as the proper orthogonal modes.

SVD methods in the context of timeseries are effectively an m dimensional generalisation of the least squares fit. Taking a sample of N state vectors $\mathbf{x}_i$ from a time series one can construct a matrix which is the discrete version of the correlation tensor $R(x, x^{'})$, or

$$R = \frac{1}{N} \sum_{i=1}^{N} \mathbf{x}_i \otimes \mathbf{x}_i, \tag{4.36}$$

where superscript T denotes transpose, the covariance matrix, and the operator $\otimes$ is the outer product of two vectors. The eigenvalues of R are related to the variance of the dataset, and in decreasing order their corresponding eigenvectors point in the direction of maximum to minimum variance. Since the covariance matrix is symmetric, the eigenvalues are all real and positive, while the eigenvectors are orthogonal. The eigenvalues give an upper bound on the dimensional size of the attractor, as they give the magnitudes of the principal axes of a family of n dimensional ellipsoids, where n is the size of the phase space. This family of ellipsoids defines curves of constant probability in the phase space. When a certain direction in the phase space is rarely explored by orbits, the probability is low and the ellipse is flattened in this direction. In this sense, an eigenvalue corresponding to an ellipse which has been flattened sufficiently can be assumed to be a negligible direction of the phase space (or one with a very low probability for finite values), which need not be integrated. Say that there are $n-m$ negligible directions, then the remaining m form a new basis spanning the linear subspace which is the phase space of the reduced model. Any system

$$\frac{d\mathbf{x}}{dt} = L\mathbf{x} + \mathbf{N}(\mathbf{x}), \tag{4.37}$$

can be expressed in terms of the principal components. Given a set of m principal vectors ϕ, $\mathbf{x}$ can be decomposed via the $m \times n$ matrix V as

$$\mathbf{x} = V\phi, \tag{4.38}$$

and since $V^T V = 1$, equation (4.37) describing an n dimensional system becomes a lower order m dimensional system

$$\frac{d\phi}{dt} = V^T L V\phi + V^T \mathbf{N}(V\phi) \tag{4.39}$$

through multiplication by the $m \times n$ transpose of V. Another useful property of the SVD is that it allows for the calculation of the pseudoinverse of A[75],

$$A^\dagger = V\Sigma^{-1}U^T, \tag{4.40}$$

a generalisation of the inverse for nonsquare matrices with the following properties

$$AA^\dagger A = A, \tag{4.41}$$

$$A^\dagger AA^\dagger = A^\dagger, \tag{4.42}$$

$$(AA^\dagger)^* = AA^\dagger, \tag{4.43}$$

$$(A^\dagger A)^* = A^\dagger A. \tag{4.44}$$

It can be used to solve linear systems of equations regardless of whether a unique solution exists, which shall be crucial for projecting onto the approximate inertial manifold which will now be explained.

4.3 Nonlinear Methods

4.3.1 The Baer-Tribbia Series

A well known initialisation scheme for projecting onto the slow manifold was developed by Baer and Tribbia[4]. It assumes the model equations contains a small parameter $\epsilon < 1$ such that (4.22) separates into a fast and slow evolving

part with

$$L = \begin{pmatrix} \epsilon\Lambda_x & 0 \\ 0 & \Lambda_y \end{pmatrix}, \tag{4.45}$$

$$\mathbf{N} = \epsilon \begin{pmatrix} \mathbf{N_x} \\ \mathbf{N_y} \end{pmatrix}, \tag{4.46}$$

and

$$\mathbf{x} = \begin{pmatrix} \mathbf{X} \\ \mathbf{Y} \end{pmatrix}, \tag{4.47}$$

so that

$$\frac{d\mathbf{X}}{dt} = \epsilon\Lambda_x\mathbf{X} + \epsilon\mathbf{N}_x(\mathbf{x}) \tag{4.48}$$

$$\frac{d\mathbf{Y}}{dt} = \Lambda_y\mathbf{Y} + \epsilon\mathbf{N}_y(\mathbf{x}), \tag{4.49}$$

where $\mathbf{X}$ and $\mathbf{Y}$ represent slow and fast components of $\mathbf{x}$ respectively. Here the equations have been written in their Jordan normal form, so Λ is diagonal. The vector $\mathbf{x}$ is then expanded into a power series in terms of ϵ

$$\mathbf{x} = \sum_{i=0}^{\infty} \mathbf{x_i}\epsilon^i, \tag{4.50}$$

and the time variable is split into fast $t^* = t$ and slow $\tau = \epsilon t$ timescales, so (4.48) reads

$$\frac{\partial\mathbf{X}}{\partial t^*} = \epsilon\left(\Lambda_x\mathbf{X} - \frac{\partial\mathbf{X}}{\partial\tau}\right) + \epsilon\mathbf{N}_x(\mathbf{x}), \tag{4.51}$$

$$\frac{\partial\mathbf{Y}}{\partial t^*} = \Lambda_y\mathbf{Y} - \epsilon\frac{\partial\mathbf{Y}}{\partial\tau} + \epsilon\mathbf{N}_y(\mathbf{x},). \tag{4.52}$$

By choosing the correct initial value of $\mathbf{Y}$ then, it should be possible to eradicate fast motion from the system altogether, that is $\mathbf{Y}$ is independent of

the fast time t^*. Taking these expressions to zero order in ϵ gives

$$\frac{\partial \mathbf{Y_0}}{\partial t^*} = \Lambda_y \mathbf{Y_0} \quad \tfrac{\partial \mathbf{X_0}}{\partial t^*} = 0. \tag{4.53}$$

and to first order

$$\frac{\partial \mathbf{X_1}}{\partial t^*} = \Lambda_x \mathbf{X_0} - \frac{\partial \mathbf{X_0}}{\partial \tau} + \mathbf{N}_x(\mathbf{x_0}), \tag{4.54}$$

$$\frac{\partial \mathbf{Y_1}}{\partial t^*} = \Lambda_y Y_1 + \mathbf{N}_y(\mathbf{x_0}). \tag{4.55}$$

From (4.53) the t^* independence of $\mathbf{X}_0$ is clear. For $\mathbf{Y}_0$ this can be attained by setting

$$\mathbf{Y}_0(0) = 0. \tag{4.56}$$

Removing t^* dependence from (4.53) results in

$$\frac{d\mathbf{X}_0}{d\tau} = \Lambda_x \mathbf{X_0} + \mathbf{N}_x(\mathbf{x_0}), \tag{4.57}$$

and

$$\mathbf{Y}_1 = \Lambda_y^{-1} \mathbf{N}_y(\mathbf{x_0}). \tag{4.58}$$

One potentially restrictive aspect of this scheme with regards to the aforementioned box models is the demand for a small parameter, ϵ, as it is not unusual for an n-box system to have nonlinear terms which outweigh the linear, for example due to the presence of limit cycles.

4.3.2 The Inertial Manifold

Although turbulence as it stands is still an incomplete theory, there have been some advances over the past few decades which may be of some practical use in climate prediction. One example comes from the combination of dynamical systems theory with functional analysis, giving rise to the theory of infinite dimensional dynamical systems[82][83]. This field of work is mainly concerned in proving that within the infinite dimensional phase space of certain PDEs there

exists a finite dimensional global attractor; an invariant set which attracts all orbits within the space. While it has been known for some time that flows in a Hilbert space have finite dimensional attractors[76], the earliest known example was proven by Mallet-Paret, whether or not turbulence is a finite dimensional phenomenon is still an open question. Attempts to answer this question within a rigorous mathematical framework led to the discovery of the inertial manifold, an invariant finite dimensional manifold which contains the global attractor and attracts all orbits exponentially in time[77]. These have been proven to exist for some PDEs, including the Kuramoto-Sivashinksky[78] and complex Ginsburg-Landau[79] equations. Connections between inertial manifold theory and weather prediction have already been established, and it has been shown that the slow manifold is a special case of inertial manifold[80]. Indeed, there are similarities between the Baer-Tribbia expansion and the inertial form which will be described shortly. Model reduction via the approximation of inertial manifolds for chaotic systems would seem a more natural choice than the approximation of the attractor itself, since this typically has a fractal structure for chaotic flow.

Proving the existence involves taking a Fourier decomposition of the PDEs, and showing that a condition known as the squeezing property holds[83]. It could be possible to check a modified version of this property for finite dimensional systems by looking at the difference between two solutions projected onto fast and slow subspaces, but the following discussion will refer to the infinite dimensional case. To achieve the squeezing one must separate the identity matrix I which operates on a Hilbert space H into finite P (the low modes) and infinite Q (the high modes) dimensional projectors

$$I = P_m + Q_m, \tag{4.59}$$

then, if $\mathbf{x}_1$ and $\mathbf{x}_2$ are two different trajectories on the attractor, either

$$|Q_m(S(t)\mathbf{x}_1 - S(t)\mathbf{x}_2)| \leq |P_m(S(t)\mathbf{x}_1 - S(t)\mathbf{x}_2)|, \tag{4.60}$$

with $S(t)$ the solution operator for some fixed time t, or else

$$|S(t)\mathbf{x}_1 - S(t)\mathbf{x}_2| \leq \delta|\mathbf{x}_1 - \mathbf{x}_2|. \tag{4.61}$$

where $0 < \delta < 1$. The projection index m is a function of δ such that reducing δ calls for an increase in the dimensionality of P_m. Thus, either low modes dominate the motion or solutions are tending toward the same asymptotic future. Now, letting $P_m\mathbf{x} = \mathbf{p}$ and $Q_m\mathbf{x} = \mathbf{q}$, this leads to the strong squeezing condition which states that either

$$|\mathbf{q}_1(0) - \mathbf{q}_2(0)| \leq L|\mathbf{p}_1(0) - \mathbf{p}_2(0)|, \tag{4.62}$$

implying

$$|\mathbf{q}_1(t) - \mathbf{q}_2(t)| \leq L|\mathbf{p}_1(t) - \mathbf{p}_2(t)|, \tag{4.63}$$

or

$$|\mathbf{q}_1(t) - \mathbf{q}_2(t)| \geq L|\mathbf{p}_1(t) - \mathbf{p}_2(t)|, \tag{4.64}$$

implying

$$|\mathbf{q}_1(t) - \mathbf{q}_2(t)| \leq |\mathbf{q}_1(t) - \mathbf{q}_2(t)|e^{-kt}, \tag{4.65}$$

where L, k are positive constants. Roughly speaking, this states that either a system is dominated by slow modes, and if not the fast modes dissipate over time. The first statement is more relevant here, since the interest is in asymptotic behaviour. These conditions guarantee the existence of a smooth mapping $\mathbf{\Phi}$ from $P_mH \to Q_mH$. That is, if q is a function $\mathbf{\Phi}(\mathbf{p})$ then

$$\frac{d\mathbf{\Phi}(\mathbf{p})}{dt} = \Lambda\mathbf{\Phi}(\mathbf{p}) + Q_m\eta(\mathbf{p} + \mathbf{\Phi}(\mathbf{p})), \tag{4.66}$$

where η is the nonlinear part of the system in terms of normal modes (see equation (4.26)). Integrating directly over all history to initial time $t_0 = 0$ gives

$$\mathbf{\Phi}(\mathbf{p}) = \int_{-\infty}^{0} \Lambda\mathbf{\Phi}(\mathbf{p}) + Q_m\eta(\mathbf{p} + \mathbf{\Phi}(\mathbf{p})). \tag{4.67}$$

The inertial manifold $\mathbf{\Phi}$ is then defined as the fixed point of the operator T where

$$T\mathbf{\Phi}(\mathbf{p}) = \int_{-\infty}^{0} e^{-\Lambda s} Q_m\eta\left(\mathbf{p} + \mathbf{\Phi}(\mathbf{p})\right) ds, \tag{4.68}$$

and the manifold can be evolved via numerical integration. Finding the inertial manifold is effectively finding the asymptotic slaving function of a dynamical system in a function space. Some analytical approximations can be made by considering the steady state solutions of $\mathbf{\Phi}$, where the right hand side of (4.66) is set to zero so that

$$\mathbf{\Phi} = -\Lambda^{-1} Q_m\eta(\mathbf{p} + \mathbf{\Phi}(\mathbf{p})). \tag{4.69}$$

Then be found by iterating

$$\mathbf{\Phi}_{N+1} = -\Lambda^{-1} Q_m\eta(\mathbf{p} + \mathbf{\Phi}_N), \tag{4.70}$$

with

$$\mathbf{\Phi_0} = 0, \tag{4.71}$$

$$\mathbf{\Phi_1} = -\Lambda^{-1} Q_m\eta(\mathbf{p}_0), \tag{4.72}$$

$$\mathbf{\Phi_2} = -\Lambda^{-1} Q_m\eta(\mathbf{p}_0 - \Lambda^{-1} Q_m\eta(\mathbf{p}_0)), \tag{4.73}$$

and so on. It is worth noting that, to first order, the inertial manifold has the same form as the first term in the Baer-Tribbia series, and Boyd has remarked these are two aspects of the same thing[85].

For practical purposes such as the numerical modelling of PDEs, the Hilbert space H is replaced by a finite dimensional phase space $\mathbb{R}^n$. In this case, the inertial manifold is replaced by convergent families of approximate inertial mani-

folds, which can be calculated as follows[81]. Starting with the system separated into linear and nonlinear parts

$$\frac{d\mathbf{x}}{dt} = L\mathbf{x} + \mathbf{N}(\mathbf{x}), \tag{4.74}$$

where this time each element of $\mathbf{x}$ corresponds to a Fourier coefficient of a PDE system, this system is transformed, as before, into normal modes

$$\frac{d\chi}{dt} = \Lambda\chi + V^{-1}\mathbf{N}(V\chi), \tag{4.75}$$

where Λ is a diagonal matrix of eigenvalues of L. The individual nonzero elements $\Lambda_{i,i}$ are arranged so that the element with the most positive real part comes first, and the following elements are in descending order according to $\Re(\Lambda_{i,i})$. If there are to be m low modes and therefore $n-m$ high modes, the $n \times n$ identity matrix is again separated into projectors

$$I = P_m + Q_m, \tag{4.76}$$

where P_m is effectively the identity with all diagonal elements $> m$ equal to zero. This time the range of the operator Q_m is finite dimensional. Since P_m and Q_m commute with Λ, the low and high resolution parts become

$$\begin{aligned} \frac{d\mathbf{p}}{dt} &= \Lambda\mathbf{p} + P_m V^{-1}\mathbf{N}(V(\mathbf{p}+\mathbf{q})), \\ \frac{d\mathbf{q}}{dt} &= \Lambda\mathbf{q} + Q_m V^{-1}\mathbf{N}(V(\mathbf{p}+\mathbf{q})), \end{aligned}$$

respectively. To find the approximate inertial manifold, the steady state solutions of $\mathbf{\Phi}(\mathbf{p}) = \mathbf{q}$ are

$$\frac{d\mathbf{q}}{dt} = 0, \tag{4.77}$$

so that $\mathbf{q}$ is a (nonlinear) function of $\mathbf{p}$ only

$$\mathbf{q} = -\Lambda^{-1}Q_m V^{-1}\mathbf{N}(V(\mathbf{p}+\mathbf{q})). \tag{4.78}$$

The main difference between the approximate inertial manifold method and the Galerkin truncation is that the m dimensional subset containing the attractor is allowed to have curvature based on the nonlinear part of the dynamical system. Now, using

$$\mathbf{\Phi}(\mathbf{p}) = -\Lambda^{-1} Q_m V^{-1} \mathbf{N}(V[\mathbf{p} + \Phi(\mathbf{p})]). \tag{4.79}$$

with initial guess

$$\mathbf{\Phi}_0 = 0, \tag{4.80}$$

the next iterate is

$$\mathbf{\Phi}_1 = -\Lambda^{-1} Q_m V^{-1} \mathbf{N}(V\mathbf{p}). \tag{4.81}$$

For the sake of computational efficiency, no further iterations are made and the modified $\mathbf{p}$ equation is

$$\frac{d\mathbf{p}}{dt} = \Lambda\mathbf{p} + V^{-1}\mathbf{N}(V[\mathbf{p} - \Lambda^{-1} Q_m V^{-1} \mathbf{N}(V\mathbf{p})]), \tag{4.82}$$

the inertial form of the model equations. Consequently, if it takes m determining modes to sufficiently approximate an attractor then the model in the n dimensional phase space has been reduced by $n - m$ dimensions.

It is important to point out that conventional computations of inertial manifolds employ a Fourier decomposition of the state vector, while this study employs a finite difference scheme. Inertial manifold theory has been applied to finite difference approximations to PDEs[84], but this study adopts a different, non-rigorous approach. Due to the nature of the eigenfunctions of L in the finite difference scheme, modes corresponding to more positive eigenvalues have a tendency to resolve large scale structures, while eigenfunctions which are more rapidly decaying resolve small scale spatial patterns. Hence, the former are chosen to represent the P modes and the latter the Q, so that the slow motion is associated with smooth eigenfunctions while the fast processes stem from small scale disturbances. Projection onto the slow manifold is then effectively a smoothing out of the initial conditions, while integrating on this

manifold is timestepping through regions of the phase space which are devoid of discontinuities. Potential hazards in employing this method as an initialisation scheme include the problem of orthogonality of the eigenfunctions, which is not guaranteed, and the difficulties in the inversion of L, should there exist parallel eigenfunctions or eigenvalue degeneracy.

Chapter 5

Initialisation II: Experiments

This chapter will use model reduction methods described in chapter four and apply them to some of the models discussed in chapter three. First the accuracy of the reduction schemes is tested, then numerical stability as timestep is increased. A parameter selection is chosen for one of the box models and data from this model is used to simulate observational data. For the experiments, this data is perturbed on multiple spatial scales and fed into the full model and its reduced versions as initial conditions. Predictability of these models is compared using statistical measures of how they deviate from simulated observation over a 12 month forecast.

5.1 Methodology

An idealised hierarchy of ENSO models has been developed, and from the complex end of the scale a model with behaviour similar to that observed in reality is chosen to represent a perfect simulator of the phenomenon. The n-box model with $n = 94$ is integrated forward in time until a balanced state is reached, which is used as the initial state in a longer integration to be stored as artificial

observational data. Two reduction schemes outlined in the last chapter, the approximate inertial manifold (the acronym AIM is used from now on, see 4.3.2) and singular value decomposition (acronym SVD, see 4.2.4), are then applied to the selected model resulting in a pair of low order models.

To generate initial perturbations which act on large and small spatial scales, a combination of 10-box and n-box basis functions are used. A random sum over all functions is weighted according to the basis used and combined to give an initial perturbation. Weights can be coarse for 10-box scale thermocline perturbations and SST variables, or fine for n-box scale thermocline perturbations, and the experiments described in this chapter show how varying these weights affects ensemble forecasts of the selected model. For the initialisation experiments, ensembles of randomly perturbed true states are fed into the full model and reduced models as erroneous initial states, and statistics of how these ensembles deviate from the true states provide a means to calculate error growth. Standard error magnitude is measured by examining differences between the perfect observation and forecasts made using perturbed initial data with the perfect model. If the growth of this error is reduced with forecasts made using perturbed initial data with the AIM or SVD models, there has been an improvement of predictability and it can be said that an improved initialisation has been performed. At this stage there is enough foundation work to proceed with the initialisation experiments which will form the main result of this study.

5.1.1 Parameter Selection

While it is unlikely that an n-box model (with n=94) will satisfy all the criteria of the observed ENSO, the pair M_1 at $(\kappa_0, R_E, R_W) = (13/4, 0.47, 0.65)$ with $\kappa_a = \kappa_0/4$, and M_2 at $(\kappa_0, R_E, R_W) = (3/2, 0.26, 0.39)$ with $\kappa_a = \kappa_0$, have many similar characteristics (see table 3.4 for full list of parameters used). M_1 (see figure 5.1) has the properties

- Fourier spectrum of SST time series indicates an oscillation period of greater than 4 years.

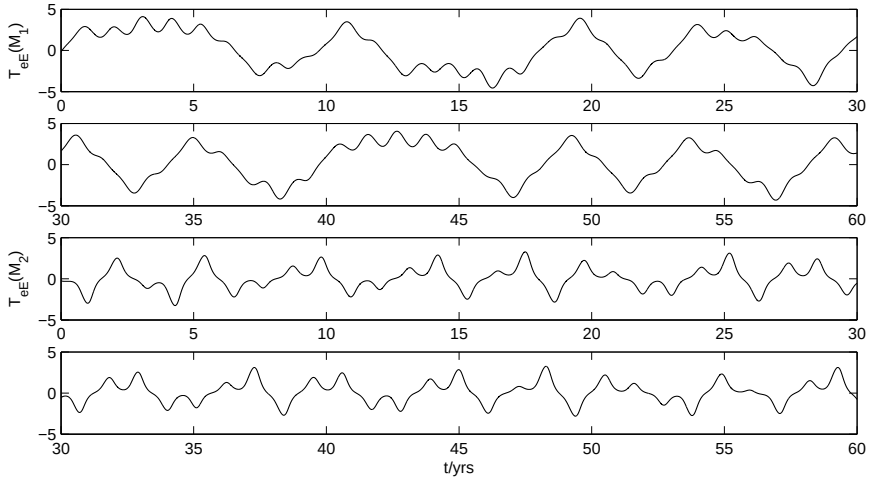

Figure 5.1: Sample timeseries of eastern equatorial SST T_{eE} from M_1 (top) and M_2 (bottom).

- Amplitude of this oscillation is larger than observed in reality,
- Variance as a function of annual phase shows phase locking is present, but not dominant,

and M_2 satisfies

- Fourier spectrum of SST time series indicates an oscillation period of exactly 4 years,
- Amplitude of this oscillation is within a physically justifiable range,
- Variance as a function of annual phase shows phase locking dominates behaviour.

While both models are sensitive to initial perturbations, M_1 being weakly coupled to the annual cycle results in ensembles with more spread, while M_2 suffers from strong seasonal dissipation and orbits converge rapidly through some phases of the annual cycle. An ensemble of perturbed initial states at certain times of year will return to a common state for M_2, but diverge regardless for M_1, making the latter more suitable for initialisation experiments. Although

M_2 and its reduced versions will be used later to test stability as the timestep is increased, M_1 is selected as the main model for the tests of predictability.

5.1.2 Simulation Data

Since a model has been designated to generate artificial observational data, time series generated by M_1 can be seen as a history of the true state of the system; a set of data free from the uncertainties which arise through atmospheric turbulence, exterior forcings or instrumental inaccuracy. Run for a sufficient length beyond spin up time (at least 30 years), to ensure a balanced state has been reached, the final state is used as an initial condition. M_1 is then integrated a further 10^5 timesteps (with the step size around half a day), and approximately 140 years worth of data is recorded. The phase space has 94 thermocline coordinates, 2 box averaged SST coordinates and it is also convenient to include one coordinate ϕ representing the annual cycle, so the data array is 10^5 by 97. Coupling $\kappa(t) = \kappa_0 + \kappa_a \cos(\phi)$ takes a maximum value at $\phi = 0$ (see 3.4, equation (3.112)), and the region $[0, 2\pi]$ is divided into 12 segments with the first month starting at $\phi = 0$, second at $\phi = \pi/6$ and so on. This data, used in the initialisation experiments and finding empirical normal modes, describes an ENSO with a period roughly between 3 and 7 years, a stronger than average event every 15-20 years and a long event lasting for 3 years or more around every 30-40 years. Since the experiments have the potential to generate large amounts of timeseries data, it is useful to define an index which is representative of the entire system at any point in time. In this study, the index will be the mean temperature over the eastern equator, that is

$$T_{eE}(t) = \frac{1}{2}\left[\mathbf{\Theta}_{n+1}(t) + \mathbf{\Theta}_{n+2}(t)\right], \tag{5.1}$$

where $\Theta_1 = T_{e1}$ and $\Theta_2 = T_{e2}$, for a box model of $n = 94$ thermocline variables. Predictability of M_1 will be tested using perturbed initial conditions from the perfect observation as a function of ϕ, and the key to improving this accuracy

is in the reduction of M_1 to lower dimensions.

5.2 Reduction

In order to improve the forecast skill of M_1, a reduction to a lower dimensional model is performed. This lower dimensional model does not integrate directly the model coordinates Θ_i, but instead the normal modes χ_i which resolve large spatial scales for small i and small scale for large i. Dimensions corresponding to χ_i where i is large are not integrated, and this is found to slow error growth in M_1 (see initialisation experiments later) and allows for a larger timestep to be chosen without loss of stability for M_2. Two methods were used to find these normal modes, the first using only the equations of the n-box model and the second using empirical data from the perfect observation. Spatial and temporal characteristics of the reduced models of various dimensionalities are now compared with those of M_1 and M_2, including a time step sensitivity test for the latter and its reduced counterparts.

Variance

Variance of the T_{eE} index is measured as a function of month, or phase ϕ divided into twelve segments $j\pi/6$ integer j, for the n-box model operating in the ENSO-like regimes at $(\kappa_0, R_E, R_W) = (3, 0.26, 0.39)$ with $\kappa_a = \kappa_0$ and $(13/4, 0.47, 0.65)$ with $\kappa_a = \kappa_0/4$. Reduced model variances are shown in figure 5.2, in red for the AIM integration and blue for the SVD with M_1 on the left and M_2 on the right. The black curve shows the seasonal variation in amplitude for both models, confirming each is phase locked to the annual cycle with a maximum at month 4, or $\phi = 2\pi/3$, and a minimum at month 10 ($\phi = 5\pi/3$). In between these months is known as the decaying phase of ENSO, while the complementary region is the growing phase. While the variance of M_1 varies sinusoidally as a function of ϕ with a finite minimum, M_2 has a peak at $\phi = 2\pi/3$ which diminishes rapidly in the decaying phase. The long phase where the variance is

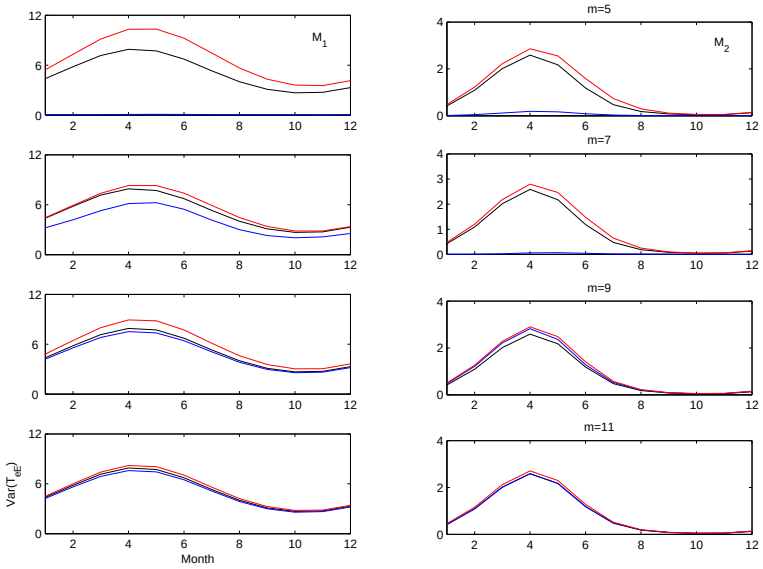

Figure 5.2: Variance of reduced models compared with full model starting with the lowest $m = 5$ (top) to highest $m = 11$ (bottom) dimensionality. AIM reduction is in red, while SVD is in blue, with black curves M_1 on the left and M_2 on the right.

near zero indicates M_2 is too strongly locked to the annual cycle.

Now looking at the variance of the reduced models, it is clear that the SVD approximation does not resemble either M_1 or M_2 for low dimension, but after $m = 7$ the amplitude is reproduced fairly accurately. Integrations performed on the AIM begin inaccurate for the lowest dimension $m = 5$, but converge gradually to the correct values as m is increased. At around $m = 11$ both reductions have roughly the same seasonal variance as the full models. Mean is also calculated as a function of ϕ, but is not shown as it is found to be very close to zero throughout the year; this is to be expected due to the symmetry arguments.

Spectra

Long integrations of the full and reduced models provide 700 years worth of T_{eE} data which are Fourier decomposed. The resulting frequency spectra show

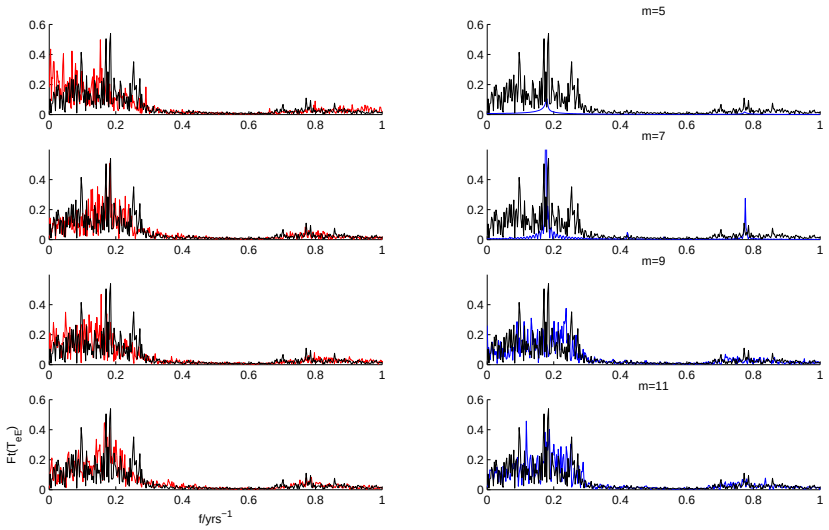

Figure 5.3: Spectra of reduced models compared with full model M_1 starting with the lowest $m = 5$ (top) to highest $m = 11$ (bottom) dimensionality. AIM reduction is in red on the left, while SVD is in blue on the right, with the black curve corresponding to the frequency spectrum of the full model.

how the reduced models compare with the strongly phase locked M_2 and the low frequency dominated M_1. Figures 5.3 and 5.4 reveal a similar picture as the seasonal variance, as the AIM gradually converges to a good approximation and the SVD disagrees for low dimension but agrees well for $m \geq 9$.

There is an advantage AIM has over SVD which means it can reproduce the dynamics of M_1 and M_2 at lower dimension, and for this reason the AIM initialisation experiments begin at $m = 7$, while SVD starts at $m = 9$. It may be worth noting that M_1 has three distinct low frequency peaks which neither reduction method reproduces exactly for the tested dimensionalities, although it was not checked whether these peaks were merely an artifact of this particular integration of the full model.

Stability

Reduced models have the beneficial ability to use longer timesteps without succumbing to numerical instability. This is due to the subspace in which they operate corresponding to spaces of smooth functions, or state vectors repre-

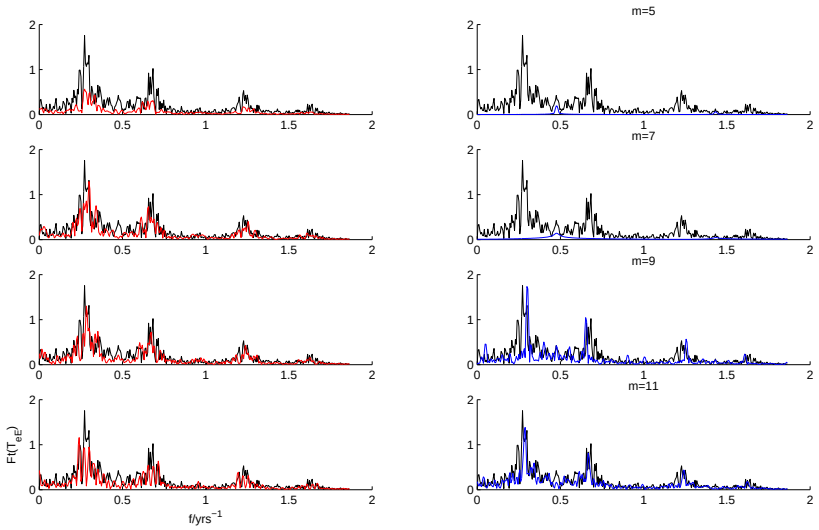

Figure 5.4: Spectra of reduced models compared with model M_2 starting with the lowest $m = 5$ (top) to highest $m = 11$ (bottom) dimensionality. AIM reduction is in red on the left, while SVD is in blue on the right, with the black curve corresponding to the frequency spectrum of the full model.

senting structures which vary only on large spatial scales. To test the stability at different timesteps, the variance of the indicator coordinate is measured for model M_2 run throughout various points from the perfect observation as the timestep is gradually increased.

The full model becomes physically inconsistent when the timestep is increased beyond 2 days. This is not the case for the reduced models, which remain stable for at least twice this step size at even the highest tested ($m = 15$) dimension. The AIM method is clearly stronger for long timesteps, crossing over a half month at $m = 9$. At this stage it may be speculated that a tenfold increase in timestep is practical for lower dimensional approximations, although these experiments are numerically expensive and a distraction from the main focus of this research, which is the improvement of forecast skill.

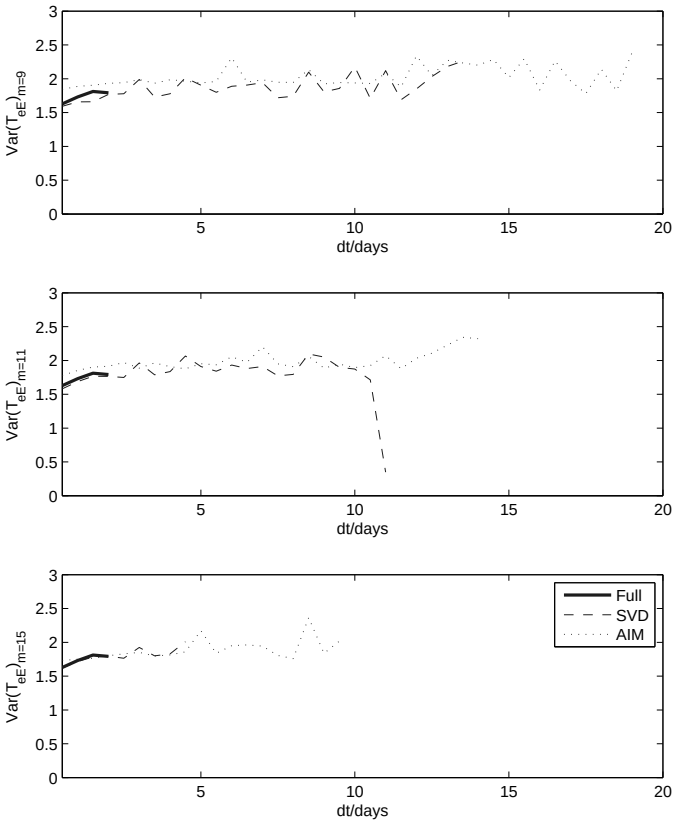

Figure 5.5: Variance (annual mean) of T_{eE}, of the full model and reduced models as timestep is varied in steps of half days up to 20 days.

5.3 Initialisation Experiments

5.3.1 The Forecast Array

The main product of the initialisation experiments is a group of three arrays containing monthly averages of all the ensemble forecasts using initial conditions from the perfect observation. For each of the models, the full model, the inertial manifold approximation and the singular value decomposition, there is a four

dimensional array

$$F^r_{i,j,k,l} = \frac{1}{n_m} \sum_{s=1}^{n_m} T^k_{eE}(12n_m i\Delta t + n_m(j+l)\Delta t + s\Delta t) \tag{5.2}$$

where the subscript i refers to the year number, j the month when the forecast was initiated, k distinguishes one randomly perturbed forecast from another, and l the lead time. The superscript r determines the reduced space in which the model is operating, S for the singular value truncation and I for the inertial form truncation. For example, $F^S_{10,3,2,6}$ will correspond to year 10, the 6th month of an integration starting in month 3, the second in an ensemble of forecasts in month 9, initiated 6 months earlier. While cumbersome, this notation will be useful later on for calculating statistical properties of ensemble forecasts.

5.3.2 Artificial Observation Array

Deviation from observation is what determines the predictability of the models, so along with the forecast data there must also be a recording of simulated empirical data from the full model. This is effectively the artificial observation divided up into monthly averages, that is a two dimensional array

$$P_{m,n} = \frac{1}{n_m} \sum_{s=1}^{n_m} T_{eE}(12n_m m + n_m n + s) \tag{5.3}$$

where again n is the year number, m is the month and n_m the number of timesteps Δt amounting to one month. Error norms are calculated using the forecast array and observation array. Before calculating the statistical properties, a correspondence must be made between the forecast array and the observation array, since each element of $F_{i,j,k,l}$ represents a deviation from $P_{m,n}$. To relate a forecast at lead month l initiated at month j and year i to an element

of $P_{m,n}$, an algebraic relation between (m,n) and (i,j,l) can be derived as

$$m = i + \sigma(j,l) \tag{5.4}$$

$$n = j + l - [1 + 12\sigma(j,l)], \tag{5.5}$$

where

$$\sigma(j,l) = \begin{cases} 1 & \text{if } j + l - 1 > 12; \\ 0 & \text{otherwise.} \end{cases}, \tag{5.6}$$

and indices (m,n) remain unchanged for different values of ensemble index k.

5.4 Initial Perturbations

As was mentioned in the previous chapter, it is important to choose initial perturbations carefully so that the right regions of the tangent space of an initial state are explored. For this model, the tangent vectors will be composed of high and low resolution components, in order to test the sensitivity of the full and reduced models to changes in the spatial scale of random initial errors. It is worth making these perturbations for the n-box model neutral with regards to the initialisation schemes chosen, in that neither eigenvectors of the covariance matrix nor the Jacobian are used. Instead the choice of modes hearkens back to the foundations of the n-box model and its predecessor the 10-box.

5.4.1 Fine Perturbations

Small scale perturbations ϵ_f of initial states from M_1 physically represent random fluctuations of the thermocline profile due to weather noise, and are of the same resolution as the model itself. These are added to the h_n and h_e coordinates of $\mathbf{\Theta}$ only due to the coarse nature of the atmospheric parametrisation used in the n-box model. That is,

$$\epsilon_f = w_f \sum_k X\mathbf{e}_k \tag{5.7}$$

for the n-box thermocline coordinates, where X is a random variable sampled from the uniform distribution centered around zero

$$f(X) = \begin{cases} 1 & |X| < 1/2; \\ 0 & \text{otherwise.} \end{cases}, \tag{5.8}$$

so X can take any value between $X = -1/2$ and $X = +1/2$. The vectors $\mathbf{e}(k)$ are finite difference basis functions for the n-box model, defined by

$$\mathbf{e}_k = \begin{cases} 1 & k = i; \\ 0 & \text{otherwise.} \end{cases} \tag{5.9}$$

The weight parameter w_f controls the amount of small scale noise in the random perturbation. Temperature coordinates $\mathbf{\Theta}_{n+1}$ and $\mathbf{\Theta}_{n+2}$ are unaffected by fine perturbations.

5.4.2 Coarse Perturbations

Climatological fluctuations are parametrised by ϵ_c, which affects thermodynamic variables and clusters of thermocline depths on a large scale. The thermocline structure of this low resolution noise resembles a randomised 10-box model, and the SST coordinates are also altered. Coarse perturbations can be expressed as

$$\epsilon_c = w_c \sum_k X \mathbf{e}_k, \tag{5.10}$$

where $\mathbf{e}_k$ are finite difference basis functions for the 10-box model, defined by

$$\mathbf{e}_k = \begin{cases} 1 & 1 + (k-1)B < i < kB; \\ 0 & \text{otherwise.} \end{cases}, \tag{5.11}$$

in the equatorial strip where $k \in [1, 6]$,

$$\mathbf{e}_k = \begin{cases} 1 & (k-1)B < i < kB - 1; \\ 0 & \text{otherwise.} \end{cases}, \tag{5.12}$$

in the northern strip where $k \in [7, 12]$. Again the points $i = 6B - 1$ and $i = 12B - 1$ are missing due to the boundary conditions. SST variables Θ_{n+1} and Θ_{n+2} are also perturbed with random variables from the same distribution. The degree to which this manner of perturbation will affect the initial condition of a forecast is controlled by the number w_c, and temperature coordinates are affected in the same manner as would a B-sized box of thermocline coordinates.

5.5 Projection

5.5.1 Approximate Inertial Manifold

To perform a calculation on the approximate inertial manifold, first the projection matrix must be found. Diagonalising the Jacobian at the origin provides a sequence of eigenvalues and a matrix of associated eigenvectors. The first three eigenvectors are shown in figure 5.6, corresponding to the first three eigenvalues which are all real. Examining $\mathbf{e}_1$, the only growing mode, reveals a structure similar to the observed ENSO. A positive SST anomaly, shown with the dotted curve, is accompanied by a deepening of the equatorial thermocline to the east and shallowing of the northern strip in the central Pacific. This is contrasted with $\mathbf{e}_2$, which shows no thermocline activity but a single positive SST box anomaly, a slowly decaying mode. The third eigenvector has most of the activity concentrated in the northern strip, where the thermocline is deepened in the east and shallowed in the west. In the equatorial strip, the thermocline is shallowed overall with one positive and one negative SST box anomaly.

It is the inverse of the matrix of eigenvectors which projects a vector to the normal modes, of which the first few m primary modes p are dominant. The q

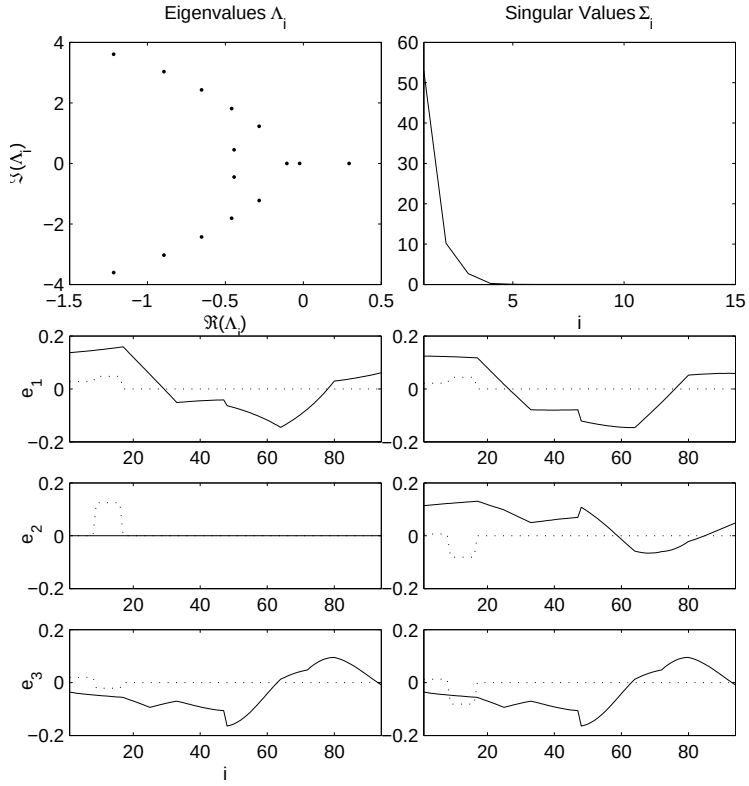

Figure 5.6: First 15 eigenvalues (decreasing from most positive real part) and singular values (largest to smallest magnitude) of M_1, along with the first three eigenvectors and singular vectors, covering h_e $(\Theta_1 \rightarrow \Theta_{48})$, h_n $(\Theta_{49} \rightarrow \Theta_{94})$. Box averaged SST anomalies are shown with dotted curves where they occur relative to thermocline coordinates.

modes are not integrated but affect the nonlinear part of the dynamic equation. A problem arises for the n-box and n^*-box models when n is large enough and the determinant of the matrix of eigenvectors shrinks to near zero. This is due to the tendency of some eigenvectors to align and their dot product tended to unity, while the eigenvalues remain distinct. Where standard inverse calculation methods fail where the matrix is nearly singular, the Moore-Penrose generalised inverse, mentioned in the previous chapter, is used instead.

Further problems arise in the calculation of the projection matrix for the n^*-box model. The eigenfunction corresponding to Λ_2 (the second diagonal element

of Λ in (4.82)), which looks like a unit eigenvector of the n-box model in the $\mathbf{\Theta}_{n+2}$ direction with a flat thermocline, is the first indication of a problem developing as it would appear that there is an uncoupled variable which is slowly varying. As more SST coordinates are added, more modes crop up with the same eigenvalue, meaning the matrix of eigenvectors is singular and thus noninvertable, so the projection onto the approximate inertial manifold cannot be made. This makes sense; the temperature equations are identical and thus have identical eigenvalues. The n-box model avoids this problem as the evolution equation for $\mathbf{\Theta}_{n+2}$ is distinct from that of $\mathbf{\Theta}_{n+1}$ since the latter is not forced by the atmosphere. Some possible ways around this include coupling each SST equation with a unique weight to the atmosphere, or adding random noise to the linear matrix corresponding to the SST variables.

5.5.2 Singular Value Decomposition

Empirical data from the perfect run provides a means to calculate the directions of maximum variance in the phase space. Consider an array which contains each of the components of state vector $\Theta_i(t)$ at times $t = j\delta t$, where δt is the timestep, written Θ_i^j. The covariance matrix is then

$$R = \frac{1}{N} \sum \Theta_i^j \Theta_k^j, \tag{5.13}$$

where a repeated index implies summation over this index and N is the total number of timesteps. The eigenvalues of R, when arranged in decreasing order, drop off to zero after around the values between 5 and 10, as is shown in figure 5.6. This places an upper bound on the dimensionality of the attractor. Since the SVD method requires only empirical data to calculate the projections, and no information about the model equations are required, there is no problem in generalising to more complex models making this a more versatile approach to model reduction. The projection matrix in this case is the transpose of the first m eigenvectors of R. Eigenvectors of R bear some similarity to the

eigenvectors of the Jacobian about $\mathbf{\Theta} = 0$, with the exception of $\mathbf{e}_2$. There is one ENSO-like mode, and a pair of northern strip modes with opposite signs for the thermocline anomalies, but the same SST structure. The first and third eigenvectors are nearly identical to $\mathbf{e}_1$ and $\mathbf{e}_3$, respectively.

5.6 Skill Measures

Monthly averages of the observational sets and perturbed model forecasts at fixed ϕ values provides two sets of values which can be treated as random variables. From these two sets can be calculated commonly used statistical properties which measure how different they are from each other. The data sets X and Y are calculated from the forecast and observational arrays respectively, and forecast skill is calculated as the deviation of X from Y.

5.6.1 Root mean square

This is a measure of the average Euclidean distance between two sets of data. First, the mean is removed to give anomalies $(X_i^{'}, Y_i^{'}) = (X_i - \overline{X}, Y_i - \overline{Y})$. This step is occasionally neglected in the case of very small mean values. Given two sets of N random variables $X_i^{'}$ and $Y_i^{'}$, the root mean square error is

$$\nu(X^{'}, Y^{'}) = \sqrt{\frac{\sum_{i=1}^{N}(X_i^{'} - Y_i^{'})^2}{N}}, \tag{5.14}$$

the average distance between the members of the sets $X^{'}$ and $Y^{'}$.

5.6.2 Correlation

The second test of similarity between the two sets of variables is the correlation, measuring the strength of a linear relationship between variables X_i and Y_i. Again, the mean is removed $(X_i^{'}, Y_i^{'}) = (X_i - \overline{X}, Y_i - \overline{Y})$, which is not neglected

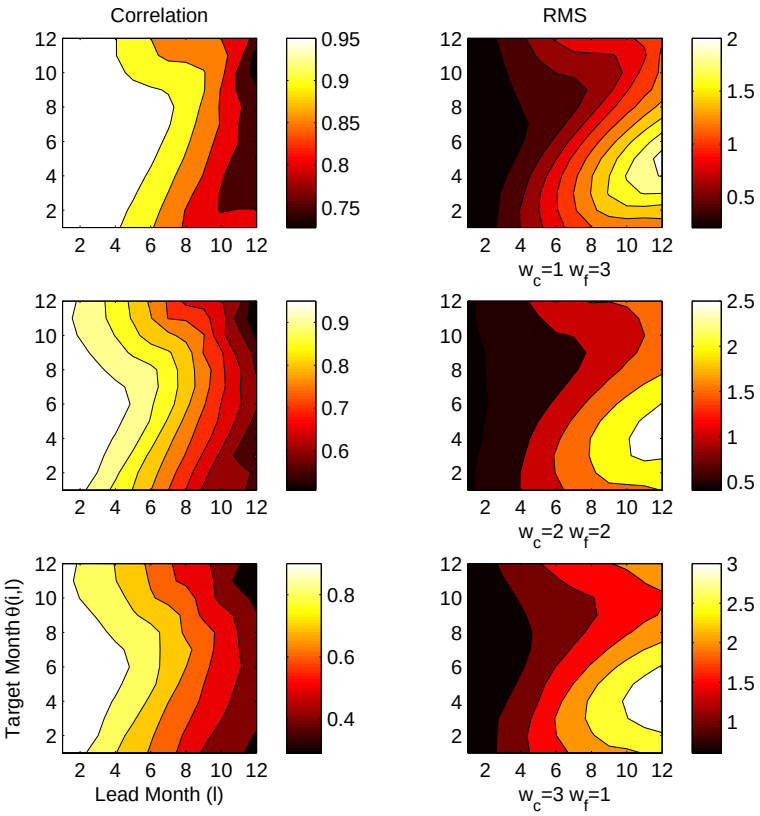

Figure 5.7: Correlation (left) and RMS Error (right) as a function of lead month (l) and target month (a function of i and l). Noise scale varies from fine (top) to coarse (bottom).

even for very small mean values. The correlation is then calculated as

$$\varrho(X^{'}, Y^{'}) = \frac{\sum_{i=1}^{N} X_i^{'} Y_i^{'}}{\left(\sum_{i=1}^{N} X_i^{'2}\right)\left(\sum_{i=1}^{N} Y_i^{'2}\right)}. \tag{5.15}$$

This will take the values $[-1, 1]$ for variables which lie exactly on a straight line through $(X, Y) = 0$ with a negative or positive gradient, or zero for variables which fill the space in a manner depending on the probability distribution they satisfy.

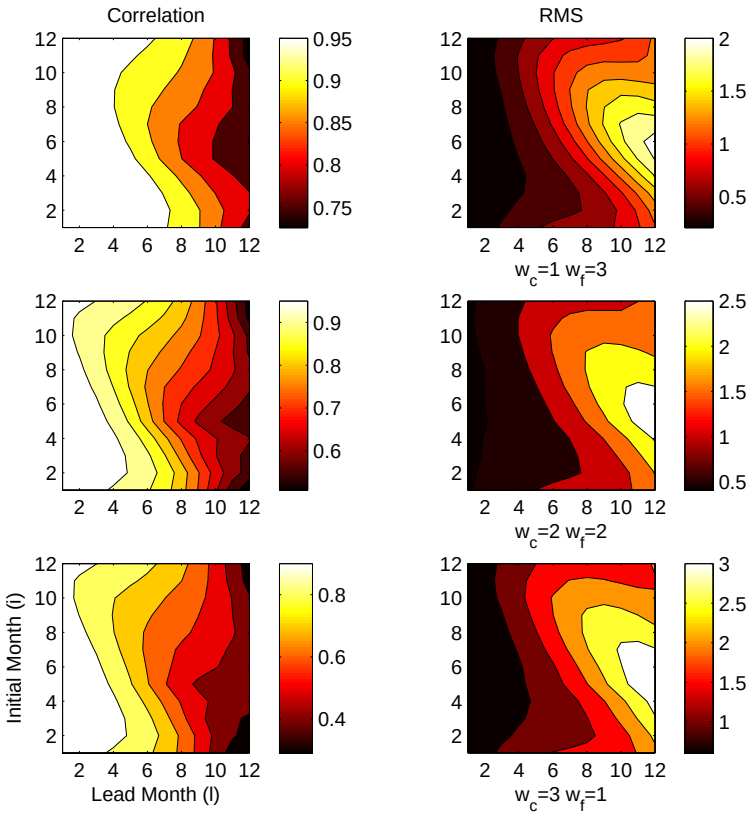

Figure 5.8: Correlation (left) and RMS Error (right) as a function of initial month (i) and lead month (l). Noise scale varies from fine (top) to coarse (bottom).

5.7 Results

5.7.1 Full Model

Predictability of the full model is measured as a function of annual phase. The code developed to calculate this analyses the perfect observation one timestep at a time. Every time annual phase ϕ crosses into another dodecant, a set of 20 random perturbations are added to the state vector which is then time integrated forward one year. This goes on for 50 years until a total of 1000 forecasts have been made for each month, after which the monthly averages are

taken and stored in the forecast array. The sets $X^{'}$ and $Y^{'}$ used to calculate skill measures then each contain 1000 elements, and the values $\nu(i,l)$ and $\varrho(i,l)$ are calculated for three different types of initial perturbation, varying from fine dominated $(w_c, w_f) = (1,3)$, then intermediate $(w_c, w_f) = (2,2)$ to coarse dominated $(w_c, w_f) = (3,1)$.

Figure 5.7 shows how well each month is predicted as a function of lead time, confirming there is an annual dependence on forecast skill. Different types of initial perturbation also have an effect on the outcome of the initialisation experiments. When initial perturbations are on the small scale, the most accurate months are between 8 and 10 as relatively high correlation lasts around 9 months and forecasts remain close to the simulated observation. As the spatial scale increases, the peak shifts back a few months and the best correlation is between 6 and 8 for coarse perturbations. As far as RMS deviations are concerned, the worst months are between 4 and 6, with maximum drift spreading back as far as month 2 and overall magnitude increasing by around 50% for large scale perturbations.

Another arrangement of the same data can be seen in figure 5.8, which show how forecasts initiated at different times of the year fare as lead time is increased. While integrations started after the beginning of the year are the most accurate for fine perturbations, with correlation still high (around 3/4 of the original value) after 12 months, increasing the scale to coarse drastically reduces this timescale to around 8 months. Ensembles passing into and out of an ENSO event are analysed using a collection of 9 ENSO events from the M_1 simulation, with a reduction dimension $m = 9$ and coarse dominated noise. Forecasts (5 in total for each event) are taken around the point where the SST anomaly crosses zero from below for the growth phase, and around the nearest maximum for the decaying phase. Figure 5.13 shows how correlation in the decaying phase, starting low, drops rapidly but starts high and gradually decreases in the growing phase.

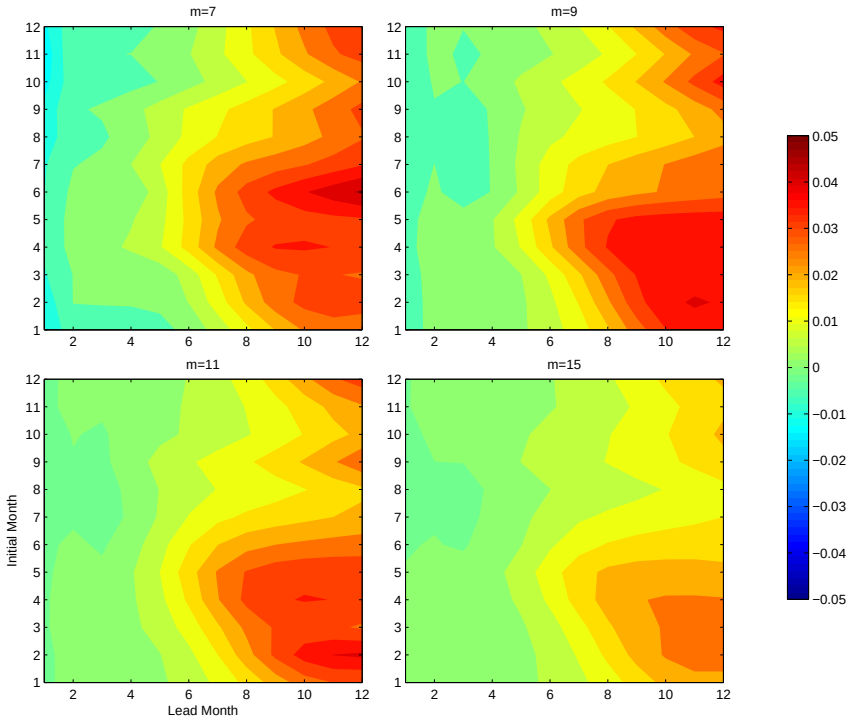

Figure 5.9: Correlation difference $\delta\varrho = \varrho_r(i,l) - \varrho(i,l)$ between M_1 and AIM dimension $m = 7$, with low resolution noise $(w_c, w_f) = (3, 1)$.

5.7.2 Reduced Models

As with the full model, ensemble forecasts are made on the linear and nonlinear subspaces corresponding to the singular value decomposition and approximate inertial manifold respectively, while intensities of coarse and fine noise and reduced model dimension are varied. Correlation $\nu_R(i,l)$ and root mean square deviation $\varrho_R(i,l)$ are measured in the same way as before, and the figures 5.9 and 5.10 look at the differences $\delta\nu = \nu_r(i,l) - \nu(i,l)$ and $\delta\varrho = \varrho_r(i,l) - \varrho(i,l)$ between reduced model and full model statistics. As a general rule, it was found that the magnitude of this difference follows the magnitude of error generated by the full model when predicting itself, and decreases as m is increased.

A comparison between the empirical reduction scheme and the full model when mixed scale initial perturbations can be seen in 5.12, showing a clear

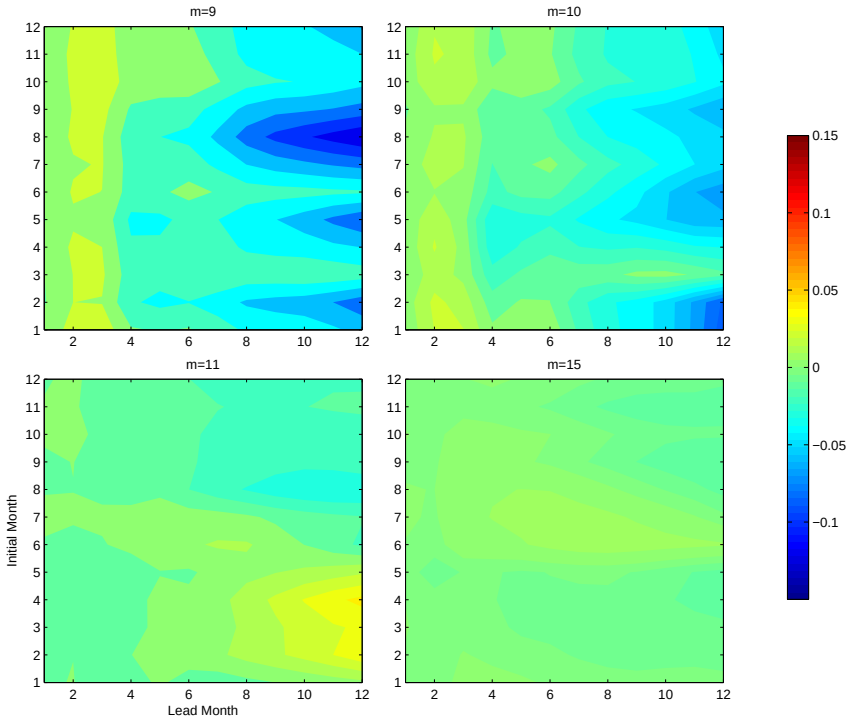

Figure 5.10: RMS difference $\delta\nu = \nu_r(i,l) - \nu(i,l)$ between M_1 and the SVD reduction dimension $m = 9$, with mixed resolution noise $(w_c, w_f) = (2, 2)$.

reduction in RMS error growth has been made. In contrast, the slow manifold approach has a clear improvement in correlation for lead times approaching one year, and this is visible in figure 5.11. Again, measures denoted by the dashed lines in figures 5.12 and 5.11 have been calculated from data produced by modified versions of M_1, where the integration has been performed in a subspace of the full phase space. Skill dependence as a function of ENSO phase is calculated or reduced dimension $m = 9$ and coarse scale noise, and figure 5.13 shows an improvement for both reduced models in the growth phase. Only the AIM method improves predictability in the decay phase, while the SVD method proves to have less skill than the full model towards the end of the forecast. Described here in detail are the results of skill differences $\delta\nu$ and $\delta\varrho$ for coarse dominated noise and fine dominated noise. Results for the intermediate case,

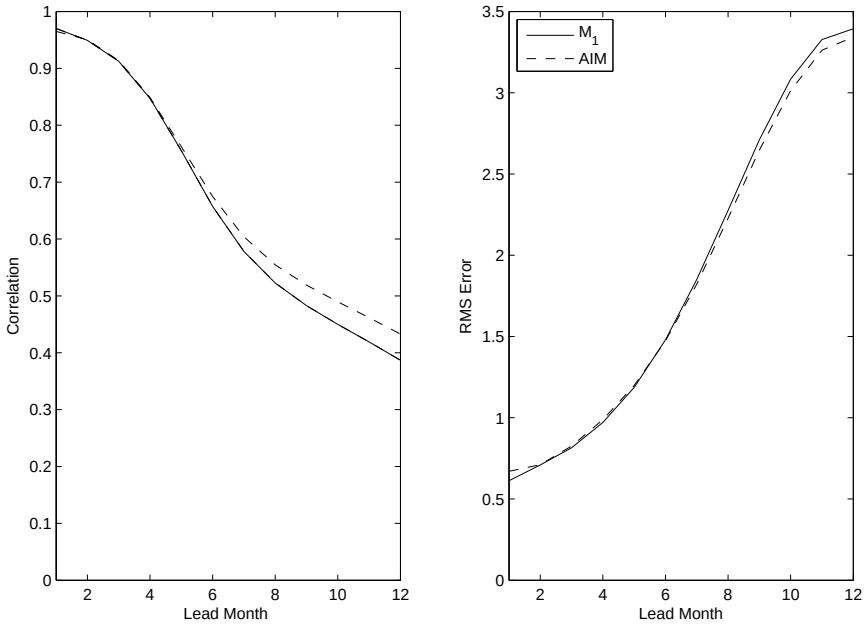

Figure 5.11: Comparison of correlation and RMS error for M_1 (solid line) and the AIM reduction of dimension $m = 7$ (dashed line) for initial month 8. Noise is coarse, parametrised by $(w_c, w_f) = (3, 1)$.

which can be seen in figures 5.14 and 5.15, lie somewhere in between the two cases.

Fine Noise

Random perturbations on the small spatial scales are found to be the least effective in filtering out the weaker initialisation schemes in favour of the stronger ones, and this can be seen in 5.15. It is found that the AIM reduction has virtually no effect on RMS deviation compared with M_1, while the SVD reduction does keep trajectories close to the attractor for low dimensionality, so is more robust with regard to small scale perturbations. An increase in SVD dimensionality to $m = 11$ results in a loss of skill (see figure 5.10), but ultimately there is little difference for large dimensions ($m = 15$). This could provide an indication of the spatial scale of noise (around $m = 10$) which damages the forecast and

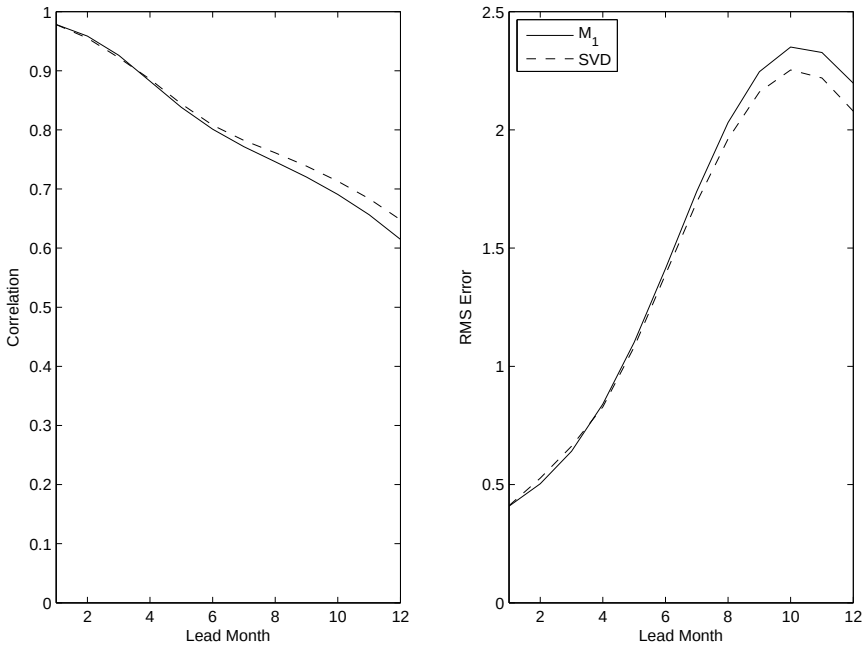

Figure 5.12: Comparison of correlation and RMS error for M_1 (solid line) and the SVD reduction of dimension $m = 9$ (dashed line) for initial month 6. Noise is mixed, parametrised by $(w_c, w_f) = (2, 2)$.

has been filtered for low dimension.

Coarse Noise

Large scale perturbations are more effective than small scale ones, as is demonstrated in the M_1 ensembles as well as the approximate models. Integrations of the inertial form have a clear seasonal dependence, and have more of an impact on correlation than RMS error. Quite the opposite is true for the singular value decomposition, which keeps orbits close to the attractor but is less effective at preserving a linear relationship. A comparison of correlation for both models shown in figure 5.14 would imply that there is a strong seasonal dependence on forecast skill on the AIM, which is less apparent for the SVD. RMS error on the other hand (see figure 5.15), is significantly improved by the SVD method while the AIM has little effect.

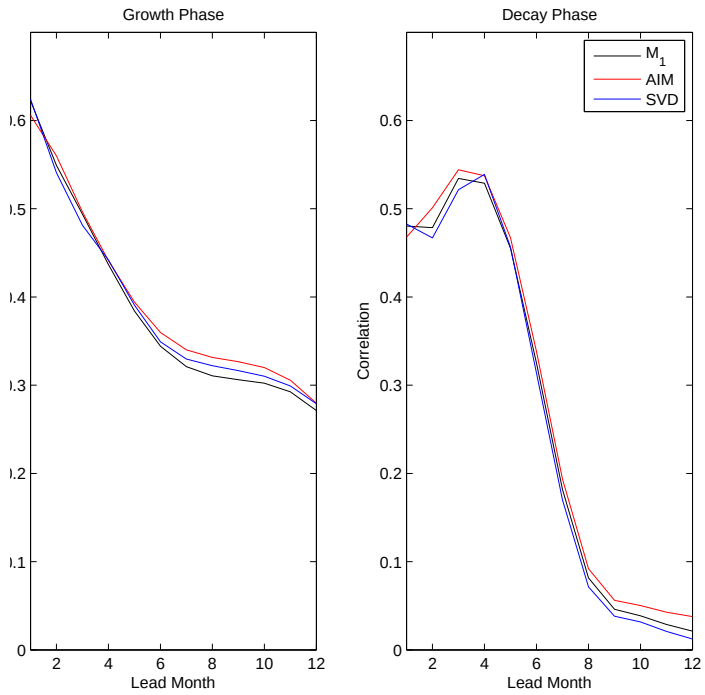

Figure 5.13: Correlation as a function of lead month in the growth (left) and decay (right) phases of ENSO for M_1 (black curve) and the reduced variants (red, blue).

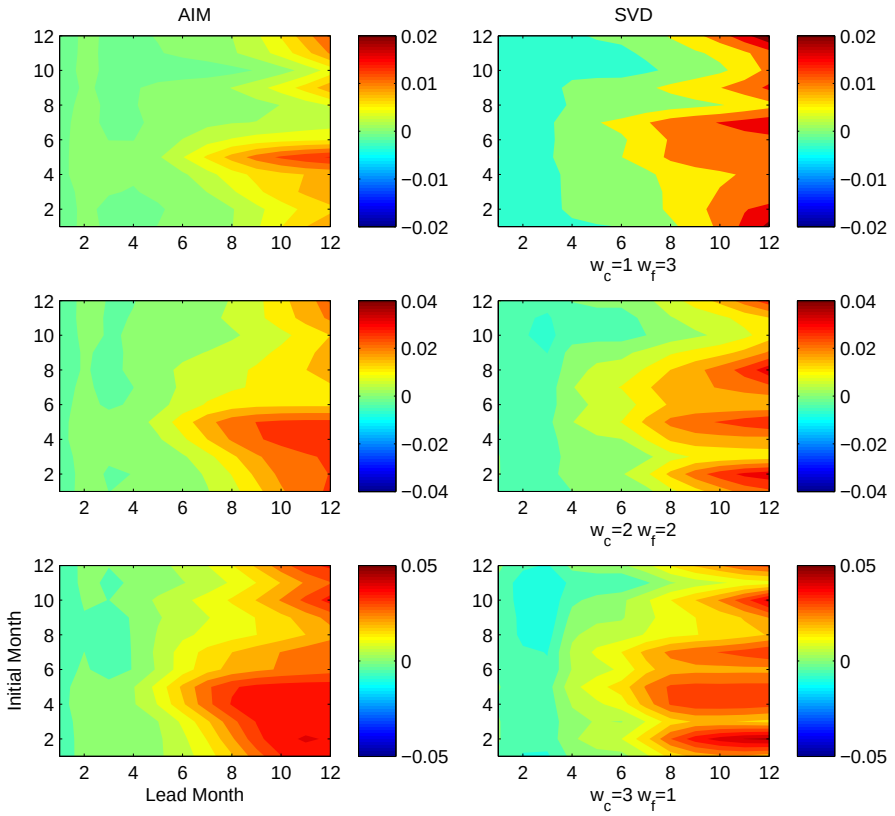

Figure 5.14: Difference in correlation $\delta\varrho$ between M_1 and its approximations AIM ($m = 9$) on the left, SVD ($m = 9$) on the right for varying noise parameters from fine (top) to coarse (bottom).

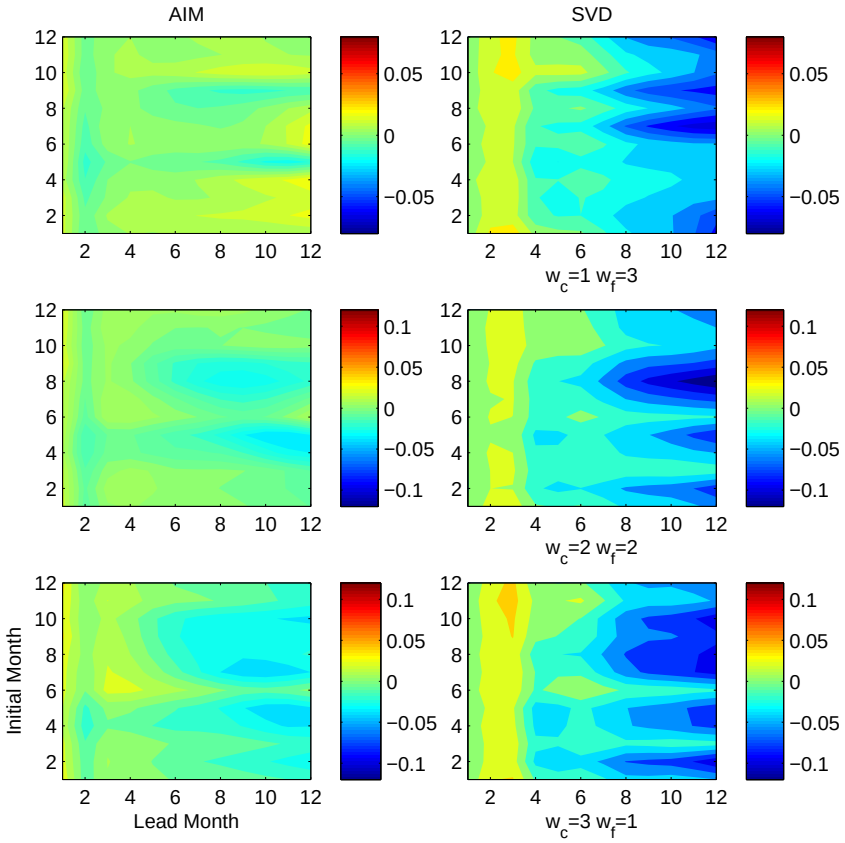

Figure 5.15: Difference in RMS error $\delta\nu$ between M_1 and its approximations AIM ($m = 9$) on the left, SVD ($m = 9$) on the right for varying noise parameters from fine (top) to coarse (bottom).

Chapter 6

Conclusions

6.1 Summary of Research

The research described in this thesis was carried out with the aim of developing new initialisation strategies for use in ENSO modelling. Beginning with low order models, the key idea was to develop a scheme for simple models which was general enough to be applied to a model of arbitrary complexity. This process can be divided into three phases. The first involved deriving a simple 2 ODE system by discretising the Jin[15] 2-strip model, and oscillatory solutions to this model were found with periods and amplitudes close to that of the observed phenomenon. Some regions of the parameter space had multiple solutions, both stable equilibria and limit cycles with a separatrix. An early attempt was made to represent this 2-box system by approximating the attractor of the limit cycle solutions with an ellipse, which was found to be best in the weakly nonlinear limit just after the Hopf bifurcation. However, this representation was not suitable for some of the irregular oscillations encountered in later models.

Phase two was concerned with the evolution of the 2-box into more complex variants based on the 2-strip system, beginning with the 10-box model which incorporated the seasonal cycle and culminating in the n-box PDE system. Mapping out statistics of numerical solutions to these models showed that there was

significant parametric instability, and irregular solutions of infinite period were rare, arising through the interaction of unstable modes and the seasonal cycle since no stochastic forcing was introduced. Chaos was found only in cases with strong ocean-atmosphere coupling and, due to the autonomous dynamical systems approach to modelling, this meant nonlinearity was strong. The transition from a nonautonomous system to an autonomous one with additional nonlinear terms was originally made for numerical efficiency, with an alternative 10-box model with time integrated normal modes. Eigenvectors and eigenvalues were changing with every timestep and needed to be recalculated continuously, so a scheme was devised to make the system autonomous by introducing artificial normal modes representing the seasonal cycle. It also turned out to be useful for normal mode initialisation.

Many solutions were heavily phase locked to the annual cycle with periods which were integer multiples of one year, which could on some occasions be attributed to the large amplitude of coupling variation in the 10-box model. Lyapunov spectra were then calculated using a tangent space method and positive exponents were found. A pair of general PDE models, the n-box and n^*-box models, were then developed using the 10-box as a foundation, each with its own atmospheric parametrisation. While the n^*-box was more complex with a fine scale atmospheric coupling, the n-box was the only model which passed on to the final phase of research, and generated the data to be used as observation. A considerable amount of research time involved finding the appropriate parameters which satisfied the criteria that the n-box model (with $n = 94$) was sufficiently sensitive to initial conditions, had a period and amplitude close to those observed in the real world, and the oscillation was neither too strongly nor too weakly locked to the annual cycle. As a side effect of the parametric instability of the model, a perfect simulation could be an infinitesimal step away in model space to a completely unsuitable one.

Once the appropriate parameters had been found, initialisation schemes were outlined to provide the background for the experiments which comprised the fi-

nal phase, where the n-box model was modified to improve forecast skill. Using two of the schemes outlined, a reduction of models was performed by projecting onto either a nonlinear manifold calculated from the model equations or a linear manifold which was calculated empirically. While problems with matrix inversion arose with the generalisation to the n^*-box model where the projection matrix was found to be singular, the nonlinear reduction made a better approximation at lower dimension. It was also found to be the most resilient to increases in timestep: the linear reduction scheme allowed for a larger timestep than the full model but to a lesser degree. Using timeseries from the n-box model as a proxy for observational data, ensemble forecasts were triggered each month for 50 years with initial conditions provided by this set. These initial states were integrated forward 12 months for the full n-box model and two reduced variants. The full model forecast skill was strongly dependent on initial phase of the annual cycle (phase zero being at the maximum ocean-atmosphere coupling strength), with decorrelation and drift occuring most in the early to mid phases. Results of initialisation experiments for the reduced variants were mixed, but overall the nonlinear method was more effective at improving correlation while the linear method was better for reducing root mean square error. While the linear method was less phase dependent, the nonlinear method had a clear seasonal bias with skill improvement in the first half of the year, roughly at the same phase and lead times where the full model faltered. Forecasts of the growth and decay of events found that correlation dropped gradually in the former case and rapidly in the latter for the full model. In the decay phase, forecasts made by the full model decorrelated rapidly. Linear reduction did worse than the full model in this case, while nonlinear reduction improved predictability.

6.2 Developments

Advancements have been made in the area of ENSO theory starting with the Jin 2-strip model of equatorial thermocline dynamics. With the first discretisation came the 2-box model, and a proposed linear approximation for limit cycles of delayed oscillator type models which was close to numerical simulations near points of bifurcation. A 10-box conceptual model was derived with the following discretisation, which modelled the annual cycle as a subsystem in perpetual simple harmonic motion. This was purely for convenience as it allowed the system, nonautonomous due to the seasonal variation of coupling, to be treated as an autonomous system. Nonetheless the method had not been implemented in other known ENSO-type systems. It has also been shown that the 10-box demonstrates structural instability, and there are chaotic regimes with positive Lyapunov exponents. The final discretisation based on the 10-box was a general PDE system, the n-box model, which was explored empirically for sensitivity to initial conditions. Error growth was reduced using two comparitive schemes, one linear and the other nonlinear. Although the underlying idea for the nonlinear method has not been used in the context of ENSO prediction, it was found to be mathematically equivalent, at least to first order, to other well-known nonlinear initialisation schemes.

6.3 Implications

Beginning with the research into ENSO dynamics and modelling in the early stages, a good approximation was made for the 2-box limit cycle using parameters based on observation. This led to the proposal of a new initialisation scheme which could be used to improve forecast skill for simple models. An original ENSO conceptual model, the 10-box, was derived from a set of coupled PDEs describing the atmospheric forcing of two equatorial wave modes. To incorporate the seasonal cycle, artifical modes were introduced in perpetual simple harmonic motion. While originally included for numerical convenience,

it proved to be useful in normal mode initialisation and could be beneficial for any predictive system with coefficients which vary periodically. It was found, by mapping out statistical properties of the 10-box model whilst varying parameters, that in regions where the dynamics were close to that of the observed ENSO, the system was not structurally stable. This roughness also permeated the parameter space of both the n-box and n^*-box generalisations of the 10-box model. Owing to the persistence of this theme throughout the model hierarchy a general observation could be made on arbitrarily complex models of this type, as to whether the characteristic period is robust to parametric disturbances or prone to drastic change when an infinitesimal change is made to the system. A similar question has been raised by Ghil et al on the role of structural instability with regards to uncertainties in GCM climate projections[88].

Using a choice of parameters from the n-box models, a pair of reductions were made. Integrations were made on a linear manifold calculated empirically and a nonlinear slow manifold derived from the model equations. While the approximate inertial manifold has not been used as an initialisation scheme for ENSO, it is not clear how distinct this method is from the nonlinear normal mode initialisations of Leith or Baer and Tribbia. To first order, the two schemes appear to be mathematically equivalent. Additionally, a problem with the inversion of the matrix of normal modes placed an upper bound on the complexity limit of this scheme. However, the scheme was able to reproduce the attractor of the full model in a lower dimensionality than the empirical reduction, and predictability was smoother as a function of the annual phase, improving correlation most where forecasts were entering the decaying phase of ENSO. Additionally, the nonlinear reduction allowed for a larger timestep. One interpretation is that this is a slow-fast system, where the attractor of this n-box system lives in a nonlinear manifold and a linear scheme is not a sufficiently good approximation to reproduce model dynamics at low dimension. Initialisation as a function of reduced dimensionality m suggests a dimension of less than 10 is required for a substantial reduction in error growth, as beyond

this little change is observed from the full model. This provides an indication of the scale threshold of perturbations, as beyond $m = 10$ the process of filtering initial data has no effect on predictability.

6.4 Future Research

6.4.1 Dynamics Perspective

On reflection, while most of the aims of the original research were met there were just as many questions raised as answered. Some avenues of research which were intended to be explored included the analysis of experimental data for evidence of off-equatorial Rossby wave propagation, analysing the 10-box model with the atmospheric parametrisation of the n-box, exploring the effect of varying different parameters such as wave speed ratio r_s and coupling amplitude k_a, or testing the forecast skill of other n-box models. The key issues were noninvertability of the matrix of eigenvalues (of the Jacobian at the origin) for projection onto the approximate inertial manifold, as well as the problem of finding rare irregular solutions with the right timescales in a large parameter space and the generality of initialisation schemes for low order models. All of these could potentially be overcome by embracing stochastic effects and the theory of nonautonomous (or random) dynamical systems. For the Jacobian problem, eigenvalue degeneracy arose due to the indistinguishability of SST evolution equations. Perturbing those elements of the Jacobian corresponding to SST dynamics randomly by a small amount could disperse these clustered eigenvalues. Alternatively, a different function parametrising the zonal spatial structure of a wind stress anomaly (a tent shape, for example) would ensure each SST equation is unique, since it has been shown the particular shape of zonal wind stress does not affect asymptotic solutions[87]. Much research time was committed to finding irregular solutions with a period and amplitude close to that of the observed ENSO, which could have been saved if irregularity was introduced more cheaply by implementing stochastic forcing. Finally, there was

the issue of transfer to an autonomous dynamical systems which required the expansion of phase space to incorporate artificial modes. While including these modes did not improve predictability in any way, they did permit the separation of time varying and fixed value coefficients by introducing a new nonlinear term which was a prerequisite for the normal mode initialisation scheme used to improve model skill. If instead the pullback attractor (briefly mentioned in the second chapter) were to be approximated, there would be no need to introduce these artificial modes. Additionally, random forcing need not be treated any differently as the resulting systems also fall under the category of nonautonomous dynamics. However, the rigorous theory is relatively new[89] and as a result practical approximations of pullback attractors may be out of reach for now. It is also worth noting that stochastic systems are inherently unpredictable, and should be approached with caution when used as predictive systems.

6.4.2 Initialisation Perspective

It has not yet been explored as to whether initialising the 2-box can assist in improving forecast skill. While the model is intrinsically predictable with some multiple equilibria regimes, the inclusion of both stochastic forcing and the seasonal variation of coupling could result in a sporadic model with a period and amplitude close to the observed mechanism as well as a noisy frequency spectrum. By applying the $R^{-1}SR$ operator on initial data, it may be possible to improve the predictability of this model.

An underlying theme of the research presented in this thesis was the approximation of model attractors as a means to reduce error growth. Based on the fact that a nonlinear scheme was better at approximating behaviour at low dimension than a linear empirical one, an interesting avenue for research could be whether a nonlinear empirical scheme would be advantageous. Nonlinear feature extraction is a well known technique in artificial intelligence and machine learning[90], and has recently seen application in ENSO prediction[91]. An inertial manifold is a finite dimensional manifold embedded in an infinite

dimensional space which attracts orbits exponentially with time. While finite, the dimensionality may well be large, but once the manifold is known it may be possible to find a mapping between a PDE system and a comparatively low order ODE system. While the human brain is constrained to visualise objects in three dimensions or less, there is no dimensional limit to computer vision, meaning that given a long enough timeseries is provided there is no reason why the manifold containing the attractor cannot be learned numerically. Although it has been remarked that ENSO is currently a weakly nonlinear phenomenon excited by noise[23], it has been shown in this thesis that in the case of strong nonlinearity a nonlinear normal mode initialisation scheme may well be a better approach than a linear method for improving correlation in seasonal forecasts. Should there be a regime shift after which the ENSO behaves in a less linear manner, it could be worth investigating nonlinear methods for initialising CGCMs where there may be room for improvement as far as predictability is concerned.

Appendix A

Shallow Water Equations

A.1 Derivation

Here the equations underlying equatorial wave dynamics from which the 2-strip equations are derived, the shallow water equations in an equatorial β-plane, are worked out from scratch. Derivation begins with the Euler equations

$$\frac{\partial \mathbf{u}}{\partial t} + (\mathbf{u} \cdot \nabla)\mathbf{u} = -\frac{1}{\rho}\nabla \overline{p} + \mathbf{F}, \tag{A.1}$$

with the incompressibility condition

$$\nabla \cdot \mathbf{u} = 0, \tag{A.2}$$

where $\mathbf{u}$ is the three component velocity vector, $\overline{p}$ pressure, ρ is (constant) density and $\mathbf{F}$ a body force. The first two components of $\mathbf{u}$, (u, v), are tangent to the surface of the earth, with u pointing in the positive x direction from west to east and v pointing in the positive y direction from south to north, the third, w points in the vertical direction. Here the force is induced by gravity and the rotation of the Earth

$$\mathbf{F} = -2\mathbf{\Omega} \times \mathbf{u} + \nabla(\phi_c - gz), \tag{A.3}$$

with the potential term being a combination of centripetal acceleration from rotation and acceleration due to gravity, with the former to be absorbed into the pressure term. Ω from the Coriolis term is the angular velocity, which is at its maximum at the poles and minimum at the equator. Then, taking θ as the angle of inclination measured from the zenith (the North Pole),

$$\boldsymbol{\Omega} \times \mathbf{u} = \begin{vmatrix} \mathbf{e_1} & \mathbf{e_2} & \mathbf{e_3} \\ 0 & 0 & \Omega \sin\theta \\ u & v & w \end{vmatrix} = \Omega \sin\theta \begin{pmatrix} -v \\ u \\ 0 \end{pmatrix}. \tag{A.4}$$

Consequently, the inviscid Euler equations become

$$\begin{aligned} \frac{\partial u}{\partial t} + \left(u\frac{\partial}{\partial x} + v\frac{\partial}{\partial y} + w\frac{\partial}{\partial z} \right) u - fv &= -\frac{1}{\rho}\frac{\partial p}{\partial x}, \\ \frac{\partial v}{\partial t} + \left(u\frac{\partial}{\partial x} + v\frac{\partial}{\partial y} + w\frac{\partial}{\partial z} \right) v + fu &= -\frac{1}{\rho}\frac{\partial p}{\partial y}, \\ \frac{\partial w}{\partial t} + \left(u\frac{\partial}{\partial x} + v\frac{\partial}{\partial y} + w\frac{\partial}{\partial z} \right) w &= -\frac{1}{\rho}\frac{\partial p}{\partial z} - g, \end{aligned}$$

where $f = 2\Omega \sin\theta$ and $p = \overline{p} - \rho\phi_c$. Now, the average depth of the ocean is around 4 kilometres, while the radius of the earth is around 6000 kilometres, so the ocean is in fact a thin film on the surface of the planet. It can then be treated as an almost two dimensional flow. Taking the characteristic vertical lengthscale to be D and the horizontal L, the quantity

$$\delta = \frac{D}{L} \ll 1 \tag{A.5}$$

permits the scaling out of terms from the rotating Euler equations. After some algebra, the left hand side of the vertical velocity equation turns out to be of relative order δ^2, and drops out of the equations, leaving the hydrostatic equation

$$-\frac{1}{\rho}\frac{\partial p}{\partial z} - g = 0. \tag{A.6}$$

Integrating this with respect to z, assuming ρ is constant, gives

$$-\frac{p}{\rho} - gz = A_0(x, y, t). \tag{A.7}$$

Consider a rectangular basin of ocean whose surface displacement is $\eta(x, y, t)$, with some topography at the ocean floor at $z = 0$ given by $\eta_b(x, y)$, so that the total depth is $H = \eta - \eta_b$. It is reasonable to assume that the pressure at the surface $z = \eta$ is some constant value p_0, and it follows that

$$A_0(x, y, t) = -\frac{p_0}{\rho} - g\eta, \tag{A.8}$$

so the pressure is given by

$$p = p_0 + \rho g(\eta(x, y, t) - z). \tag{A.9}$$

From this the right hand side of both horizontal equations can be determined

$$-\frac{1}{\rho}\frac{\partial p}{\partial x} = -g\frac{\partial \eta}{\partial x}, \tag{A.10}$$

$$-\frac{1}{\rho}\frac{\partial p}{\partial y} = -g\frac{\partial \eta}{\partial y}. \tag{A.11}$$

Since the right hand side is independent of z, so must the left hand side, eliminating two terms from the horizontal equations. Integrating the incompressibility condition with respect to z gives

$$w(x, y, z, t) = \overline{w}(x, y, t) - z\left(\frac{\partial u}{\partial z} + \frac{\partial v}{\partial y}\right), \tag{A.12}$$

whereby the background velocity $\overline{w}$ can be found by exploiting the impermeability condition at the ocean floor,

$$w(x, y, \eta_b, t) = u\frac{\partial \eta_b}{\partial x} + v\frac{\partial \eta_b}{\partial y}, \tag{A.13}$$

thus,

$$\overline{w} = u\frac{\partial \eta_b}{\partial x} + v\frac{\partial \eta_b}{\partial y} + \eta_b\left(\frac{\partial u}{\partial z} + \frac{\partial v}{\partial y}\right). \tag{A.14}$$

Similarly, at the surface $z = \eta$,

$$w = \frac{\partial \eta}{\partial t} + u\frac{\partial \eta}{\partial x} + v\frac{\partial \eta}{\partial y}. \tag{A.15}$$

Substitute this into the integrated incompressibility condition at $z = \eta$,

$$\frac{\partial \eta}{\partial t} + \frac{\partial}{\partial x}[u(\eta - \eta_b)] + \frac{\partial}{\partial y}[v(\eta - \eta_b)] = 0, \tag{A.16}$$

and all that remains are the three shallow water equations

$$\begin{aligned}
\frac{\partial u}{\partial t} + \left(u\frac{\partial}{\partial x} + v\frac{\partial}{\partial y}\right)u - fv &= -g\frac{\partial \eta}{\partial x}, \\
\frac{\partial v}{\partial t} + \left(u\frac{\partial}{\partial x} + v\frac{\partial}{\partial y}\right)v + fu &= -g\frac{\partial \eta}{\partial y}, \\
\frac{\partial H}{\partial t} + \frac{\partial}{\partial x}(uH) + \frac{\partial}{\partial y}(vH) &= 0.
\end{aligned}$$

Most of the dynamics relevant to ENSO occur in the vicinity of the equator, where $f = 2\Omega \sin\theta$ is small enough to make the approximation

$$\sin\theta \approx \theta, \tag{A.17}$$

then

$$f \approx \Omega\theta = \beta y, \tag{A.18}$$

where $\beta = 2\Omega/R_0$, R_0 is the radius of the earth. This is known as the equatorial beta plane approximation.

A.1.1 Linear Shallow Water Theory

To study analytic solutions of the shallow water equations, the equations must be first written in their linear form. Let

$$H(x, y, t) = H_0(x, y) + \eta(x, y, t). \tag{A.19}$$

Removing all terms which are quadratic or higher in (u, v, η) results in

$$\frac{\partial u}{\partial t} - fv = -g\frac{\partial \eta}{\partial x}, \tag{A.20}$$

$$\frac{\partial v}{\partial t} + fu = -g\frac{\partial \eta}{\partial y}, \tag{A.21}$$

$$\frac{\partial \eta}{\partial t} + \frac{\partial}{\partial x}(uH_0) + \frac{\partial}{\partial y}(vH_0) = 0. \tag{A.22}$$

Taking partial derivatives $\frac{\partial}{\partial y}$ of (A.20) and $-\frac{\partial}{\partial x}$ of (A.21) gives

$$\frac{\partial \zeta}{\partial t} + f\left(\frac{\partial u}{\partial x} + \frac{\partial v}{\partial y}\right) = 0, \tag{A.23}$$

where ζ is the relative vorticity

$$\zeta = \frac{\partial v}{\partial x} - \frac{\partial u}{\partial x}. \tag{A.24}$$

By dividing through (A.22) by H_0, it can be seen that the second term in (A.23) is in fact $-f\partial_t\eta/H_0$, resulting in the conservation law

$$\frac{\partial}{\partial t}\left(\frac{\zeta}{f} - \frac{\eta}{H}\right) = 0, \tag{A.25}$$

where the conserved quantity

$$PV = \frac{\zeta}{f} - \frac{\eta}{H_0} \tag{A.26}$$

is the potential vorticity. In the special case that $PV = 0$, the linearised shallow water equations reduce to the Klein-Gordon equation

$$\frac{\partial^2 \eta}{\partial t^2} - c^2 \left(\frac{\partial^2}{\partial x^2} + \frac{\partial^2}{\partial y^2} \right) \eta + f^2 \eta = 0, \tag{A.27}$$

where

$$c^2 = gH. \tag{A.28}$$

Acknowledgements

I would like to thank the following people and institutions for making this happen:

Without the financial support of EPSRC and the UK Met Office, the thesis would not have been possible.

My supervisors, primarily Mike Davey, for his patience and constant support, also Ted Johnson for his helpful contributions.

My examiners Rod Halburd and Magdalena Balmaseda for directing the improvement of quality, also James Robinson for his suggestions.

Finally, the electronic music which was the driving force throughout the process.

Bibliography

[1] Richardson, L. F. (1922) Weather prediction by numerical process. Cambridge University Press.

[2] Charney, J.G., Fjørtoft, R., von Neumann, J. (1950) Numerical integration of the barotropic vorticity equation. Tellus. 2: 237254.

[3] Machenhauer B. (1977) On the dynamics of gravity oscillations in a shallow water model, with applications to normal mode initialization. Beitr. Phys. Atmos. 50: 253271.

[4] Baer, F., Tribbia, J. J. (1977) On complete filtering of gravity modes through nonlinear initialization. Mon. Weather Rev. 105: 1536-1539.

[5] Tribbia, J. J., (1979) Nonlinear initialisation on an equatorial beta-plane. Mon. Weather Rev. 107: 704-713.

[6] Leith, C. E. (1979) Nonlinear normal mode initialization and quasi-geostrophic theory. J. Atmos. Sci. 37: 958-968.

[7] Lorenz E. N. (1980) Attractor sets and quasi geostrophic equilibrium. J. Atmos. Sci. 37: 1685-1699.

[8] Shukla J. (1981) Dynamical predictability of monthly means. J. Atmos. Sci. 38: 2547-2572.

[9] McCreary, J. P. (1983) A model of tropical ocean-atmosphere interaction. Mon. Weather Rev. 111: 370-387.

[10] Vallis, G. K. (1986) El Niño: A chaotic dynamical system? Science 232: 243-245.

[11] Zebiak Z. E., Cane M. A. (1987) A model El Niño-southern oscillation. Mon. Weather Rev. 115: 2262-2278.

[12] Cane M. A., Zebiak Z. E. (1986) Experimental forecasts of El Niño. Nature. 321:827-832.

[13] Battisti D. S., Hirst A. C. (1989) Interannual variability in a tropical atmosphere-ocean system: Influence of the basic state, ocean geometry, and non-linearity. J. Atmos. Sci. 46: 1687-1712.

[14] Jin F.-F. (1997) An equatorial recharge paradigm for ENSO, Part I: Conceptual model. J. Atmos. Sci. 54: 811-829.

[15] Jin F.-F. (1997) An equatorial recharge paradigm for ENSO, Part II: A stripped-down coupled model. J. Atmos. Sci. 54: 811-829.

[16] Tziperman E. et al (1994) El Niño chaos: overlapping of resonances between the seasonal cycle and the pacific ocean-atmosphere oscillator. Science 264: 72-74.

[17] Penland C., Sardeshmuhk, P. D. (1995) The optimal growth of tropical sea surface temperature anomalies. J. Climate 8: 19992004.

[18] Moore, A. M., Kleeman, R. (1999) Stochastic forcing of ENSO by the intraseasonal oscillation. J. Climate 12: 11991220.

[19] Thompson, C. J., Battisti, D. S. (1999) A linear stochastic dynamical model of ENSO. Part I: Model Development. J. Climate 13: 2818-2832.

[20] Thompson, C. J., Battisti, D. S. (2000) A linear stochastic dynamical model of ENSO. Part II: Analysis. J. Climate 14: 445-465.

[21] Panja D., Burgers G. (2006) Predictability of El Niño as a nonlinear stochastic limit cycle. arXiv:nlin/0612043.

[22] Timmermann A., Jin F.-F. (2002) A nonlinear mechanism for decadal El Ni no amplitude changes. Geophys. Res. Lett. 29. 1003, DOI: 10.1029/2001GL013369.

[23] Burgers G., Jin F.-F., van Oldenborgh G. J., (2005) The simplest ENSO recharge oscillator. Geophys. Res. Lett. 32. L13706, DOI: 10.1029/2005GL022951.

[24] Ghil M., Zaliapin I., Thompson S. (2008) A delay differential model of ENSO variability: parametric instability and the distribution of extremes. Nonlinear Proc. Geoph. 15: 417-433.

[25] Xue Y., Cane M. A., Zebiak Z. E., Palmer T. N. (1997) Predictability of a coupled model of ENSO using singular vector analysis. Part II: Optimal growth and forecast skill. Mon. Weather Rev. 125: 20572073.

[26] Chen D., Zebiak S. E., Cane M. A., and Busalacchi A. J. (1997) On the initialization and predictability of a coupled ENSO forecast model. Mon. Weather Rev. 125: 773788.

[27] Ji M., Leetmaa A. (1997) Impact of data assimilation on ocean initialization and El Niño prediction. Mon. Weather Rev. 125: 742753.

[28] Wang G., Kleeman R., Smith N. R., and Tseitkin F. (2002) The BMRC coupled general circulation model ENSO forecast system. Mon. Weather Rev. 130: 975991.

[29] Rasmusson E. M., Carpenter T. H. (1982) Variations in tropical sea surface temperature and surface wind fields associated with the southern oscillation/El Niño. Mon. Weather Rev. 110: 354-384.

[30] Trenberth K. E. (1997) The definition of El Niño. B. Am. Meteorol. Soc. 78: 2771-2777.

[31] Walker G. T. (1923) Correlation in seasonal variations of weather VIII. Mem. Indian Meteor. Dep. 24: 75-131.

[32] Glantz, M. H. (2001) Currents of change: Impacts of El Nio and La Nia on climate and society. Cambridge University Press.

[33] Couper-Johnston R. (2000) El Niño: The weather phenomenon that changed the world. Hodder & Stoughton.

[34] WMO (1999) The global climate system in 1998. WMO Bulletin 48: 251-255.

[35] Philander S. G. (1989) El Niño, La Niña, and the southern oscillation. International Geophysics.

[36] McCreary J. P., Anderson D. L. T. (1991) An overview of coupled ocean-atmosphere models of El Niño and the southern oscillation. J. Geophys. Res. 96: 31253150.

[37] Neelin, J. D. et al (1998) ENSO theory. J. Geophys. Res. 103: 14,26114,290.

[38] Manabe S., Smagorinsky J., Strickler R. (1965) Physical climatology of a general circulation model with a hydrologic cycle. Mon. Weather Rev. 93: 769798.

[39] Bryan K., Cox M. D. (1968) A nonlinear model of an ocean driven by wind an differential heating, parts I and II. J. Atmos. Sci. 25: 945-978.

[40] Manabe S., Bryan K. (1969) Climate calculations with a combined ocean-atmosphere model. J. Atmos. Sci. 26: 786-789.

[41] Rowntree, P. R. (1972) The influence of tropical east Pacific ocean temperatures on the atmosphere. Q. J. Roy. Meteor. Soc. 98: 290-321.

[42] Johns T. C., et al (2006) The new Hadley centre climate model (HadGEM1): Evaluation of coupled simulations. J. Climate 19: 1327-1353.

[43] van Oldenborgh, G. J. et al (2005) Did the ECMWF seasonal forecast model outperform statistical ENSO forecast models over the Last 15 years?. J. Climate 18: 3240-3249.

[44] Arribas A. et al (2010) The Glosea4 prediction system for seasonal forecasting. Mon. Weather Rev. 139: 1891-1910.

[45] Kalman, R. E. (1960) A new approach to linear filtering and prediction problems. J. Basic Eng.-T. ASME 82: 35-45.

[46] McWilliams, J. C., Gent, P. R., (1978) A coupled air-sea model for the tropical Pacific. J. Atmos. Sci. 35: 962-989.

[47] Bjerknes J. (1969) Atmospheric teleconnections from the equatorial Pacific. Mon. Weather Rev. 97: 163-172.

[48] Suarez M. J., Schopf P. S. (1988) A delayed action oscillator for ENSO. J. Atmos. Sci. 45: 3283-3287.

[49] Drazin P. G. (1992) Nonlinear systems. Cambridge University Press.

[50] Jordan D. W., Smith P. (1999) Nonlinear ordinary differential equations: An introduction to dynamical systems. 3rd edition. Oxford University Press.

[51] Gilmore R., Lefranc M. (2002) The topology of chaos. Wiley.

[52] Rössler O. E. (1976) Chaotic behavior in simple reaction system. Z. Naturforsch A. 31: 259-264.

[53] Lorenz E. N. (1963) Deterministic nonperiodic flow. J. Atmos. Sci. 20: 130-141.

[54] Wolf A., Swift J. B., Swinney H. L., Vastano J. A. (1985) Determining Lyapunov exponents from a time series. Physica 16D: 285-317.

[55] Palmer T. N., Buizza R., Molteni F., Chen Y.-Q., Corti S. (1994) Singular vectors and predictability of weather and climate. Philos. T. R. Soc. S-A. 348: 459475.

[56] Birman J. S., Williams R. F. (1983) Knotted periodic orbits in dynamical systems I: Lorenz's equations. Topology 22 (1) 47-82.

[57] Daley R., Puri K. (1980) Four-dimensional data assimilation and the slow manifold. Mon. Weather Rev. 108: 8599.

[58] M. A. Balmaseda et al (2009) Ocean initialization for seasonal forecasts. Oceanography Vol. 22 No. 3: 154-159.

[59] Pedlosky J. (1987) Geophysical fluid dynamics. 2nd edition. Springer-Verlag.

[60] Gill A. E. (1982) Atmosphere-ocean dynamics. International Geophysics.

[61] Gill A. E. (1980) Some simple solutions for heat-induced tropical circulation. Q. J. Roy. Meteor. Soc. 106: 447462.

[62] Jin F.-F., Neelin J. D. (1993) Modes of interannual tropical oceanatmosphere interactionA unified view. Part I: Numerical results. J. Atmos. Sci. 50: 34773502.

[63] Chekroun M. D., Simmonnet E., Ghil M. (2010) Stochastic climate dynamics: Random attractors and time-dependent invariant measures. Physica D. Accepted.

[64] Wu Z.-K. (2009) Solution of the ENSO delayed oscillator with homotopy analysis method. J. Hydrodyn. S-B. 21: 131-135.

[65] Benettin G., Galgani L., Giorgilli A., Strelcyn J.-M. (1980) Lyapunov characteristic exponents for smooth dynamical systems and for Hamiltonian systems; A method for computing all of them. Meccanica 15: 10-20.

[66] Shimada I., Nagashima T. (1979) A numerical approach to ergodic problem of dissipative dynamical systems. Prog. Theor. Phys. 61: 1605-1616.

[67] Kim S. T., Jin F.-F., (2010) An ENSO stability analysis. Part II: results from the twentieth and twenty-first century simulations of the CMIP3 models. Clim. Dynam. DOI: 10.1007/s00382-010-0872-5.

[68] Katok A., Hasselblatt B. (1996) Introduction to the modern theory of dynamical systems. Cambridge University Press.

[69] Deremble B., D'Andrea F., Ghil M. (2009) Fixed points, stable manifolds, weather regimes and their predictability. Chaos. DOI: 10.1063/1.3230497.

[70] Toth Z., Kalnay E. (1997) Ensemble Forecasting at NCEP and the breeding method. Mon. Weather Rev. 125: 3297-3319.

[71] Loeve, M. (1963) Probability theory. 4th edition. Springer-Verlag.

[72] Lumley J. L. (1967) The structure of inhomogeneous turbulent flows. Atmospheric turbulence and radio wave propagation: 166-178. Elsevier.

[73] Berkooz G., Holmes P., Lumley J. L. (1993) The proper orthogonal decomposition in the analysis of turbulent flows. Annu. Rev. Fluid. Mech. 25: 539-575.

[74] Chaterjee A. (2000) An introduction to the proper orthogonal decomposition. Curr. Sci. India. 78: 808-817.

[75] Gollub G., Kahan W. (1965) Calculating the singular values and pseudo-inverse of a matrix. SIAM J. Numer. Anal. S-B. 2: 205-224.

[76] Mallet-Paret J., (1976) Negatively invariant sets of compact maps and an extension of a theorem of Cartwright. J. Differ. Equations 16: 331-348.

[77] Foias C., Sell G. R., Temam R. (1988) Inertial manifolds for nonlinear evolutionary equations. J. Differ. Equations 73: 309-353.

[78] Foias C., Nicolaenko B., Sell G. R., Temam R. (1988) Inertial manifolds for the Kuramoto-Sivashinsky equation and an estimate of their lowest dimension. J. Math. Pures Appl. 67: 197-226.

[79] Constantin P. (1989) A construction of inertial manifolds. Contemp. Math. 99: 27-62.

[80] Debussche A., Temam R. (1991) Inertial manifolds and slow manifolds. Appl. Math. Lett. 4: 73-76.

[81] Foias C., Jolly M. S., Kevrekidis I. G., Sell G. R., Titi E. S. (1988) On the computation of inertial manifolds. Phys. Lett. A 131 Nos 7, 8: 433-436.

[82] Robinson J. C. (2001) Infinite-dimensional dynamical systems. Cambridge University Press.

[83] Temam R. (1997) Infinite dimensonal dynamical systems in mechanics and physics. Applied Mathematical Sciences.

[84] Foias C., Titi E. S. (1991) Determining nodes, finite difference schemes and inertial manifolds. Nonlinearity 4: 135-153.

[85] Boyd J. P. (2001) Chebyshev and Fourier spectral methods. Second edition. Dover.

[86] Jin E. K. et al (2008) Current status of ENSO prediction skill in coupled ocean-atmosphere models. Clim. Dynam. 31: 647664.

[87] Schopf P. S., Suarez M., J. (1990) Ocean wave dynamics and the time scale of ENSO. J. Phys. Oceanogr. 20: 629645.

[88] Ghil M., Chekroun M.D., Simonnet E. (2008) Climate dynamics and fluid mechanics: natural variability and related uncertainties. Physica D. 237: 21112126.

[89] Arnold L. (1998) Random dynamical systems. Springer.

[90] C. M. Bishop. (1995) Neural networks for pattern recognition. Clarendon Press.

[91] An S. I., Hsieh W. W., and Jin F. F. (2005) A nonlinear analysis of the ENSO cycle and its interdecadal changes. J. Climate. 18: 32293239.